PHASE TRANSFORMATIONS AND STRUCTURE PROPERTY CORRELATIONS IN Ni-Cr-Mo ALLOYS

By

RUMU HALDER BANERJEE

(PHYS01201504015)

Bhabha Atomic Research Centre, Mumbai

A thesis submitted to the

Board of Studies in Physical Sciences

In partial fulfillment of requirements

for the Degree of

DOCTOR OF PHILOSOPHY

of

HOMI BHABHA NATIONAL INSTITUTE

December, 2020

Homi Bhabha National Institute[1]

Recommendations of the Viva Voce Committee

As members of the Viva Voce Committee, we certify that we have read the dissertation prepared by Smt. Rumu Halder Banerjee entitled "**Phase Transformations and Structure Property correlations in Ni-Cr-Mo alloys**" and recommend that it may be accepted as fulfilling the thesis requirement for the award of Degree of Doctor of Philosophy.

Chairman – Prof. R. Tewari **Date:** 30/08/21

Guide / Convener – Prof. Ashok K. Arya **Date:** 30/08/2021

Examiner – Prof. N. Prabhu **Date:** 01/09/2021

Member 1- Prof. S. M. Yusuf Md. Yusuf **Date:** 30.8.2021

Member 2- Prof. P. Mukherjee. P. Mukherjee **Date:** 20.8.21

Final approval and acceptance of this thesis is contingent upon the candidate's submission of the final copies of the thesis to HBNI.

I/We hereby certify that I/we have read this thesis prepared under my/our direction and recommend that it may be accepted as fulfilling the thesis requirement.

Date: 01/09/2021

Place: Mumbai

Guide

---

[1] This page is to be included only for final submission after successful completion of viva voce.

STATEMENT BY AUTHOR

This dissertation has been submitted in partial fulfillment of requirements for an advanced degree at Homi Bhabha National Institute (HBNI) and is deposited in the Library to be made available to borrowers under the rules of the HBNI.

Brief quotations from this dissertation are allowable without special permission, provided that accurate acknowledgement of the source is made. Requests for permission for extended quotation from or reproduction of this manuscript in whole or in part may be granted by the Competent Authority of HBNI when in his or her judgment the proposed use of the material is in the interests of scholarship. In all other instances, however, permission must be obtained from the author.

Rumu Halder

(Rumu Halder Banerjee)

DECLARATION

I, hereby, declare that the investigation presented in the thesis has been carried out by me. The work is original and has not been submitted earlier as a whole or in part for a degree/diploma at this or any other Institution / University.

Rumu Halder
Rumu Halder Banerjee

List of Publications arising from the thesis

a. <u>Journal:</u>

1. "Quantitative description of the role of Cr on ordering characteristics in a single phase Ni-16 wt.% Mo- 7wt.% Cr alloy", **<u>Rumu H. Banerjee</u>**, A. Arya, H. Donthula, C. Nayak, D. Bhattacharya and S. Banerjee, ***Acta Materialia***, 219 (2021) 117263.
2. "A comparative study of surface layer formation in Ni-based alloys with varying Cr contents exposed to high temperature fluoride environment", **<u>Rumu H. Banerjee</u>**, V. Singh, A. Arya and S. Banerjee, ***Journal of Nuclear Materials***, 516 (2019) 54-62.
3. "Evaluating effective pair and multisite interactions for Ni-Mo system", **<u>Rumu H. Banerjee</u>**, A. Arya and S. Banerjee, ***AIP conference proceedings***, 1942 (2018) 090016.

b. <u>To be communicated</u>

1. Microstructural degradation of Ni-Mo-Cr alloy under tellurium attack, **<u>Rumu H. Banerjee</u>**, Vishal Singh, A. Arya and S. Banerjee.

2. Evolution of ordering in Ni-Mo alloys, **<u>Rumu H. Banerjee</u>**, A. Arya and S. Banerjee.

<u>Publications in conferences/symposiums:</u>

a. <u>International Conferences:</u>

1. "Short term interaction of Ni-based alloys with eutectic LiF-NaF-KF salt", **<u>Rumu H. Banerjee</u>**, Vishal Singh, A. Arya and S. Banerjee, *National Metallurgists Day- Annual Technical meeting (NMD-ATM),* Goa, India **2017**. (**Oral presentation**)

2. "Microstructural and Cluster expansion based studies on Ni-Mo-Cr alloy for high temperature applications", **<u>Rumu H. Banerjee,</u>** Vishal Singh, H. Donthula, A. Arya and S.

Banerjee, *International Conference on Advanced Materials and Manufacturing Processes for Strategic Sectors (ICAMPS)*, Trivandrum, India **2018**. (**Poster Presentation**)

3. "Microstructural degradation of Ni -16 wt. % Mo - 7 wt.% Cr alloy by simulated fission product tellurium", **<u>Rumu H. Banerjee</u>**, Harish Donthula, Vishal Singh, A. Arya and S. Banerjee, *12th Asia-Pacific Microscopy Conference (APMC-2020)*, Hyderabad, India **2020**. (**Poster Presentation**)

b. <u>National Conferences:</u>

1. "Evaluating effective pair and multisite interactions for Ni-Mo system", **<u>Rumu H. Banerjee</u>**, A. Arya and S. Banerjee, *DAE-Solid State Physics Symposium*, Mumbai, India **2017**. (**Poster presentation**)
2. "Cluster expansion based Monte Carlo study of order-disorder phase transitions in Ni-Mo alloys", **<u>Rumu H. Banerjee</u>**, A. Arya and S. Banerjee, *The first DAE computational chemistry symposium (DAE-CCS)*, Mumbai, India **2019. (Poster presentation)**

<u>Other Publications (Not included in the thesis):</u>

1. "Understanding self-ion damage in FCC Ni-Cr-Fe based alloy using X-ray diffraction techniques", **<u>Rumu H. Banerjee</u>**, P. Sengupta, A. Chatterjee, S.C. Mishra, A. Bhukta, P. V. Satyam, I. Samajdar and G. K. Dey, ***Journal of Nuclear Materials***, 501 **(2018)** 82-93.
2. "Photoluminescence study on irradiated yttria stabilized zirconia', **<u>R. Halder</u>**, P. Sengupta, V. Sudarsan, A. Ghosh, A. Ghosh, A. Bhukta, G. Sharma, I. Samajdar and G. K. Dey, ***Journal of Nuclear Materials***, 456 **(2015)** 359-368.

3. “Perovskite-Ni composite: A potential route for management of radioactive metallic waste”, P. S. Mahadik, P. Sengupta, **R. Halder**, G. Abraham and G. K. Dey, ***Journal of Hazardous Materials***, 287 **(2015)** 207-216.
4. “Interaction of Alloy 693 with borosilicate glass at high temperature", **R. Halder**, P. Sengupta, G. Abraham, C. P. Kaushik and G. K. Dey, ***Materials Today: Proceedings***, 3 **(2016)** 3025–3034.

Rumu Halder

Rumu Halder Banerjee

Dedicated to My Family

and

My Mentor Dr. S. Banerjee

ACKNOWLEDGEMENTS

First of all, I wish to express my sincere gratitude to my mentor and former guide Late Dr. Srikumar Banerjee for his valuable guidance, constant supervision and cooperation throughout the execution of the dissertation. His patience, support and encouragement had kept me motivated to complete this study. I am equally grateful to my advisor Dr. Ashok K. Arya for sharing his scientific knowledge on computational techniques and providing constant guidance to understand the subject. I also thank my doctoral committee members Dr. R. Tewari, Dr. S. M. Yusuf, Dr. P. Mukherjee and Dr. G. K. Dey (ex-member) for sharing their precious time for the periodic assessment of the work and providing valuable suggestions in enhancing the quality of the thesis.

I would like to express my sincere thanks to Mr. Vishal Singh, Mr. Harish Donthula and Dr. Naveen who have helped me in sample characterization using electron microscopy. I also thank my collaborators Dr. Chandrani Nayak and Dr. D. Bhattacharya for providing immense help in EXAFS measurements and extensive discussions on the analyses. Help provided by Dr. Amit Verma in alloy heat treatments, Dr. A. K. Debnath in sample coating and Dr. K. K. Swain for elemental analyses is also thankfully acknowledged. I also thank Mr. Ravi Hankare, Mr. Santosh and Smt. Nidhi Pandey for helping in arc melting and sample preparation. I take this opportunity to thank all the staff of supercomputing facility for providing technical support. I would like to acknowledge my sincere gratitude to all my colleagues of Materials Science Division for their constant encouragement and moral support.

The immense task of compiling this PhD thesis would not have been completed without the support and encouragement of my family members. I am forever indebted to my parents for their unconditional love, support and best wishes. I owe a special thanks to my husband for his constant encouragement, unrelenting confidence in me and patiently reviewing the thesis draft multiple times.

Above all, I praise almighty God, for being with me all the time and guiding me through all the difficult times.

CONTENTS

List of Abbreviations

ARE	Aircraft reactor experiment
ATAT	Alloy theoretic automated toolkit
BCC	Body centered cubic
BCO	Body centered orthorhombic
BCT	Body centered tetragonal
BE	Binding energy
BF	Bright field
BSE	Back scattered electron
CCD	Charged couple device
CE	Cluster expansion
Corrdump	Correlation dumper
CV	Cross validation
DCM	Double crystal monochromator
DF	Dark field
DFT	Density functional theory
Dpa	Displacement per atom
ECI	Effective cluster interaction
EDS	Energy dispersive spectroscopy
EMC2	Easy Monte Carlo Code
EXAFS	Extended X-ray absorption fine structure
FCC	Face centered cubic
FESEM	Field emission scanning electron microscope

FIB	Focussed ion beam
F/T	Fast/Thermal
FT-EXAFS	Fourier transformed extended X-ray absorption fine structure
FWHM	Full width at half maximum
Gen	Generation
HAADF	High angle annular dark field
HCP	Hexagonal closed Packed
IGC	Intergranular corrosion
IMSBR	Indian Molten salt breeder reactor
LRO	Long range ordered
MAPS	MIT ab-initio phase stability
MC	Monte Carlo
Mcsqs	Monte Carlo special quasirandom structures
MSBR	Molten Salt breeder reactor
MSR	Molten salt reactors
MSRE	Molten Salt reactor experiment
MWe	Mega Watt electrical
MWth	Mega Watt thermal
NN	Nearest neighbour
ORNL	Oak Ridge National Laboratory
PAW	Projector-augmented wave
PBE	Perdew-Burke-Ernzerhof functional
SA	Solution Annealed
SAED	Selected area electron diffraction
SCC	Stress corrosion cracking

SCW	Static concentration wave
SCWR	Supercritical water reactors
SE	Secondary electron
SIM	Structure inversion method
SQS	Special quasirandom structures
SRO	Short range ordering
TB-LMTO	Tight-binding linear muffin-tin orbital
TCP	Topologically closed phase
TEM	Transmission electron microscope
VASP	Vienna ab-initio simulation package
WQ	Water Quenched
XPS	X-ray photoelectron spectroscopy
XRD	X-ray diffraction
XRF	X-ray fluorescence

List of Symbols

a_o	Lattice parameter of fcc matrix
a_{Ni}	Lattice parameter of Ni
a_{alloy}	Lattice parameter of alloy
a, b, c	Lattice parameters
$\alpha(l), \alpha_{i\text{-}j}$	Warren Cowley parameter for lth coordination shell where the atoms at ith and jth site are separated by distance i-j
A	Helmholtz free energy
c_A	Atomic fraction of atoms of type A in alloy $A_{1-x}B_x$
c_B	Atomic fraction of atoms of type B in alloy $A_{1-x}B_x$
c_i	Atomic fraction of atoms of ith constituent element
$C_{o,Cr}(x,t)$	Cr concentration at distance *x* from the alloy surface at time t=0
$C_{Cr}(x,t)$	Cr concentration at distance *x* from the alloy surface at any time t
$\chi(E)$	EXAFS Function
$\chi(k)$	EXAFS oscillations
d	Distance from the alloy surface
δ	Width of the grain boundary
δ_{AB}	Kronecker delta
D_{eff}	Effective diffusion coefficient
D_{gb}	Grain boundary diffusivity
D_v	Lattice diffusivity

$D\varphi$	Cluster multiplicity
e/a	Valence electron to atom ratio
E	Energy
E_i	Formation energy of the i^{th} structure predicted by CE
E_{CE}	Energy of the structure obtained by fitting with cluster expansion formalism
E_{DFT}	Energy calculated from DFT approach
f_{Mo}, f_{Ni}	Atomic scattering factors for Mo and Ni, respectively
G	Gibbs free energy
γ	Fcc matrix
h	Planck's constant
η	Long range order parameter
hkl	Miller indices for planes corresponding to the fcc matrix
HKL	Miller indices for the plane corresponding to $D1_a$ phase
ΔH	Enthalpy of formation
I_o	Flux of the incident X-ray beam
I_f	Flux of the Fluorescent X-rays
J_{ij}, $J\varphi$, $J\gamma$	Effective cluster interaction parameters
k	Wave vector
K_B	Boltzmann constant
l_α	Cluster diameter (Å)
λ	Wavelength of X-ray beam
m	Separation distance between the cluster vertices
$\mu(E)$	Normalised absorption coefficient
$\mu_o(E)$	Absorbance due to bare atom

n	Number of lattice sites
n_α	Cluster type
v	Frequency of the electromagnetic wave
N	Coordination number in the first coordination shell
ω	Chemical potential
φ, Υ	Clusters
Φ	Grand potential of the semi-canonical ensemble
$P_i(BA)$	Probability of finding A atom in the vicinity of B atom
r	Bond length corresponding to first nearest neighbour distance
R	Goodness of EXAFS fit
ρ	Calculated correlation
ρ_a	Actual correlation
$(\rho- \rho_a)$	Correlation mismatch
S	Entropy
σ^2	Debye Waller factor
σ_i	Occupational variables
σ, θ, P	Topologically closed packed
t	Exposure time
T	Temperature
Te	Tellurium
T_s	Spinodal ordering temperature
U	Internal energy of the system
$V(r)$	Pair interaction energies

V_{Cr}, V_{Mo}	Vegard's coefficients for Cr and Mo, respectively
W	Tungsten
x	Characteristic diffusion distance
ξ_{γ}^{Φ}	Cluster function
ξ_{i}	Point correlation
ξ_{ij}	Pair correlation
y	Number of atoms in a cluster
Z	Partition function

List of Figures

Chapter 1

Chapter 2

Chapter 3

Chapter 4

Chapter 6

List of Tables

Chapter 5

Chapter 6

Chapter 1 : Introduction

1.1 Background

Ni-Mo-Cr based alloys have extensive applications in different sectors such as petrochemical industries, hydropower, space technology, nuclear energy program, etc. [1-4] owing to their excellent high temperature mechanical strength, superior resistance against oxidation and corrosive attack in various media and acceptable radiation stability [1-5]. With the inclusion of molten salt reactors (MSR) and supercritical water reactors (SCWR) in Generation IV reactors [3-4, 6-8], there is a renewal of interest in examining the properties of Ni-Mo-Cr alloys which have emerged as a potential candidate for use as structural materials in these reactors where high temperature, corrosive environment and extensive radiation fields are prevalent.

Ni-Mo-Cr alloys considered for applications in MSR are solid solution strengthened alloys. One of them named Hastelloy N with low Mo (15-16 wt.%), Cr (6-8 wt.%) content was developed by Oak Ridge National Laboratory (ORNL) in 1950s for the molten salt reactor program [9-10]. This Ni-based alloy was chosen over the conventional Fe-based alloys as pure nickel shows good resistance to stress corrosion cracking (SCC) in chloride environments and is also fairly compatible with fluorides [9-11]. Due to the lack of required high temperature strength in Ni, Molybdenum (Mo) is added for solid solution strengthening, high temperature creep resistance and resistance to corrosion in reducing media such as fluoride melt [9-11]. Chromium (Cr) also imparts solution strengthening as well as provides oxidation resistance. The Mo and Cr contents are thus limited to <20 wt.% and <10 wt.%, respectively, to limit spalling of mixed oxide $NiMoO_4$ and void formation due to Cr depletion by fluoride melt [9-11].

For the long-term service of this structural alloy in a nuclear reactor, it is necessary to understand the phase transformation mechanisms in the alloy at the operating temperatures (~923-1123 K). A study of binary Ni-Mo and Ni-Cr alloys as well as Ni-Mo-Cr ternary phase diagrams (Fig. 1.1(a)-(b)) suggest quite a few interesting possibilities of phase transformations, namely, precipitation of long range ordered (LRO) precipitates [12-16]. In both Ni-Mo (8-33 at.% Mo) and Ni-Mo-Cr alloys, the phenomenon of short range ordering (SRO) has been observed. The characteristic features of the SRO state have been identified to be the weak diffused diffraction spots at {1 ½ 0} positions and their absence at {210} positions in the selected area diffraction (SAED) patterns. The marked difference between the SAED patterns from the SRO and the long range ordered (LRO) structures, which develops upon prolonged ageing, attracted the attention of several investigators [13-14, 17-22]. These alloys are often designated as {1 ½ 0} type alloys. In these alloys, several competing superlattice structures having close symmetry relationships with the parent disordered face centered cubic (fcc) structure and, possibly, nearly equal formation energies are present. For example, in the Ni-Mo system, the equilibrium Ni_4Mo shows an ordered $D1_a$ structure with ordering transition at ~1140 K [20, 23]. At the Ni-33 at.% Mo composition, the ordered Ni_2Mo with Pt_2Mo type structure appears as a metastable structure. While in Ni-Cr alloys, formation of the equilibrium Ni_2Cr (oP6 phase) occurs at temperatures ~873 K [24-25], but Ni_4Cr is not observed experimentally. In ternary Ni-Mo-Cr system, with high Cr+Mo content (> 30 wt.%), Pt_2Mo type $Ni_2(Cr,Mo)$ and/or topologically close packed (TCP) phases, *viz.*, σ, θ and P are formed at temperatures < 900 K [26-27]. The formation of different LRO structures in this system is dependent on the Mo/Cr ratio [28].

The isothermal section of ternary Ni-Mo-Cr phase diagram at 1473 K (Fig. 1.1(b)) shows that the austenite γ-phase field extends upto ~75 at.% Ni on Mo side and ~45 at.% Ni on Cr side [15, 29] and most of the commercial alloys including Hastelloy N fall in this region. These alloys are mainly designed with the objective that the alloy remains in a single phase for extended periods at operating temperatures and is, therefore, not expected to show any ordering transition or precipitation reaction. However, taking the cue from the studies on binary Ni-20 at.% Mo alloy [18-20], the prolonged exposure of these alloys in the medium to high temperature regime in a radiation environment, may lead to the formation of coherent ordered precipitates. With the ternary addition of Cr, along the tie line of Mo+Cr~20 at.%, the stabilities of competing ordered phases may change depending on the Mo/Cr ratio. Though the binary counterpart of this alloy, Ni-20 at.% Mo has been extensively studied over past fifty years [18-20, 30-32], no such exhaustive study is performed on the ternary alloys especially in the composition range of Cr+Mo ~20 at.%.

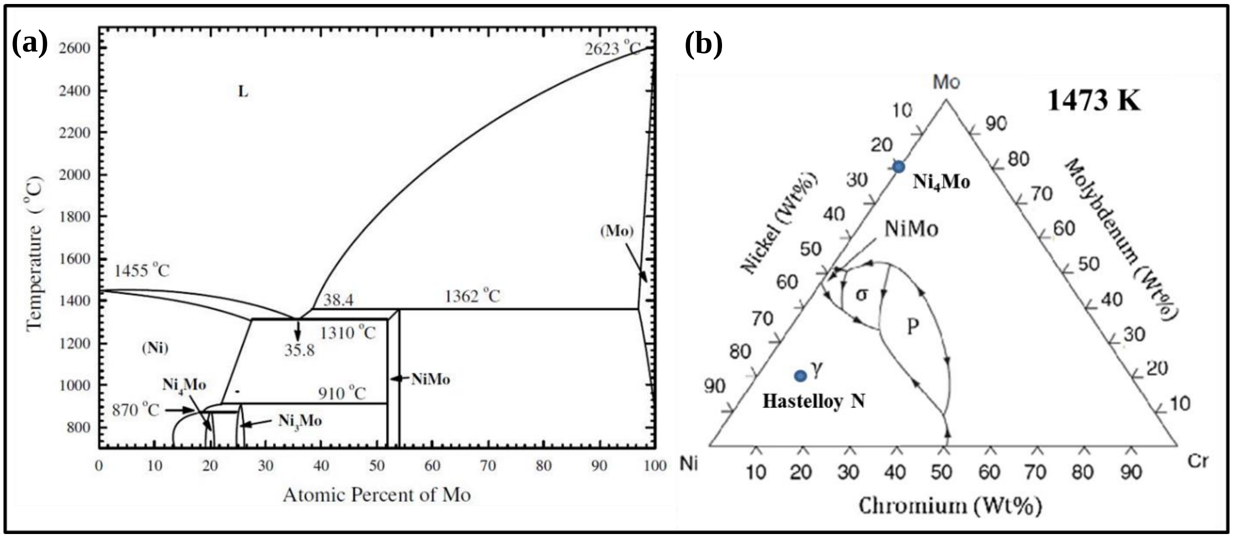

Fig. 1.1: Phase diagram for (a) Ni-Mo [12] and (b) Ni-Mo-Cr system [15].

In addition to high temperature, the alloy is subjected to an intense field of high-energy neutrons (neutron flux~10^{13} n cm^{-2} s^{-1}, damage ~100 dpa) [3-10, 33-34], fission product build-up particularly, tellurium, temperature (650-850 °C) [3-10, 35-36], corrosive environment of fluoride salts (UF_4 containing fuel salt and LiF-NaF-KF type candidate coolant salt) [3-10, 37-41] in a reactor environment. Degradation of Ni-Mo-Cr alloy in this environment can lead to reduced performance, and in some cases, sudden failure. Thus, the safe operation and operating life of a nuclear power reactor rely to a great extent, on the service performance of structural materials. The alloy, earlier used for experimental MSR was meant for operating temperatures < 973 K. However, MSR in Gen IV initiative aims at operating temperatures of ~1123 K and also in the environment of new salts. Hence the compatibility of Ni-Mo-Cr alloy with fluoride salt and Te fission products need to be re-assessed. The effect of temperature mainly in terms of the ordering transformations, corrosion and fission product interactions in Ni-Mo-Cr alloys chosen for MSR are briefly discussed in the sections 1.2-1.5.

1.2 Brief overview of molten salt reactors

Molten salt fuelled reactors commonly known as molten salt reactors (MSR) (Fig. 1.2) uses molten fluoride- based salts as fuel, e.g., UF_4, PuF_3 and fluorides of minor actinides and/or fertile elements such as ThF_4 are dissolved in LiF solvent/primary coolant in suitable concentration [3-10, 40-42] depending upon the desired application, *viz.*, breeder, burner, etc. The blanket salt if any, and fuel salt are circulated through individual heat exchangers. Heat generation in reactor vessel is controlled by circulating a secondary coolant which is also a molten salt through the intermediate heat exchangers [42].

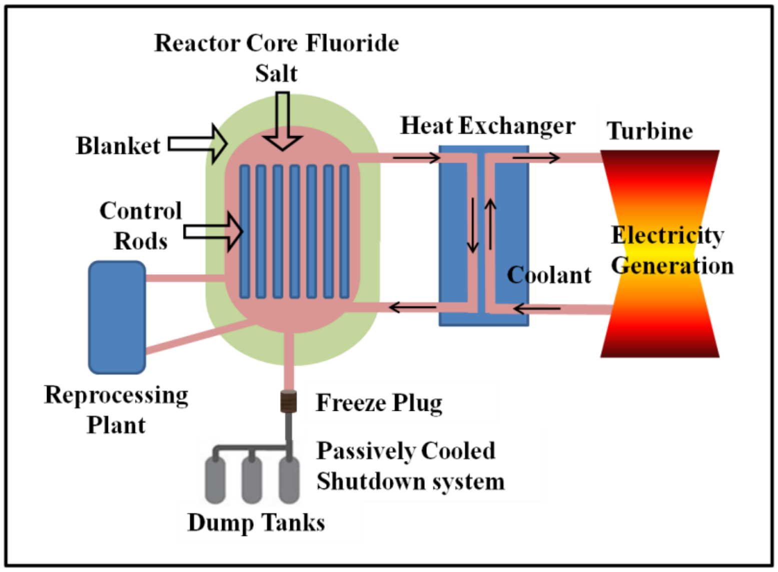

Fig. 1.2: Schematic diagram of a MSR [6].

The initial research on MSR started with 2.5 MWth aircraft reactor experiment (ARE) operated in 1950's at Oak Ridge National Laboratory (ORNL) [7-11, 42] followed by 8 MWth Molten salt reactor experiment (MSRE) in a test thermal reactor which was operated from 1965 to 1969 using fuel salt LiF-BeF$_2$-ZrF$_4$-^{233}UF$_4$/^{235}UF$_4$/^{239}PuF$_3$ (65-29-5-1 mol.%), pyrolytic graphite moderator, molten 2LiF-BeF$_2$ salt (66-34 mol.%) secondary coolant and a low Cr - high Mo containing Ni based alloy (INOR 8) as structural material. MSRE showed that the actinide fission products are stable in molten salt and established the feasibility of uranium recovery [7-11, 42-43]. The favourable experience gained with ARE and MSRE led to the design of a prototype 1000 MWe molten salt breeder reactor (MSBR) with a thermal spectrum graphite moderated core, and thorium–uranium fuel cycle with operating temperatures < 973 K [7-11, 42] using LiF-BeF$_2$-ThF$_4$-UF$_4$ (72-16-12-0.4 mol.%) as fuel salt and NaF-NaBF$_4$ (8-92 mol.%) as the secondary coolant [42]. However, the applicability of molten salts for use at extreme temperatures was not explored extensively during that time and the program was stopped abruptly in favour of fast breeder reactor program. Nonetheless, a marked resurgence of interest in MSR is observed in recent years [2-3, 7-

11, 42] as indicated by its inclusion in the Gen IV initiative. A schematic roadmap of MSR research with time is presented in Fig. 1.3.

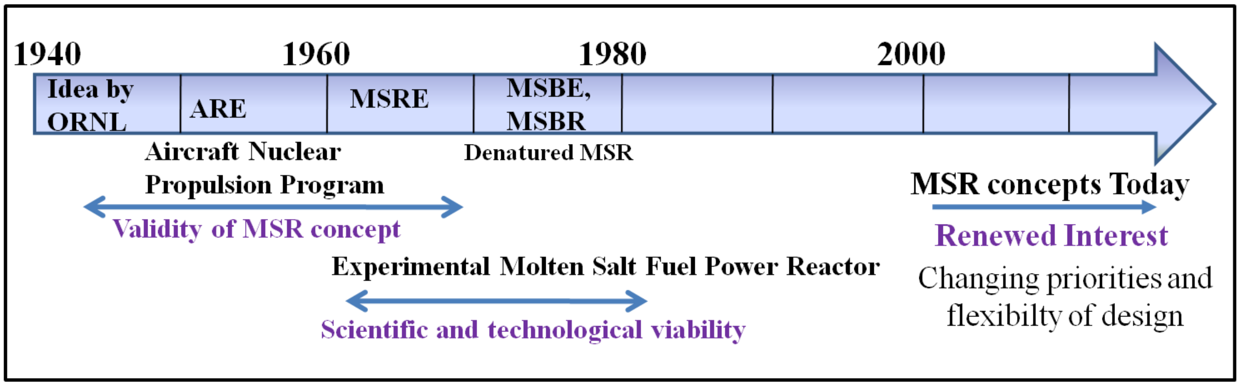

Fig. 1.3: Roadmap of development of MSR [3].

The principal advantages of MSR over solid fuel element system are that it is inherently safer as the fuel can easily be cooled by draining it in criticality safe dump tanks at ambient pressure without any possibility of core melt down or radiation damage. The fission products generated are less in quantity and can be reprocessed online. MSR can achieve higher thermal efficiency due to higher operating temperatures, negative temperature and void coefficients [7-10, 42-43]. One of the attractive features of the molten salt system is that a variety of reactor types can be considered to cover a range of applications such as breeders, transuranic waste burners or provide energy for industrial applications like hydrogen production [42-43] and desalination. MSR can be operated with different types of fissile elements, and/or neutron spectrum (Table 1.1).

Table 1.1: **Different types of MSR concepts [3].**

Class	Concepts	F/T	Fuel cycle	Comments
MSR Breeder	MSBR	T	U-233/Th	BR >1.05
	AMSTER-B	T	U-233/Th	BR > 0.95
	REBUS	F	U/Pu	
	FUJI	T	U-233/Th	
	TMSR	T or F	U-233/Th	BR >1
MSR-Burner	AMSTER-I	T	U-Pu-MA	
	SPHINX/ MOZART	F	Pu-MA	Feedback reactivity coefficient <0

1.3 Indian program on MSR

Indian molten salt breeder reactor (IMSBR) is an attractive option for thorium utilization in the third stage of Indian Nuclear Power program with the goals of enhanced safety, efficient resource consumption and high efficiency power conversion (~35%) [44-46]. ^{233}Pa, an intermediate isotope formed during conversion of ^{232}Th to ^{233}U [44-46] is mostly lost in solid fuel reactors by neutron absorption (Fig. 1.4). Online removal of ^{233}Pa in MSR allows it to decay to ^{233}U thus ensuring a self-sustaining thorium utilization in third stage [9].

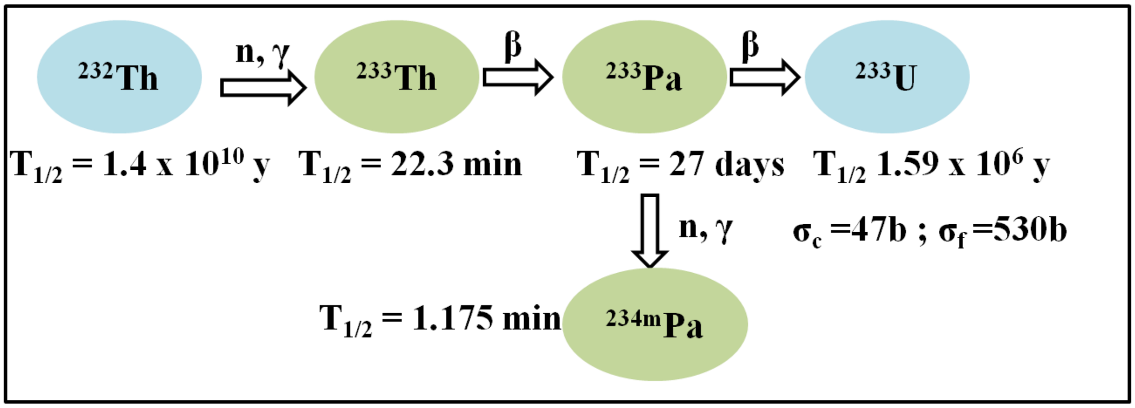

Fig. 1.4: Conversion of ^{232}Th to ^{233}U [9].

Two reactor concepts – Loop-in-tank and pool type concepts are being developed for a power level of 850 MWe. The major advantages of such breeder reactors are that breeding is possible over a wide range of neutron spectrum and self-sustaining thorium reactor possible with minimal fissile inventory [45]. A schematic of proposed loop-type IMSBR is given in Fig. 1.5.

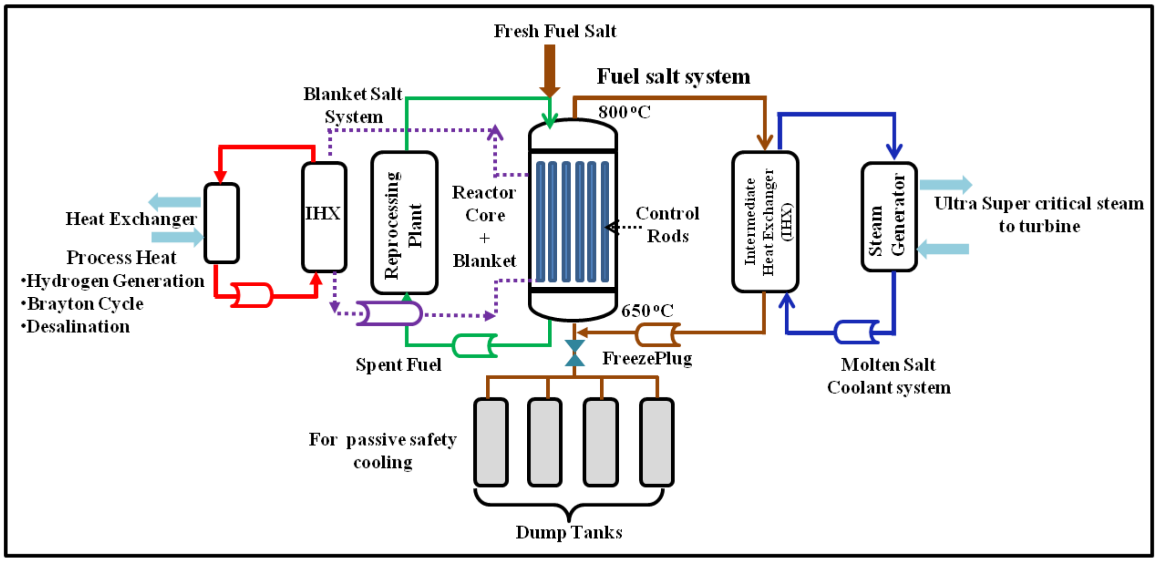

Fig. 1.5: Preliminary layout of the proposed loop-type IMSBR [45].

1.4 Ni-Mo-Cr based alloys for MSR applications

The potential candidate for use as structural materials must satisfy the criteria of high temperature strength, stability against thermal creep and high temperature oxidation, radiation stability upto displacement damage of ~ 100 dpa, good neutronic properties and a high degree of chemical compatibility with molten salt [7-10]. In general, the structural alloy is compatible (noble) with the salt if the difference in the Gibbs free energy of formation of the salt and the container material is >20 kcal mole^{-1}°C^{-1} [47]. The tendency for corrosion in molten fluoride salts is increased in the following order: Ni, Co, Fe, Cr, Al; while the refractory metals Nb, Mo, and W could be expected to be relatively free from attack. The corrosive environment can be aggravated by presence of impurities and the structural alloy must be able to withstand such harsh operating conditions [38, 47].

The Zr-based alloys though have low neutron capture cross-section, acceptable mechanical and corrosion resistance in aqueous environment but an increased susceptibility to hydrogen embrittlement, allotropic phase changes at elevated temperatures (α→β phase) as well as poor creep and oxidation properties render them unfit for use in MSR [48-49]. Similarly, stainless steels considered for fast reactors have unacceptable long term chemical compatibility with the molten fluoride salt [50]. ORNL research on the material selection for their aircraft experiment lead to the development of INOR-8 (Hastelloy N) with an optimized composition of Ni-16 wt.% Mo-7 wt.% Cr-5 wt.% Fe suitable for operations in the range of 973 K [46-49]. With the renewed interest in MSR, the interest in candidate alloys has resurfaced and the various Ni-Mo-Cr based alloys that are being considered for present day applications are summarized in Table 1.2.

Table 1.2: Chemical composition of selected candidate Ni-based alloys considered for use in different types of MSR [39].

Alloy Name	**Elemental Composition (wt.%)**					
	Mo	**Cr**	**Fe**	**Mn**	**C**	**Ni**
Hastelloy N	15.7	7.1	3.7	0.6	<0.05	Balance
GH3535	17.1	7.0	4.0	0.8	<0.02	Balance
MONICR	17.4	6.8	0.7	0.06	<0.002	Balance

1.5 Phase transformations in Ni-Mo-Cr based alloys

Binary and ternary Ni-Mo based alloys under the service conditions of high temperature show interesting phase transformations, namely, precipitation and chemical ordering which influence the microstructure as well as the mechanical and the corrosion properties of the alloys [18-30] such as improved hardness, reduced fracture toughness, increased hydrogen embrittlement susceptibility and SCC [18-30]. Moreover, the transformation mechanism as well as the kinetics is governed by the alloy composition and ageing temperature. The binary counter part of Hastelloy N (Mo+Cr ~20 at.%) is Ni_4Mo (Mo-20 at.%) alloy which forms coherent LRO precipitates of $D1_a$

(Ni_4Mo) structure. Depending upon the Mo content (8-33 at.%), the binary Ni-Mo alloys undergo different type of transformations controlled by a competition between several fcc based superlattices and a SRO characterized by the presence of intensity maxima at {1 ½ 0} positions in the SAED pattern [22-24]. Commercial Ni-Mo-Cr alloys with high Cr+Mo content (> 30 wt.%) lead to the formation of coherent LRO precipitates of Pt_2Mo type (Ni_2Mo; $Ni_2(Mo,Cr)$) structures upon ageing [25-29]. However, ordering transformations in Hastelloy N is not being investigated at all. The order-disorder phase transformations in Ni-Mo and Ni-Mo-Cr alloys are briefly discussed below.

1.6 Ordering reactions in binary Ni-Mo alloys

Ni-Mo alloys (8-33 at.% Mo) exhibit several competing first order ordering processes resulting in stable and metastable fcc superlattice structures, *viz.*, $D1_a$ (Ni_4Mo), stable DO_a and metastable DO_{22} (Ni_3Mo), Pt_2Mo (Ni_2Mo) type configurations as well as a short wave length concentration modulated structure with wave vector, **k**= <1½0> which is a candidate for second order transition [14,18-20,23,30-32]. The crystallographic properties of various Ni-Mo intermetallics are summarized in Table 1.3 [14].

Table 1.3: Properties of stable and metastable intermetallics in Ni-Mo system [14].

Phase	**e/a**	**Mo conc. (at.%)**	**Crystal structure**	**Lattice Parameter (Å)**			**Space group**
				a	b	c	
α-Ni	10	0	FCC	3.524	3.524	3.524	$Fm\bar{3}m$ (225)
Ni_8Mo	9.55						4/m2/m2/m
β-Ni_4Mo	9.2	20	BCT	5.727	5.727	3.566	I4/m (87)
γ-Ni_3Mo (DO_a)	9.0	25	HCP	5.064	4.224	4.448	Pmmn (59)
δ-NiMo ($L1_0$)	8.0	51-52.5	Orthorhombic	9.108	9.108	8.852	P4/mmm (123)
Mo	6.0	98.9-100	BCC	3.147	3.147	3.147	
Ni_2Mo	8.67	20-52.5	BCO	2.492	7.475	3.524	Immm (71)
Ni_3Mo ($L1_2$)	9.0	25	Cubic				$Pm\bar{3}m$ (221)
Ni_3Mo (DO_{22})	9.0	25	Tetragonal				I4/mmm (139)
Ni_2Mo_2	8.0		Tetragonal				$I4_1$/amd (141)
NiMo ($L1_1$)	8.0	51-52.5	Rhombohedral				$R\bar{3}m$ (166)

The quenched-in state of SRO in binary Ni-Mo shows the intensity maxima at only $\{1\frac{1}{2}0\}_{fcc}$ positions and complete absence of intensity at $\{210\}_{fcc}$ and its equivalent positions. Thus, the state of SRO is significantly different from a structure which contains micro-domains of any of the competing LRO structures, namely, $D0_{22}$, Pt_2Mo or $D1_a$ [20]. The atomic structure of such a state of SRO has been a subject of considerable controversy. The development of LRO structures from SRO often proceeds via intermediate stages. In case of an alloy of Ni_4Mo composition, LRO can evolve either continuously (a lower aging T) via the SRO state or by the first order transformation mode (predominant at higher aging T) yielding six different variants of $D1_a$ [18-20, 30-32]. An alloy of Ni_3Mo composition, on the other hand, initially separates into a coherent phase mixture of Ni_4Mo ($D1_a$) and metastable Ni_2Mo (Pt_2Mo-type) ordered phases which on prolonged ageing results in the formation of γ-Ni_3Mo. The stoichiometric DO_{22} structure is formed under special conditions when Mo is substituted by a ternary element such as Ta or Al and ageing treatment is carried out below 900 K [32]. All these competing superlattice structures, *viz.*, SRO state, $D0_{22}$, Pt_2Mo or $D1_a$ can be described in terms of periodic stacking of pure Ni layers and pure Mo layers along {420}γ atomic planes [20] (a) {1 ½ 0} structure Ni_2Mo_2: 2 Ni layers followed by 2 Mo layers (b) Ni_3Mo (DO_{22} structure): 3 Ni layers followed by 1 Mo layer (c) Ni_2Mo (Pt_2Mo structure): 2 Ni layers followed by 1 Mo layer and (d) Ni_4Mo (D1a structure): 4 Ni layers followed by 1 Mo layer. Alternatively, each of these ordered structures can be generated by introducing the tiles as indicated in Fig. 1.6.

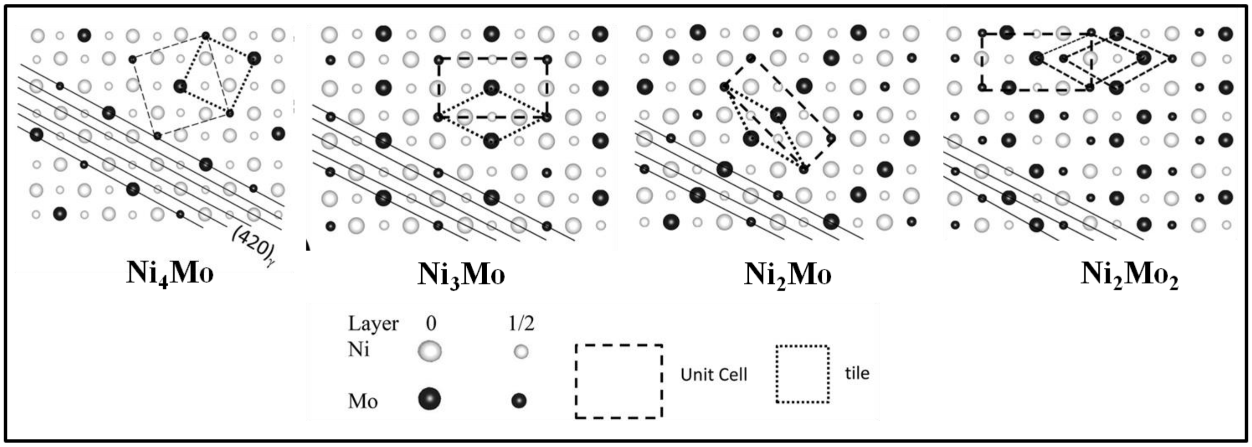

Fig. 1.6: $[001]_\gamma$ projection of the competing fcc superlattice structures for Ni-Mo system. Dashed lines show the unit cells while the tiles in the sub unit cell clusters are marked by dotted lines [20].

1.6.1 Atomic description of SRO

Several structural descriptors are proposed [14] to explain the nature of SRO which are briefly discussed as follows

(a) Static concentration wave (SCW) model

In this model, the distribution of atoms over the alloy lattice is described in terms of superposition of static concentration waves of different wavelengths and amplitudes along specific crystallographic directions [51]. The amplitudes are represented by the Fourier transformation of the local composition variation. Any ordered structure is then represented by a specific set of concentration waves whose wave vectors are given by the reciprocal-lattice vectors of the superlattice reflections localized within the first Brillouin zone of the disordered matrix [14, 23, 25].

The SCW model was first used by de Fontaine [52-53] to explain the <1½0> spots in Ni_4Mo alloy where the free energy of the system expressed in terms of SCW amplitudes expanded in Taylor series around disordered state by considering pair interaction energies V(r). For small amplitudes, the free energy minimum was obtained from the extrema of V(r) and one of the solutions for the fcc solid solution was {1½0}. The SRO was then described in terms of low amplitude static concentration waves (SCWs) with **k**-vectors ending at ⟨1½0⟩ and equivalent positions in the reciprocal space. Khachaturiyan [51, 54] and de Fontaine [52-53] further proposed that these wave vectors are associated with the hypothetical ordered structure N_2M_2. This N-N-M-M stacking of atom along the <420> planes gives rise to the observed SRO state. Similarly, the concentration wave with wave vector either **k** =1/5<420>, **k** =1/4<420> or **k** =1/3<420> are respectively associated with $D1_a$, DO_{22}, Pt_2Mo in the γ-fcc lattice [55-57] as shown in Fig. 1.7. The amplification of the amplitudes of the concentration waves is driven by supercooling (T_s-T) where T_s is the spinodal ordering temperature. Since, T_s is highest for the N_2M_2 structure, hence formation of SRO structure is favoured the most amongst all the competing superlattices [55].

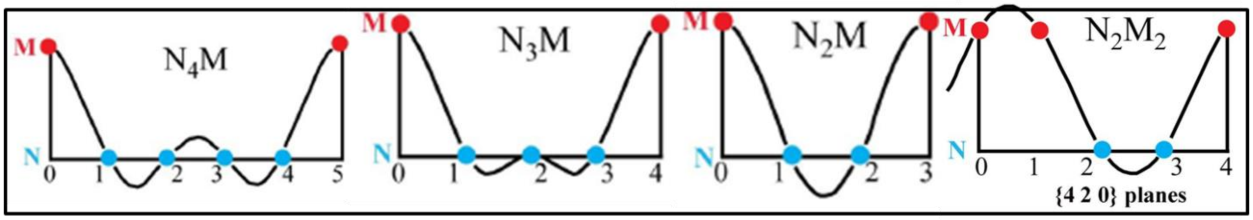

Fig. 1.7: Different types of SCW in fcc lattice along the {420} planes generating Pt_2Mo, DO_{22} and $D1_a$ structures [25].

(b) Microdomain Model

In this model, the existence of SRO state is associated with the presence of perfectly ordered microdomains of different equilibrium and metastable LRO structures with sharp interfaces in the disordered matrix. These microdomains can form continuous array or may remain dispersed in the disordered matrix [31-32]. Experimental evidences by Hata *et al.* [31-32, 58] and Monte Carlo (MC) calculations by Kulkarni *et al.* [59-60] suggest that these microdomains or sub-unit cell clusters are mainly a mixture of, Pt_2Mo, DO_{22} and $D1_a$ structures in case of Ni_3Mo and Ni_4Mo alloys [19]. This is plausible since Arya *et al.* [61] showed that the free energies associated with these different LROs are nearly equal. Banerjee *et al.* [14, 20, 62] treated microdomain model as the atomistic analogue of the SCW model thereby showing the equivalence between two models.

(c) Change in chemical interaction:

Ustinovshikov *et al.* [63] suggested that the <1½0> SRO state is attributed to the phase separation taking place at high temperature in which precipitates of highly dispersed Mo atoms occurs at temperatures above the liquidus of Ni-Mo system. This phase separation occurs mainly due to the change in sign of chemical interaction between the dissimilar atoms and varies with temperature and/or solute concentration.

1.6.2 Crystallographic aspects of LRO in Ni_4Mo

The equilibrium Ni_4Mo phase ($D1_a$ structure), which has an order–disorder transition temperature of 1140 K, has a body-centered tetragonal (BCT) structure having space group I4/m and c/a ratio of 0.986 (Fig. 1.8). The unit cell of $D1_a$ has 8 Ni atoms and 2 Mo atoms having the following fractional coordinates as follows

Mo: $0\ 0\ 0; \frac{1}{2}\frac{1}{2}\frac{1}{2}$; Ni: $\frac{1}{10}\frac{3}{10}\frac{5}{10}; \frac{2}{10}\frac{6}{10}1; \frac{3}{10}\frac{9}{10}\frac{5}{10}; \frac{4}{10}\frac{2}{10}1; \frac{6}{10}\frac{8}{10}1; \frac{7}{10}\frac{1}{10}\frac{5}{10}; \frac{8}{10}\frac{4}{10}1; \frac{9}{10}\frac{7}{10}\frac{5}{10}$

From the atomic positions, the expressions for structure factor corresponding to the fcc matrix and superlattice lines are obtained as

$$F_f^{D1a} = 2(f_{Mo} + 4f_{Ni}) \text{ for H-K+L =2n; (n=0,1,…)} \qquad 1.1$$

$$F_s^{D1a} = 2\eta(f_{Mo} - f_{Ni}) \text{ for H+K+L =2n; (n=0,1,…) and } 2H+K \neq 5n \qquad 1.2$$

Where f_{Mo} and f_{Ni} are atomic scattering factors for Mo and Ni, respectively and $\boldsymbol{\eta}$ is the long range order parameter. HKL and hkl are the Miller indices for the planes corresponding to $D1_a$ and fcc matrix, respectively.

The relationship between the H,K,L planes of $D1_a$ and h,k,l planes of the fcc matrix is expressed in terms of matrix equation [60]

$$\begin{bmatrix} h \\ k \\ l \end{bmatrix} = \frac{1}{5}\begin{bmatrix} 3 & -1 & 0 \\ 1 & 3 & 0 \\ 1 & 0 & 0 \end{bmatrix}\begin{bmatrix} H \\ K \\ L \end{bmatrix}$$

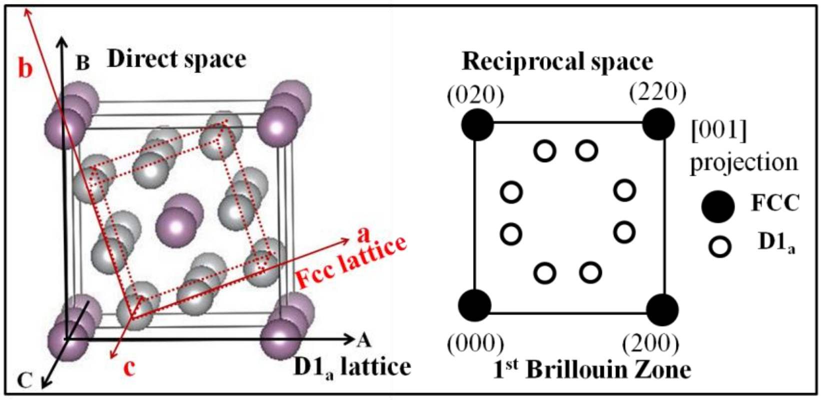

Fig. 1.8: Unit cell of $D1_a$ structure showing its orientation relationship with the parent fcc matrix and its simulated diffraction pattern along [001] zone axis.

The c-axis of $D1_a$ unit cell is either parallel or anti parallel to the any one of the axes of disordered fcc matrix and the a-axis of the $D1_a$ unit cell consequently aligns itself along the appropriate <120> directions [64] resulting in six variants of the $D1_a$ structure which can nucleate with equal probability.

1.7 Ordering reactions in Ni-Mo-Cr alloys

Numerous study on ordered $Ni_2(Cr,Mo)$ precipitates in commercial alloys propose substitution of Mo atoms by Cr in this structure [14, 25, 65]. The transformation proceeds by a mechanism of continuous ordering at low temperature (< 973 K), but changes to first order nucleation and growth process at higher temperature (> 1023 K) in Haynes Alloy 242. Aged C-22HS alloy show only the presence of superlattice spots at every $^{1}/_{3}\{220\}$ and $^{1}/_{3}\{420\}$ fcc reflection positions, characteristic of LRO Ni_2Mo phase [65-66]. Studies on Ni–Mo–Cr ternary alloy having about 70 at.% Ni, 24 at.% Mo and 6 at.% Cr show that ageing at temperatures upto 873 K produces coherent domains of Pt_2Mo type (Ni_2Mo) and $D1_a$ (Ni_4Mo) structures from diffuse SRO $\{1\ ^{1}/_{2}\ 0\}$ intensities. Ageing at 973 K results in the formation of DO_{22} plates which partially consume the Pt_2Mo and $D1_a$ domains formed initially and complete decomposition of the $\{1^{1}/_{2}0\}$

SRO γ matrix into a mixture of γ+DO_{22} plates results at 1073 K [21]. Another study, however, suggests that with a Ni–Mo–Cr alloy containing 8 wt% Cr, Ni_2(Mo,Cr) phases are unlikely to form when the Mo content is below 22 wt% (Mo/Cr =2.75) [67]. The formation mechanism and kinetics of development of Pt_2Mo type Ni_2(Mo,Cr) is thus dependent on the Mo/Cr content and is schematically presented in Fig. 1.9.

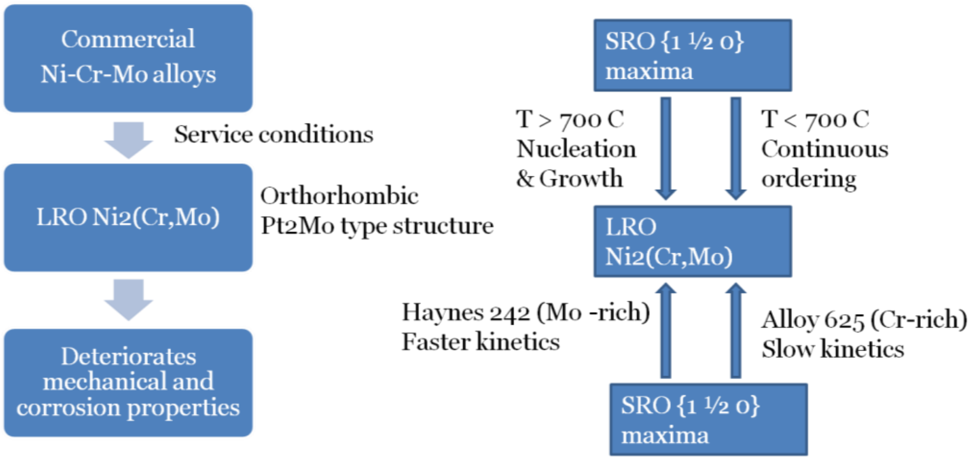

Fig. 1.9: Effect of temperature on the formation mechanism and kinetics of ordered precipitate Ni_2(Cr,Mo) in various Ni-Mo-Cr alloys.

1.7.1 Crystallographic aspects of Ni_2(Cr,Mo) LRO phase

The ordered Ni_2(Cr,Mo) phase is body-centered orthorhombic structure with space group *Immm*. The prototype of this structure is a Pt_2Mo type (N_2M structure) and contains 6 atoms per unit cell. The unit cell of Pt_2Mo structure with respect to disordered fcc unit cell is presented in Fig.1.10. The fractional coordinates for Ni and Mo atoms are as follows:

Mo: $00\,0;\frac{1}{2}\frac{1}{2}\frac{1}{2}$; Ni: $0\frac{1}{3}0;\ 0\frac{2}{3}0;\ \frac{1}{2}\frac{1}{6}\frac{1}{2};\ \frac{1}{2}\frac{5}{6}\frac{1}{2};$

Substituting these values in the formulae for structure factor calculation, the expressions deduced for principal and superlattice lines are [25]

$$F_f^{Pt2Mo} = 2(f_{Mo} + 2f_{Ni}) \text{ for H-K+L =2n; (n=0,1,…) and K=3,6,...} \qquad 1.3$$

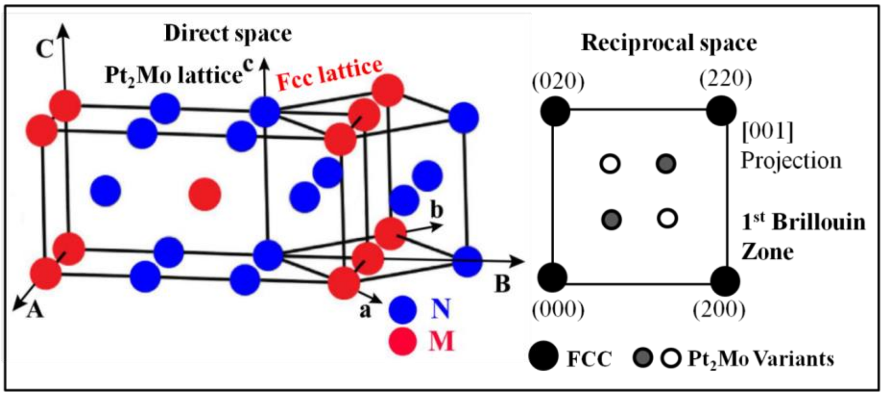

Fig. 1.10: Unit cell of Pt_2Mo structure showing its orientation relationship with the parent fcc matrix and its simulated diffraction pattern along [001] zone axis [25].

$$F_S^{Pt2Mo} = 2S(f_{Ni} - f_{Mo}) \text{ for H+K+L =2n; (n=0,1,…) and K} \neq 3,6,\ldots \qquad 1.4$$

$$F^{Pt2Mo} = 0 \text{ for H+K+L= odd} \qquad 1.5$$

The relationship between the H,K,L planes of Pt_2Mo and h,k,l planes of the fcc matrix is expressed in terms of matrix equation

$$[H \quad K \quad L] = [h \quad k \quad l] * \frac{1}{3}\begin{bmatrix} 3 & -3 & 0 \\ 1 & 1 & 0 \\ 0 & 0 & 1 \end{bmatrix}$$

The c-axis of the Pt_2Mo unit cell can align itself along any one of the three axes of the disordered fcc (A1 structure) unit cell. While the remaining two axes will align themselves along appropriate <110> fcc directions resulting in the formation of six orientational variants of the ordered phase [64].

1.8 Performance of Ni-Mo-Cr alloy under simulated service conditions

In addition to high temperature, the performance and hence service life of Hastelloy N in is also affected by corrosion from fluoride melt and inter-granular embrittlement caused by fission product tellurium (Te) [7-10]. Different candidate fluoride salts are chosen for coolant applications in MSR, but LiF-NaF-KF salt having eutectic composition 46.5-11.5-42 mol.% [7-10] also known as FLiNaK salt has emerged as one of the most promising candidate material. Over past 60 years investigations have been carried out to study the compatibility of Hastelloy N with molten fluoride salts especially FLiNaK salt though the study still remains inadequate. The microstructural evolution of the alloy under these service conditions is briefly outlined below.

1.8.1 Compatibility of Hastelloy N with fluoride melt

Fluoride induced material corrosion is a thermodynamically driven dissolution process [47]. The corrosion of a pure metal Me (Ni, Fe or Cr) in an alkali fluoride MF (M=Li, Na, K) is given by

$$\mathrm{xMe} + \mathrm{yMF} \rightarrow Me_xF_y + \ yM \tag{1.6}$$

Comparing the Gibbs free energy of formation of the fluorides for different elements, the dissolution tendency of different elements in fluoride melt FLiNaK salt is found to follow the order: W (Least prone)<Mo<Ni<Co<Fe<Cr<Al<Na (Most prone). In the case of a pure salt in contact with the alloy, the alloy is corroded by the salt till the equilibrium is reached and the alloy does not corrode any further. However, in actual service conditions, the salt may contain impurities including oxidants, thermal gradients, salt flow rate, and galvanic coupling which will alter the reaction rate and the effect of each is briefly discussed as follows:

(a) <u>Impurity driven corrosion:</u> Oxidant impurities, such as H_2O, HF, residual metal oxides of metals, and other reducible ions present in salt easily accelerate the initial stages of corrosion, but once the impurities are exhausted, the linear relationship between time and corrosion is observed [69-70]. In this later stage of the process, corrosion is governed by the thermal gradients (Fig. 1.11).

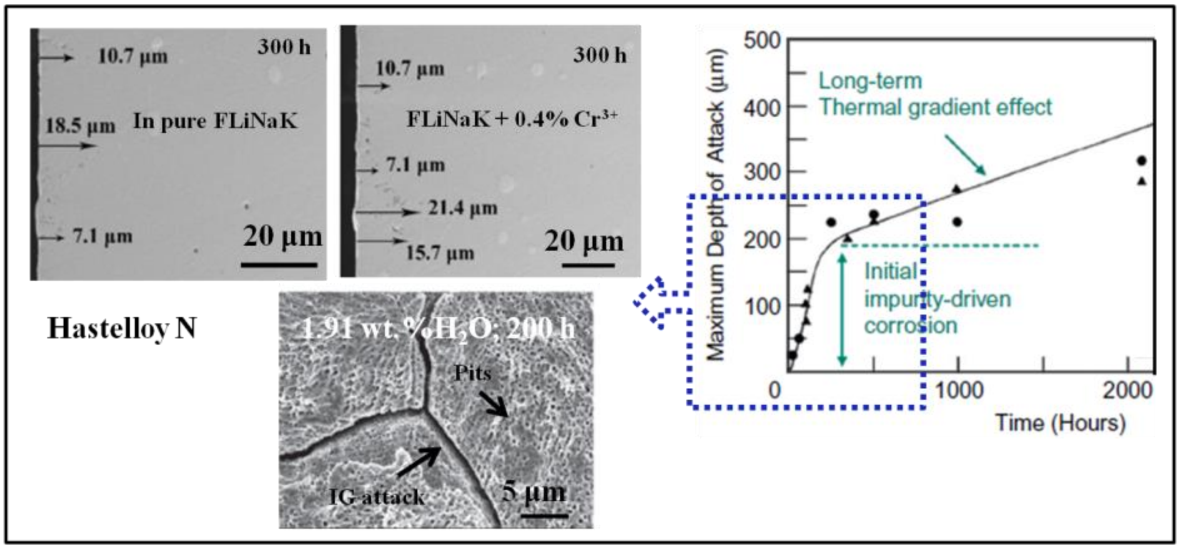

Fig. 1.11: Effect of Cr^{3+} ions and moisture in FLiNaK salt on the corrosion properties of Hastelloy N [69, 70].

Moisture is a deleterious contaminant which reacts with the salt fluorides to release corrosive HF that further aggravates the corrosive attack by reacting with alloy metals (M) according to following reactions:

$$\mathrm{MF(l)} + \mathrm{H_2O\ (g)} \rightarrow MOH\ (l)\ +\ HF(g) \qquad 1.7$$

$$\mathrm{xM} + \mathrm{y}H_2\mathrm{O} \rightarrow M_xO_y +\ yH_2 \qquad 1.8$$

Similarly, the metallic impurities are incorporated as fluorides in the salt and can react with Cr in the alloy since Cr is most prone to attack

$$\mathrm{MeF_2} +\ Cr \rightarrow CrF_2 +\ Me \qquad 1.9$$

The effect of moisture and impurities on the corrosion of Hastelloy N is studied by Ouyong *et. al* [69] Kondo *et al.* [50] and Yin *et al.* [70] reveals that higher moisture content, FeF_2 additions and Cr^{3+} in salt aggravated pitting and intergranular attack (Fig. 1.11).

(b) <u>Thermal gradient driven corrosion</u>: In Li, Na, K, U/F solvents, the equilibrium constant for reaction with Cr is temperature dependent and due to thermal gradient, the diffusivity and solubility of alloying elements at different regions are different. These two effects lead to removal of chromium from the alloy in regions of highest temperature and formation of dendritic chromium in the cold regions. Voids are formed in the alloy with uniform distribution due to selective dissolution of Cr. Rate of Cr diffusion into melt governs the rate of corrosive attack [38].

(c) Galvanic corrosion: Presence of dissimilar metals in contact with melt or thermal gradients with the melt can lead to a change in the corrosion potentials and lead to galvanic corrosion, e.g., Ye *et al.* [68] reported that the $M_{12}C$ carbides in Hastelloy N severely corroded due to Cr and Mo concentration gradient amongst the carbides. Similarly, the crucible element used for performing the experiments can also enhance the corrosion attack [38].

1.8.2 Compatibility of Hastelloy N with fission product tellurium

It is essential to study the fission product compatibility in this case since the fission product is directly exposed to the containment vessel which is different from the conventional scenario where the fission products remain confined within the solid fuel element. Early studies by ORNL on MSRE materials showed formation of surface cracks in the alloy after four years of operation which were attributed to fission product tellurium [6-12]. Such Te-induced cracking has been observed for other cladding materials such as stainless steel 316 L and Zircaloy 4 [7-10]. Though corrosion studies on Ni-based alloys caused by fluorides are widely studied, but a limited knowledge is available on the Te induced microstructural degradation of Ni-Mo based alloys.

Preliminary studies indicated that Te diffuses from the fuel salt into the alloy and resulted in grain boundary embrittlement [71-73]. The total fluence of Te deposited on the alloy surface was calculated based on the assumption of 30 years reactor operation life and it was estimated to be 2.9×10^{23} at/m^2 (60 g/m^2) [72-73]. Recent studies on Hastelloy N exposed to Te vapour at different temperatures indicate that Te diffuses mainly along the grain boundaries when T<1173

K and by lattice diffusion when T > 1273 K [74]. Te leads to formation of intergranular precipitates mainly in the form of brittle tellurides and/or low melting eutectic phases [57-59]. These precipitates, identified to be Ni-, Cr- and/or Mo- tellurides lead to crack formation and intergranular corrosion (IGC) (Fig. 1.12). Computational and Extended X-ray Absorption Fine structure (EXAFS) studies indicate weakening of Ni-Ni bonds by Te segregation along the grain boundaries and elongation of Ni-Te bonds as compared to Ni-Ni bonds [71, 75]. However, no study has been carried out to estimate relative stabilities of various Ni-Te phases. The available study on exact morphology, crystal structure and chemical composition of the tellurides formed is still ambiguous particularly with respect to the formation of nickel tellurides.

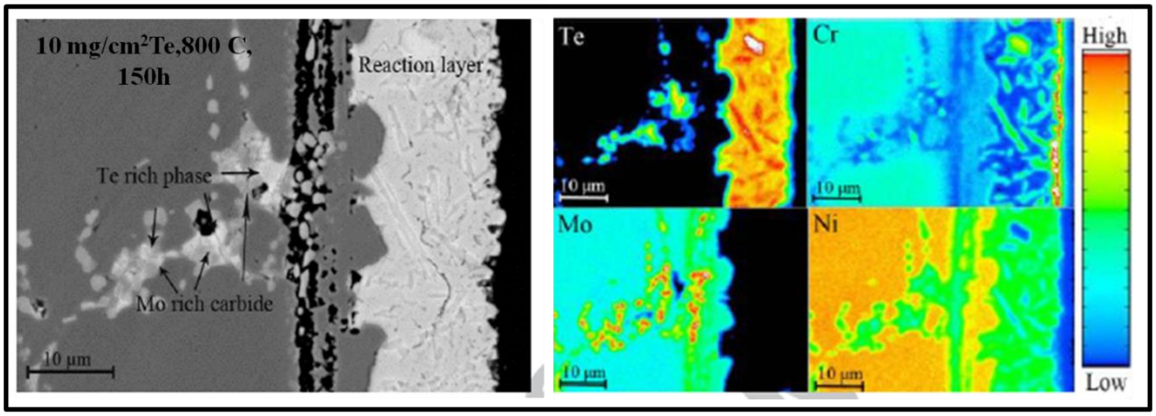

Fig. 1.12: Te induced corrosion in Hastelloy N [74].

1.9 Motivation

From the above literature review, it is evident that there are certain gaps in the existing study on Ni-Mo and Ni-Mo-Cr alloys, mainly, in terms of the ordering phase transformations which is limited only to the ordering characteristics of $Ni_2(Cr,Mo)$ phase. The LRO formation in binary Ni-Mo system with Mo=20 at.% is well studied, but an exhaustive study correlating the experimentally determined local structure with theoretically predicted structures along with the calculation of pair and multisite interaction energies dictating these ordering tendencies is lacking. Similarly, Hastelloy N, Mo+Cr~20 at.% is ternary equivalent of Ni_4Mo and thus by studying the ordering characteristics of the ternary alloy one can elucidate the role of Cr in altering the crystallography, stability and formation of LRO phases. Moreover, compatibility studies of Ni-Mo-Cr alloy with the molten fluoride shows selective Cr depletion and grain boundary attack. However, there appears no report which correlates the observed property of Cr depletion in impurity containing salt with the surface film characteristics which may alter the migration of elements between salt and the alloy. Similarly, the mechanism of grain boundary attack of the alloy by tellurium is still inconclusive and ambiguous in terms of the crystallography of the precipitates. Present study attempts to address these issues (Fig 1.13) and correlate the observed microstructure with the properties of the alloy.

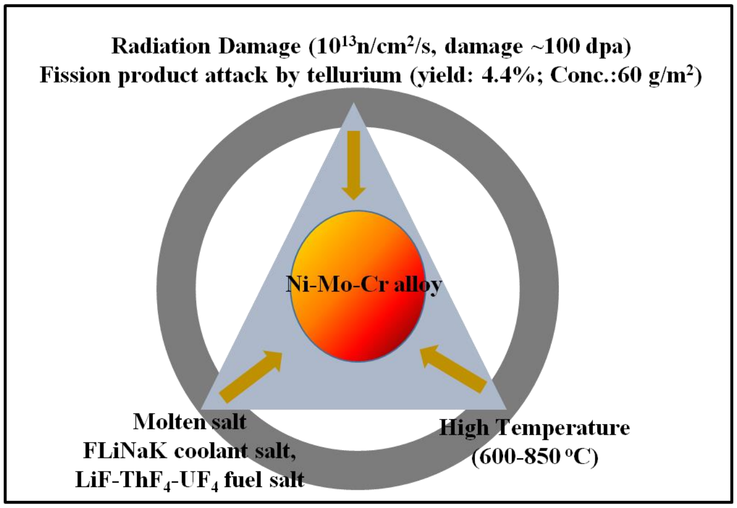

Fig. 1.13: Schematic of the operating environment in a molten salt reactor as seen by Ni-Mo-Cr based Hastelloy N assuming 30 y of reactor operation.

1.10 Broad Objectives of the present study

The present work, with the goal of comparing the ordering tendencies in binary Ni-20 at.% Mo and the ternary Ni- 16 wt.% Mo- 7 wt.% Cr alloy, has been taken up against the backdrop summarized above. Furthermore, the behaviour of the alloys in the simulated nuclear reactor environment has been investigated with an aim of establishing the correlations between observed properties under extreme environments with the microstructure, and addressing the following questions:

1. What is the nature of nearest neighbour configurations around Ni and Mo atoms in SRO, and LRO structure of Ni- 20 at.% Mo alloy? Is it possible to rationalize the observed ordering transformation sequence in terms of the nearest neighbour interaction energies?

2. To investigate the phase transformation behaviour of Ni-Mo-Cr alloy and address the specific issues: a) Is it possible to suppress the formation of ordered structures in the ternary alloy and, if so, can this be rationalized in terms of near neighbour interactions of the atomic species present?

b) What is the effect of Cr addition in Ni-Mo alloys on first nearest neighbour configurations?

c) Can the SRO structure which has earlier been characterized by X-ray, electron and neutron diffraction, and high resolution electron imaging be captured by the extended X-ray absorption fine structure (EXAFS) technique?

3. What is the role of surface films in altering the corrosion compatibility of Ni-Mo-Cr alloy, Alloy 690 and Alloy 693 with oxygen containing FLiNaK salt at elevated temperature? How the Mo atom alters the surface structure which mitigates the fluoride attack?

4. What is the nature of chemical compatibility of Ni-Mo-Cr alloy with simulated fission product tellurium? What is the phase evolution and crystallography of the Ni-rich tellurides and their subsequent role in degrading the alloy microstructure?

1.11 Thesis Layout

The thesis of present work comprises seven chapters. **Chapter 1** provides introduction and a detailed literature review pertaining to ordering transformations in Ni-based alloys and their behaviour in simulated service conditions, such as, fluoride melt and fission product tellurium, gaps in the existing study on the Ni-based alloys as candidate materials for MSR, motivation and objectives of the present study. **Chapter 2** lays out the details of experimental methodology being followed to fulfill the objectives of present study and describes the theoretical methodology adopted to study the ordering transformations. **Chapter 3-6** gives a detailed account of the results and their discussion in the light of available literature. Furthermore, the results obtained experimentally were correlated with the results obtained from theoretical calculations. **Chapter 7** presents an overall summary and conclusion for the present thesis and also provides a scope for further research based on this work.

Chapter 2 : Experimental and Theoretical Methodologies

2.1 Synthesis and treatments of Ni-Mo and Ni-Mo-Cr alloys

2.1.1 Alloy melting

The binary Ni-Mo (20 at.% Mo) and ternary Ni-16 wt.% Mo-7 wt.% Cr alloy buttons (henceforth named as Ni_4Mo and Ni-Mo-Cr alloy, respectively), each having a weight of 20 g were prepared in an arc melting furnace under high purity argon atmosphere with a non-consumable tungsten electrode and a water cooled hearth. The alloy buttons sealed in steel jackets were hot rolled at 1223 K to break the as-cast structure and reduce the alloy button thickness (~50% thickness reduction). For investigating the effect of fluoride melt on the surface film characteristics, commercially available Alloy 690, Alloy 693 both of which were in mill annealed condition and the solution annealed (SA) Ni-Mo-Cr alloy specimens cut into rectangular pieces of dimensions 1 cm x 1 cm x 1 mm were used. In addition, commercially available Hastelloy N specimens cut into dimensions of 1 cm x 1 cm x 1 mm were used to study the microstructural evolution during exposure to the simulated service conditions of fission product Te. The nominal compositions of the alloys used in present study are given in Table 2.1.

Table 2.1: Nominal composition of the alloys used in present study.

Alloy	**Elemental Composition (wt.%)**							
	Ni	**Mo**	**Cr**	**Fe**	**Mn**	**Al**	**Si**	**others**
Ni_4Mo	Balance	29.5	-	-	-	-	-	-
Ni-Mo-Cr	Balance	16	7	-	-	-	-	-
Hastelloy N	Balance	15	7.2	3.7	0.53	248ppm	-	Ti:287 ppm
Alloy 690	Balance	-	31.0	11.0	0.5	0.5	0.5	C<0.05
Alloy 693	Balance	-	29.3	3.96	0.09	3.19	0.04	Nb:1.86,Ti: 0.42

2.1.2 Heat treatments and hardness measurement

The rolled Ni_4Mo and Ni-Mo-Cr alloys were sealed in quartz capsules filled with helium gas at 160 mm Hg pressure and solution annealed at 1223 K for 2 h and 1450 K for 1 h, respectively, followed by water quenching. The annealing treatments were chosen so that both the alloys in as-quenched condition remain in γ-phase [13, 29]. Compositional homogeneity of the as-quenched Ni_4Mo, Ni-Mo-Cr alloy, Alloy 690, Alloy 693 and Hastelloy N was analyzed using X-ray fluorescence (XRF) spectroscopy and are found to be in agreement with the nominal composition of the alloy.

Both the Ni_4Mo and Ni-Mo-Cr alloy after solution annealing (SA) were given ageing heat treatments at temperatures 873-1073 K for different time durations in the range 15 min-50 h and water quenched (WQ) to observe the development of ordered phases. To remove the non-uniformity of the alloy surface, the alloys were mechanically ground and polished upto mirror finish using the standard metallographic procedures optimized for Ni-based alloys.

Microhardness measurements on the as-quenched and aged samples were made with a Vicker's microhardness tester by applying a constant load of 300 gf for a dwell time of 15 s. A total of 10 measurements at different locations on the polished alloy specimens were recorded and the average value was calculated.

2.1.3 Microstructural characterization by transmission electron microscopy

JEOL 2000FX transmission electron microscope (TEM) equipped with tungsten (W) filament and charge coupled device (CCD) camera operated at 160 kV was used for the electron microscopic investigations. Thin foil TEM specimens were prepared by punching 3 mm disks from the alloy coupons grounded to 0.1 μm thickness and then jet thinned in a dual jet Tenupol electropolishing unit using 90% ethanol (C_2H_5OH) and 10% perchloric acid ($HClO_4$) electrolytic solution at 233K/25 V. Bright field (BF) and dark field (DF) imaging was carried out to study the ordered phase growth with heat treatments and the SAED patterns along different zone axes were recorded to study the development of superlattice reflections and different variants of the ordered phases.

2.1.4 Extended X-ray Absorption Fine structure (EXAFS) study

The atomic arrangements in Ni_4Mo and Ni-Mo-Cr alloys in their SRO and LRO states were investigated by EXAFS technique which measures and analyzes the fine structure oscillations observed in the range 50 -700 eV above the absorption edge of the chosen element. The Energy Scanning EXAFS beamline (BL-9) facility at INDUS-2 Synchrotron Radiation Source (2.5 GeV, 100 mA) at the Raja Ramanna Centre for Advanced Technology (RRCAT), Indore, India was utilized in fluorescence mode within photon energy range 4-25 keV to carry out measurements [76-77]. The beamline optics comprises of a Rh/Pt coated pre-mirror with meridional cylindrical curvature for higher harmonics rejection and vertical focussing, a Si (111) (2d =6.2709 Å) based double crystal monochromator (DCM) having a resolution of 10^4 at 10 keV and a bendable post mirror placed upside down for vertical collimation. The first crystal of DCM has indirect water-cooled arrangement for cooling and temperature remains stable within ± 0.1°C while the second crystal has a cylindrical crystal bent sagittally used for horizontal focusing (Fig. 2.1).

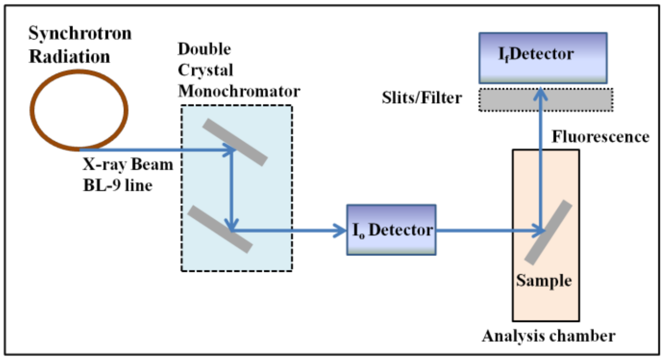

Fig. 2.1: **Schematic of EXAFS facility operated in fluorescence mode.**

For recording measurements in fluorescence mode, the sample and Si-drift detector were placed at 45° and 90° angle, respectively, to the incident beam. A ionization chamber detector placed prior to the sample stage measures the X-ray flux of the incident beam (I_0) and the absorbance of the sample (μ) determined by the relation $\mu = \frac{I_f}{I_o}$ as a function of energy (50 – 700 eV) is obtained by scanning the Si-DCM. Three spectra were recorded for each absorption edge with 10 s integration time for each scan and then averaged. The self-absorption corrections for finite thickness of the specimen are checked using the Booth algorithm provided in the ATHENA fitting software and were found to be insignificant [76-78].

For background removal, the EXAFS data $\mu(E)$ was converted to EXAFS function $\chi(E)$ by defining it as

$$\chi\,(E) = \frac{\mu(E) - \mu_o(E)}{\Delta\mu_o(E)} \qquad 2.1$$

where $\mu_0(E)$ is the background due to bare atom. $\chi(E)$ is normalized and transformed to EXAFS oscillations $\chi(k)$ as a function of wavenumber $\boldsymbol{k}$ using the standard relation between wave vector $\boldsymbol{k}$ and energy E [78-80]. The EXAFS oscillations, $\chi(k)$ is weighted by k^2 to amplify the oscillation at high $\boldsymbol{k}$ and the functions $\chi(k)*k^2$are Fourier transformed using k range of 2-10 Å^{-1} to generate the $\chi(r)$ versus r (or FT-EXAFS) spectra. The data analysis program ATHENA and ARTEMIS available within the IFEFFIT software package has been used for data processing and data fitting of the experimental EXAFS data [81-82]. Fitting program ARTEMIS generates theoretical paths based on suitable input crystalline structure models which are then fitted against the experimental $\chi(r)$ *versus* r curve in suitable $\boldsymbol{k}$ range (0.5-3.5 Å^{-1}). From the fitting results, the average bond lengths (r) corresponding to first coordination shell, co-ordination numbers (N) and disorder (Debye-Waller) factors (σ^2), which give the bond length fluctuations are evaluated. The number of free variables during each fitting cycle were kept below a maximum value dictated by Nyquist theorem ($N_{free} = \frac{2*\Delta k*\Delta r}{\pi}$) [81-82]. The goodness of fit, R obtained was in the range 0.001-0.009.

2.2 Interaction of Ni-Mo-Cr alloy with molten fluoride salt

2.2.1 Salt preparation and experimental design

Analytical grade LiF, NaF and KF salts taken in eutectic composition (46.5-11.5-42 mol.%; FLiNaK salt) were mixed thoroughly and vacuum dried at 393 K for 8 h following the procedure mentioned by Ouyang *et al.* [69] to reduce the residual moisture. At 973 K the solubility of oxygen in FLiNaK salt is estimated to be ~ 3.2 wt.% [69]. The salt was immediately transferred into the vacuum de-gassed alumina crucible containing the alloy specimens. The crucible was then placed in a box type resistance furnace maintained at 973 K at ambient pressure, held for 3 h and furnace cooled (Fig. 2.2). The ambient atmosphere was chosen for present study to simulate the accidental ingress of oxygen in the salt and promote oxide film growth. A time period for only 3 h is chosen for the present study as the impurity driven corrosion (HF, oxide, other ions) is dominant during initial exposure [38, 69-70]. The exposed samples were cleaned with 1 mol/L solution of aluminium nitrate ($Al(NO_3)_3$), acetone (CH_3COCH_3) and de-ionised water for excess salt removal at surface [69-70].

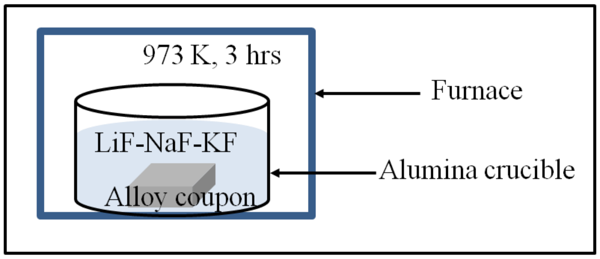

Fig. 2.2: **Schematic of experimental set up used for molten salt interaction study.**

2.2.2 X-ray diffraction

For phase identification, room temperature X-ray diffraction (XRD) measurements on the polished specimens were carried out in a Bruker's make D8 advance X-ray diffractometer in Bragg-Brentano geometry. The diffractometer uses a Ni-filtered Cu K_α radiation (λ =1.54 Å) as X-ray source operated at 40 kV/40 mA. The scans were recorded in the 2θ range 20^o-80^o at a scan speed of 1 deg/min. The peak positions were matched with the data available in JCPDS database to identify the phases.

2.2.3 Characterization by scanning electron microscopy

Carl Zeiss Auriga Cross Beam make field-emission scanning electron microscope (FESEM) was used for analyzing the morphology and microstructure of the exposed coupons surface as well as cross-sections. Secondary electron (SE) and backscattered electron (BSE) imaging modes were used to observe the surface morphology and the Z-contrast, respectively and quantitative elemental analyses were carried out using Energy dispersive spectroscopy (EDS).

2.2.4 X-ray Photoelectron Spectroscopy (XPS)

The XPS measurements were carried out using monochromatic Al Kα (hν =1486.74 eV) X-ray radiation at pass energy of 11 eV and base pressure of $< 1 \times 10^{-9}$ mbar. Survey scan in the binding energy (BE) range 0-1000 eV with step size = 0.1 eV to identify the surface elements was recorded in the fixed analyser transmission mode of the PHOIBOS HSA3500 DLD 150 R7 analyser using the SPECSLAB2 software. Subsequent high resolution energy spectra for major elements were recorded at a step size of 0.005-0.008 eV, dwell time of 0.1 ms/data point followed by necessary baseline subtraction, binding energy referencing with respect to C 1S peak occurring at 284.6 eV and flood gun corrections. Binding energy peaks were deconvoluted using Shirley background and fitted with Voigt peak profile [83] and the quantification was carried out using the CASA-XPS software.

2.3 Interaction of Ni-Mo-Cr alloy with simulated fission product tellurium

2.3.1 Design of experiment

Mechanically polished Hastelloy N specimens were electropolished in an electrolytic solution (90% CH_3OH+10% $HClO_4$) at 243 K operated at 20 V/20 s to remove the damaged surface layer formed during mechanical polishing. 10 mg/cm^2 Te was deposited on Hastelloy N surface by thermal evaporation technique. The Te concentration chosen corresponds to estimated Te that will accumulate on the MSR fuel salt container after 50 years of reactor operation. For thermal evaporation, Te flake (purity 99.9%) cleaned ultrasonically in acetone was taken in a Mo boat connected to a high voltage power supply and maintained at a vacuum of 5×10^{-5} mbar. The heat was generated in the Mo boat by adjusting the current which leads to the evaporation of Te flake that subsequently was deposited on the alloy surface (Fig. 2.3). All the Te coated specimens were subsequently sealed in evacuated quartz capsules, annealed at 973 K and 1073 K for 96 h and furnace cooled or WQ.

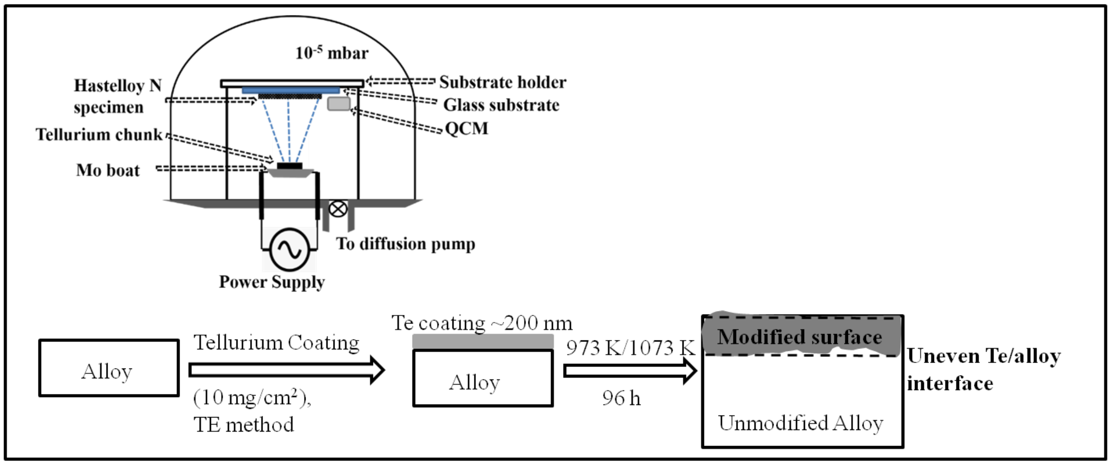

Fig. 2.3: Schematic of experimental set-up for Te interaction studies.

2.3.2 Microstructural characterization

The microstructure and nominal composition of the precipitates formed after interaction between alloy and Te were characterized using a 5-20 keV electron beam from a FESEM (Carl Zeiss Auriga Cross Beam®) equipped with EDS. Regions in the alloy cross-section suitable for TEM examination were identified under SEM observations and subsequently TEM lift outs were prepared by Auriga Carl Zeiss Focused Ion Beam (FIB) sectioning using 30 keV Ga^{2+} at milling current 150-600 pA [84]. The high angle annular dark field (HAADF) images, SAED patterns and point EDS analyses were carried out using 200 kV LIBRA 200 FE instrument having a CCD camera.

2.4 Theoretical basis for analysis of ordering transformations

The Helmholtz free energy (A) of any solid solution can be expressed in terms of the electronic, vibrational, magnetic, configurational degrees of freedom [14]

$$A = A_{el} + A_{vib} + A_{dis} + A_{mag} + A_{conf} \qquad 2.2$$

de Fontaine [52-53] showed that the configurational degree of freedom can be separated from the rest of the degrees of freedom and under certain solid-solid phase transformations such as the coherent order-disorder phase transformations, the change in the free energy is mainly governed by the change in configurational energy. In such cases the effect of change in the other degrees of freedom is neglected.

2.4.1 Configurational variables

A description of the configurational energy for the alloy was proposed by Sanchez *et al.* [14, 85] where the lattice of the alloy having n sites is represented by an Ising model (Fig. 2.4). The configuration of the alloy can then be described by a set of variables known as occupational variables {$\sigma_1, \sigma_2, \sigma_3,\ldots$} where each site 'i' is associated with an occupational variable σ_i. For a binary alloy $A_{1-x}B_x$, σ_i is defined as $\sigma_i = \begin{cases} 1 \text{ if the site is occupied by atom A} \\ -1 \text{ if the site is occupied by atom B} \end{cases}$

For n-site lattice, 2^n number of configurations are possible and the search for ground state energies in such cases becomes difficult and hence the cluster formulation was developed as a robust technique to achieve the same [85-88].

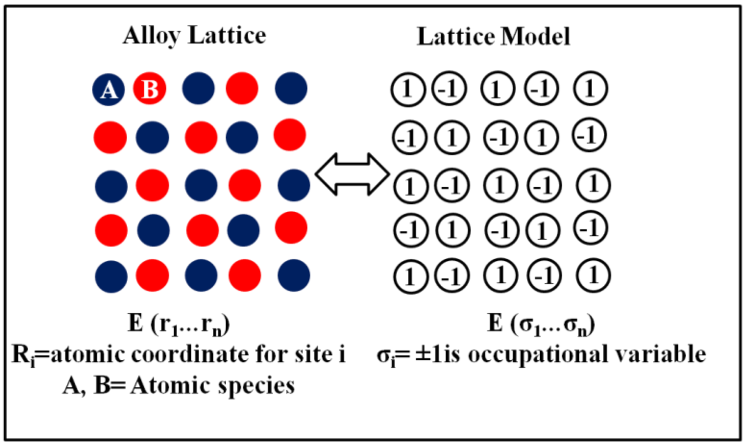

Fig. 2.4: Correspondence between alloy lattice and the lattice model/Ising model.

2.4.2 Cluster expansion formalism

As mentioned earlier, due to large number of possible configurations in N site lattice, it is advisable to use clusters in place of the point lattice [86-88]. The clusters are configurations of smaller units such as point cluster, pair cluster, triplet, etc. The energy Hamiltonian of the configuration σ is then expressed in terms of the generalized Ising Hamiltonian given by

$$E = J_0 + \sum_i J_i \sigma_i + \sum_i \sum_j J_{ij} \sigma_i \sigma_j + \sum_i \sum_j \sum_k J_{ijk} \sigma_i \sigma_j \sigma_k + \cdots \qquad 2.3$$

where 0, σ_i, $\sigma_i\sigma_j$, $\sigma_i\sigma_j\sigma_k$,… denote occupational variables of empty, point, pair and triplet clusters. The clusters which are symmetrically equivalent have same coefficient. All the terms with equal coefficients can be grouped together and the above equation can be re-written as

$$E(\boldsymbol{\sigma}) = \sum_\varphi D_\varphi J_\varphi \langle \prod_{i \in \varphi} \sigma_i \rangle \qquad 2.4$$

The coefficients J_φ are known as the effective cluster interaction (ECI) parameters and possess the symmetry property of the parent lattice [87-89]. These are defined as the interchange energy averaged over all atomic configurations and are concentration independent, but depend on the volume. D_φ is the cluster multiplicity and the correlation function $\langle \prod_{i\epsilon\varphi'} \sigma_i \rangle$ is the average taken over the symmetrically equivalent clusters of the product of spin or occupational variable over all the sites in the cluster φ' and is defined as

$$\langle \prod_{i\in\varphi} \sigma_i \rangle = 1/N \sum \sigma_i \sigma_j \sigma_k \ldots \qquad 2.5$$

When all clusters φ are considered in the sum, the cluster expansion is able to represent any function *E(**σ**)* of configuration ***σ*** by an appropriate selection of the values of J_φ. The cluster expansion converges rapidly and thus compact clusters (e.g., short-range pairs or small triplets) are sufficient for phase diagram calculations with desired accuracy.

2.4.3 Determination of ECIs

The ECIs can be either determined experimentally or by fitting the equations by energies of ordered intermetallics obtained by ab-initio density functional theory (DFT) calculations. Connolly *et al.* [90] proposed a structure inversion method (SIM) in which the ECI values were fitted to the energies of relatively small number of ordered binary alloys calculated via first principles method. The energy of any ordered intermetallic/ superstructure is written in terms of the cluster expansion (CE) Hamiltonian as

$$E(\Phi) = \sum_\gamma J_\gamma \xi_\gamma^\Phi \qquad 2.6$$

where $E(\Phi)$ is the energy calculated by first principles method and ξ_γ^Φ is the clusters chosen which forms a basis. ξ_γ^Φ is related to the configurational variables as $\xi_\gamma^\Phi = \langle \prod_{i\in\varphi} \sigma_i \rangle$, *i.e.*, the point correlation and pair correlation functions are, respectively, expressed as $\xi_i =< \sigma_i >$ and $\xi_{ij} =<$

$\sigma_i \sigma_j >$. The summation is considered only upto a maximum cluster $\Upsilon_{\max}$ beyond which the ECIs become negligible [14]

$$i.e., J_\gamma = \begin{cases} \text{finite} & \Phi \leq \Upsilon \leq \Upsilon_{\max} \\ 0 & \Upsilon_{\max} \leq \Upsilon \leq \infty \end{cases}$$

Writing the equation (2.6) in matrix form one can correlate the energy in terms of the ECIs with the cluster functions as the basis

$$\begin{bmatrix} E_{\Phi 1} \\ E_{\Phi 2} \\ \vdots \\ E_{\Phi \mathrm{n}} \end{bmatrix} = \begin{pmatrix} \xi_o^{\Phi 1} & \cdots & \xi_\gamma^{\Phi 1} \\ \xi_o^{\Phi 2} & & \xi_\gamma^{\Phi 2} \\ \vdots & \ddots & \vdots \\ \xi_o^{\Phi n} & \cdots & \xi_\gamma^{\Phi n} \end{pmatrix} \begin{bmatrix} J_o \\ J_1 \\ \vdots \\ J_n \end{bmatrix}$$

The energies are obtained from the DFT calculations of the selected ordered intermetallics. By formally inverting the equation we get the expression as

$$J_\gamma = \sum_\Phi \left(\xi_\gamma^\Phi\right)^{-1} E(\Phi) \qquad 2.7$$

The predictive power of the CE expansion and also the accuracy of the ECIs depends on the goodness of fit of the DFT energies and is expressed in terms of cross-validation score (CV) [91] defined as

$$(CV)^2 = \frac{1}{n} \sum_{i=1}^{n} (E_{DFT}^i - E_{CE}^i)^2 \qquad 2.8$$

Where E_{DFT}^i is the first principles calculated energy of the structure 'i' while E_{CE}^i is the CE predicted energy of the same structure obtained by least square fitting of the (n-1) structural energies.

The flowchart of the cluster expansion formalism [91] is presented in Fig. 2.5. In present study MAPS (MIT Ab-initio Phase Stability) code of Alloy Theoretic Automated Toolkit (ATAT) based on CE formalism [92] was used to generate clusters for Ni-Mo, Mo-Cr and Ni-Cr system. The details of input parameters are given in Table 2.2. Using Vienna Ab-initio Simulation Package (VASP), which will be discussed in section 2.4.4 [93], energy calculations were carried out for each known structure. The effective cluster interaction parameters (ECIs) as a function of cluster diameter were obtained from the VASP calculated energies by employing eqn. 2.7 and choosing a suitable cluster basis.

Table 2.2: Input parameters for ATAT calculations of Ni-Mo, Mo-Cr and Ni-Cr system.

Parameter	Description
Input crystal lattice	fcc
K-points per reciprocal space atom	2500
Potential used	PAW-PBE

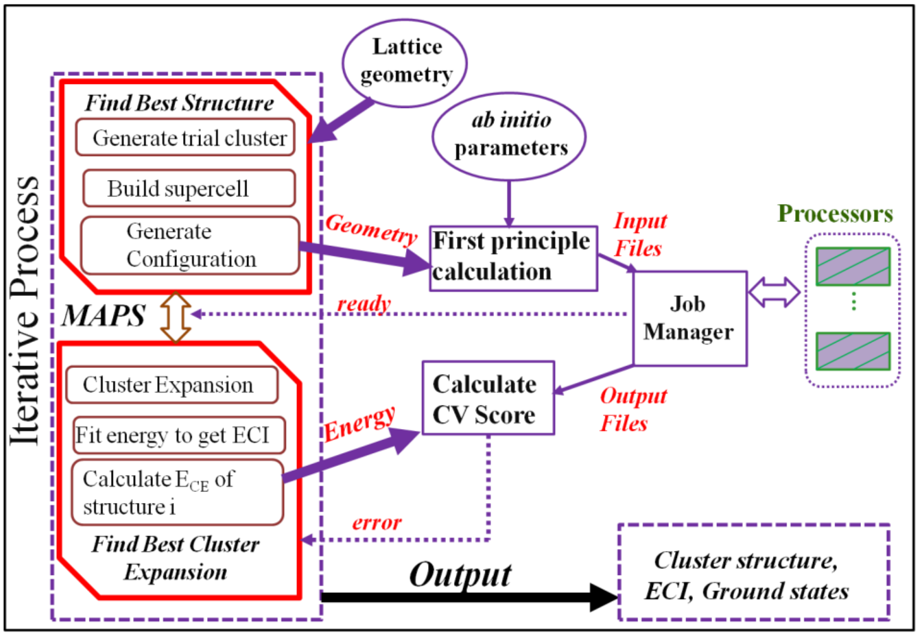

Fig. 2.5: Flowchart of cluster expansion formalism used in the present study [91].

2.4.4 First principles calculations of phase stability

The first principles calculations on Ni-Mo and Ni-Mo-Cr systems for ECI determination were performed using (VASP) [93]. The pseudopotentials used are projector-augmented wave (PAW) with the exchange-correlation potential as parameterized by Perdew-Burke-Ernzerhof (PBE) functional [94]. The Brillouin zone sampling was done by Monkhost-Pack scheme [95] using a high quality **k**-point mesh upto 12 x 12 x 12 grid. To observe the effect of Cr addition on $D1_a$ structure of Ni_4Mo, the VASP calculations were also carried out on Cr doped Ni_4Mo system with $D1_a$ structure with Cr substituting Mo site in a 2 x 2 x 2 supercell. The enthalpy of formation of the compound at zero temperature and zero pressure is obtained from the minimum total energy of the compound (expressed per atom) by subtracting the composition-weighted minimum total energies of pure elements in their standard state.

2.4.5 Evaluation of Warren Cowley parameters

The ordering reaction originates from the stronger attraction between unlike atoms as compared to like atoms. This preference for unlike atom in the first few neighbouring shells or the local ordering of atoms for any binary alloy $A_{1-x}B_x$ or ternary alloy $A_xB_yC_z$ can further be quantified using Warren Cowley parameters defined by following expressions [96]

$$\alpha_{ij}^{AB} = 1 - \frac{P_i^{AB}}{c_A} \tag{2.9}$$

where $P_i(AB)$ is the probability of finding an A atom in the neighbourhood of B in the ith shell when B is present at jth site. c_A and c_B are the atomic fractions. Similarly, in case of ternary alloy, these parameters are defined for different atomic pairs at lth shell where the atomic species are occupying ith and jth site, and expressed as [97]

$$\alpha^{AB}(\boldsymbol{l}) = \frac{P^{AB} - c_b}{\delta^{AB} - c_b} \tag{2.10}$$

Where δ^{AB} is the Kronecker delta having a value of 1 when A=B and zero otherwise. The Warren Cowley parameters, $\alpha(\boldsymbol{l})$ (where $\boldsymbol{l}$ denotes the coordination shell considered and the atomic species A resides at ith site and B is located at jth site, *i.e.*, $\alpha_{ij} \equiv \alpha(\boldsymbol{l}) \equiv \alpha^{AB}$ for A-B pair) for ordered Ni_4Mo phase with $D1_a$ structure at 300 K were calculated from the correlation functions using the following expression [92]

$$\alpha_{i-j} = \frac{\xi_{ij} - (2c-1)^2}{1-(2c-1)^2} \tag{2.11}$$

where *c* being the concentration of Mo and $\xi_{ij} = 1/N \sum \sigma_i \sigma_j$ is the pair correlation obtained from CE method. The sign of $\alpha(\boldsymbol{l})$ determines whether the atoms prefer to order ($\alpha<0$) or cluster (>0). The temperature dependence of $\alpha_{\text{i-j}}$, where i-j stands for the distance between the lattice positions *i* and *j* [87] is determined from the point (σ_i) and pair ($\sigma_i\sigma_j$) configurational variables as [87]

$$\alpha_{i-j} = \frac{<\sigma_i\sigma_j>-<\sigma_{i}><\sigma_j>}{1-<\sigma_{i}><\sigma_j>} \qquad 2.12$$

Similarly, for ternary system, the Warren Cowley parameters is expressed in terms of the correlation functions as [87]

$$\alpha_{i-j}^{AB} = \frac{<\sigma_i\sigma_j^2>+<\sigma_i^2\sigma_j>+<\sigma_i^2\sigma_j^2>-4c_A(1-c_B)}{4c_Ac_B} \qquad 2.13$$

$$\alpha_{i-j}^{AC} = \frac{-<\sigma_i^2\sigma_j^2>+<\sigma_i\sigma_j>+4c_Ac_C}{4c_Ac_C} \qquad 2.14$$

$$\alpha_{i-j}^{AB} = \frac{-<\sigma_i^2\sigma_j>-<\sigma_i\sigma_j^2>+2<\sigma_i^2\sigma_j^2>-4c_C(1-c_B)}{4c_Bc_C} \qquad 2.15$$

2.4.6 Modelling of disordered fcc structure using Special Quasi-random Structure algorithm

The disordered or random configuration of any alloy $A_{1-x}B_x$ is characterized by multisite correlation functions defined as

$$\xi_y^m = (2c-1)^y \qquad 2.16$$

where *y*, *m*, respectively, denote the number of atoms considered in cluster and separation distance e.g., *y* =2 corresponds to pair of atoms whose vertices separated by an *m^th^* neighbour distance and *c* is the solute concentration. The most convenient toolkit for generation of disordered configuration is the use of Special Quasirandom Structure (SQS) approach [98-99] where special periodic structure with a small unit cell is built whose correlation functions for the first few nearest-neighbour shells are as close as those of a target random alloy. The Monte Carlo Special

Quasirandom Structure (*mcsqs*) module and the Correlation Dumper (*corrdump*) module in ATAT has been used for generating SQS.

2.4.7 Determination of Gibbs free energy as a function of temperature

Once the ECIs are known, then standard statistical mechanics approach of semi grand canonical ensemble Monte Carlo method (MC) can be applied to study the thermodynamic properties of the material. In this approach, the solute concentration (c_i) and total energy of the ensemble (G) is allowed to change under an externally specified temperature (T) and chemical potential (ω) keeping the total number of atoms (M) fixed [92,100]. The energy is calculated using the expression

$$\Phi = G - \Delta\omega_c = U - TS - \Delta\omega_c \qquad 2.17$$

Where Φ is the Grand thermodynamic potential, U is the internal energy, S is the entropy and $\Delta\omega = \omega_{Ni} - \omega_{Mo}$. The Φ is obtained from the partition function (Z) which in turn is evaluated from the Metropolis algorithm incorporated in the MC approach. The equation used for the evaluation of Z and Φ is

$$\Phi = \frac{-\ln Z}{MK_BT} = \frac{-1}{MK_BT}\ln\left(\sum_i \exp(-MK_BT(E_i - \mu c_i))\right) \qquad 2.18$$

where E_i is the formation energy of any configuration obtained using the ECI values obtained from CE approach, K_B is the Boltzmann constant (8.617×10^{-5} eV K^{-1}).

Modelling of the order-disorder phase transformations in Ni_4Mo, is carried out by the Easy Monte Carlo Code (EMC2) module of ATAT. MC simulations were performed on supercell made by 25 x 25 x 25 expansion of the unit cell in the temperature range 400-1200 K while specifying chemical potential. The change in configuration was achieved by changing the Mo and Ni occupied sites and accepting the flip on the basis of Metropolis algorithm. Detailed algorithm of EMC2 is provided in [100-101].

Chapter 3 : New Insights to ordering in Ni_4Mo alloy

3.1 Background

Ni-Mo alloys (8-33 at.% Mo) without and with ternary additions of elements like Al, Cr, Ta, W exhibit a sequence of ordering transformations when quenched from high temperature and/or aged for longer times as discussed in section 1.5.1. These transitions are mainly dictated by the interaction energies between the near neighbours of different atomic species and the configurational entropy of the ordered arrangements. Thus, these pair and multisite interaction parameters give an insight to the complex ordering processes. In present study, the evolution of $D1_a$ structure of Ni_4Mo from the fcc matrix of the same composition is studied in-depth using the transmission electron microscopy and EXAFS. Furthermore, Cluster expansion methodology is adopted to concisely determine the configuration dependent alloy Hamiltonian. The EXAFS and CE results are correlated to quantify the structural order in Ni_4Mo alloy. The composition of the alloy studied is presented in Table 3.1.

Table 3.1: Composition of the alloy studied.

Alloy	**Theoretical composition (wt.%)**		**Experimentally determined composition (wt.%)**			
			EDS		**XRF**	
	Ni	Mo	Ni	Mo	Ni	Mo
Ni_4Mo	70.5	29.5	70.8(±0.1)	29.2(±0.1)	70.4(±0.1)	28.7 (±0.1)

3.2 TEM investigations on Evolution of the Long Range Order (LRO)

3.2.1 The As-Quenched alloy

The SAED patterns recorded along the [001] zone axis for the Ni_4Mo alloy in the as-quenched condition (SA at 1223 K for 2 h and WQ) as well as in the aged (at 873 K for 2 h) (Fig. 3.1 (a)-(b)) showed presence of diffused intensity maxima at $\{1\ \frac{1}{2}\ 0\}_{fcc}$ positions in addition to the fundamental fcc reflections. The complete absence of the $(210)_{fcc}$ reflections is also consistent with the observations, made earlier [14, 20] revealing the presence of expected short range ordering (SRO) The bright field images show a homogeneous microstructure marked only by the presence of twins (Fig. 3.1 (c)-(d)). The state of order in the as quenched condition is referred as “Short Range Order” (SRO) and is described in terms of

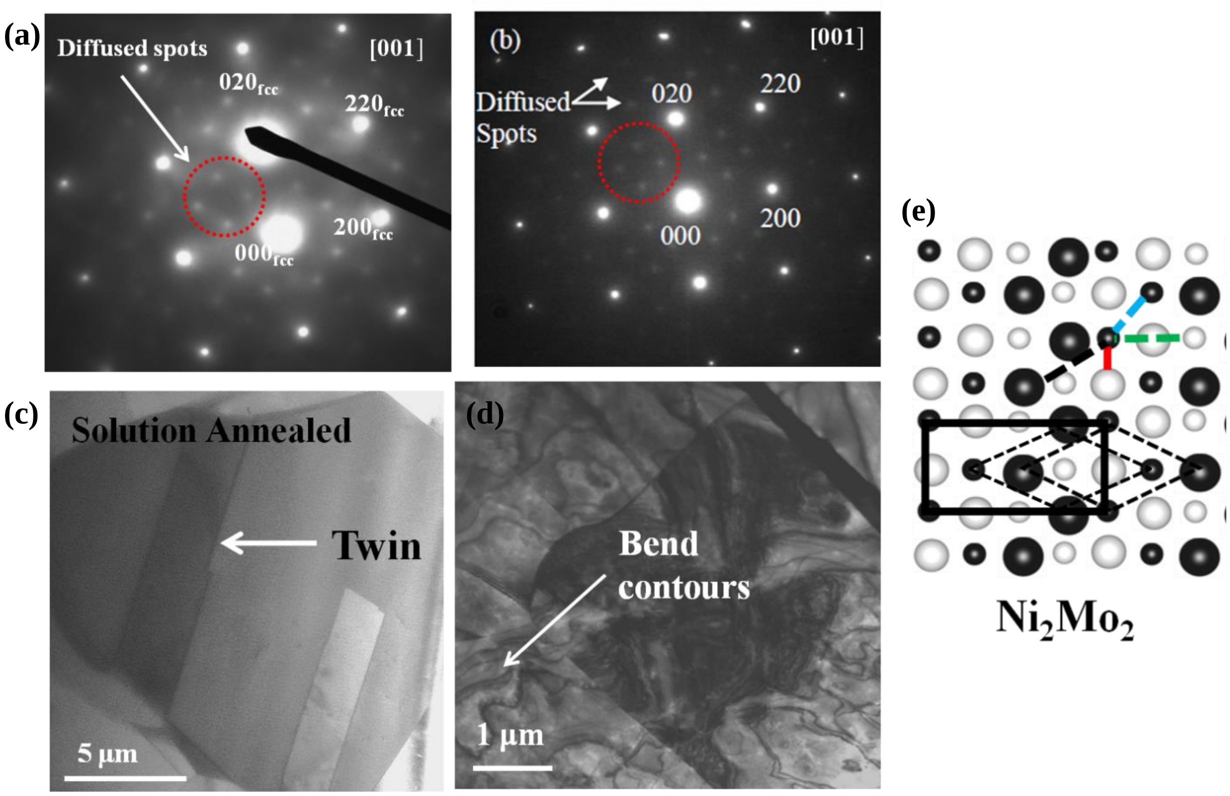

Fig. 3.1: Bright field images (a)-(b) and diffraction pattern recorded along [001] zone axis (b)-(d), for as quenched Ni_4Mo and Ni_4Mo aged at 873 K for 2 h +WQ, (e) N_2M_2 type stacking in the fcc matrix. The dotted lines show the Mo tile while the solid line shows the unit cell.

i) static short wave length concentration wave or wave packets with $\langle 1\ \frac{1}{2}\ 0\rangle_{\gamma}$ wave vectors, **k**, ii) sub unit cell clusters made up of motifs or tiles of competing superlattice structures and iii) microdomains of multiple superlattice structures of sub-unit cells of type Pt_2Mo, $D1_a$, DO_{22} coherently distributed in the disordered fcc matrix, all of which are equivalent [14, 31, 32]. The structure having the stoichiometry of N_2M_2, as shown in Fig. 3.1 (e), can be produced by amplification of such concentration waves in the fcc structure and such a transition qualifies to be a candidate for a second order transition. Since a long range ordering resulting in the N_2M_2 structure has never been encountered in the quenched Ni-Mo alloys or in analogous systems, the $<1\ ½\ 0>_\gamma$ ordered state is generally referred to as a “Short Range Ordered” (SRO) state.

3.2.2 Alloy aged at 1073 K for 4 h as well as 50 h

The Ni_4Mo alloy, after ageing at 973 K for 4 h showed weak spots at $\frac{1}{5}\{4\ 2\ 0\}$ positions and complete disappearance of $\{1\ ½\ 0\}_{fcc}$ spots in the SAED pattern indicating an early stage of the formation of ordered domains with $D1_a$ structure (Fig. 3.2 (a)). However, these domains could not be observed in the bright field images (Fig. 3.2 (b)) as well as in in the dark field images using $\{1\ ½\ 0\}_{fcc}$ spots due to their small size and volume fraction. The intensity of these superlattice reflections in the SAED patterns increased significantly for the Ni_4Mo alloy aged at 1073 K for 4 h (Fig. 3.2(c)). The increase in the intensity of the superlattice spots is mainly attributable to the increase in the volume fraction and size of ordered domains (Fig. 3.2 (d)-(f)) when the ageing time is increased from 4 h to 50 h. The dark field images also confirm the presence of ordered domains and increase in their number density and area fraction with increase in the ageing temperature and time.

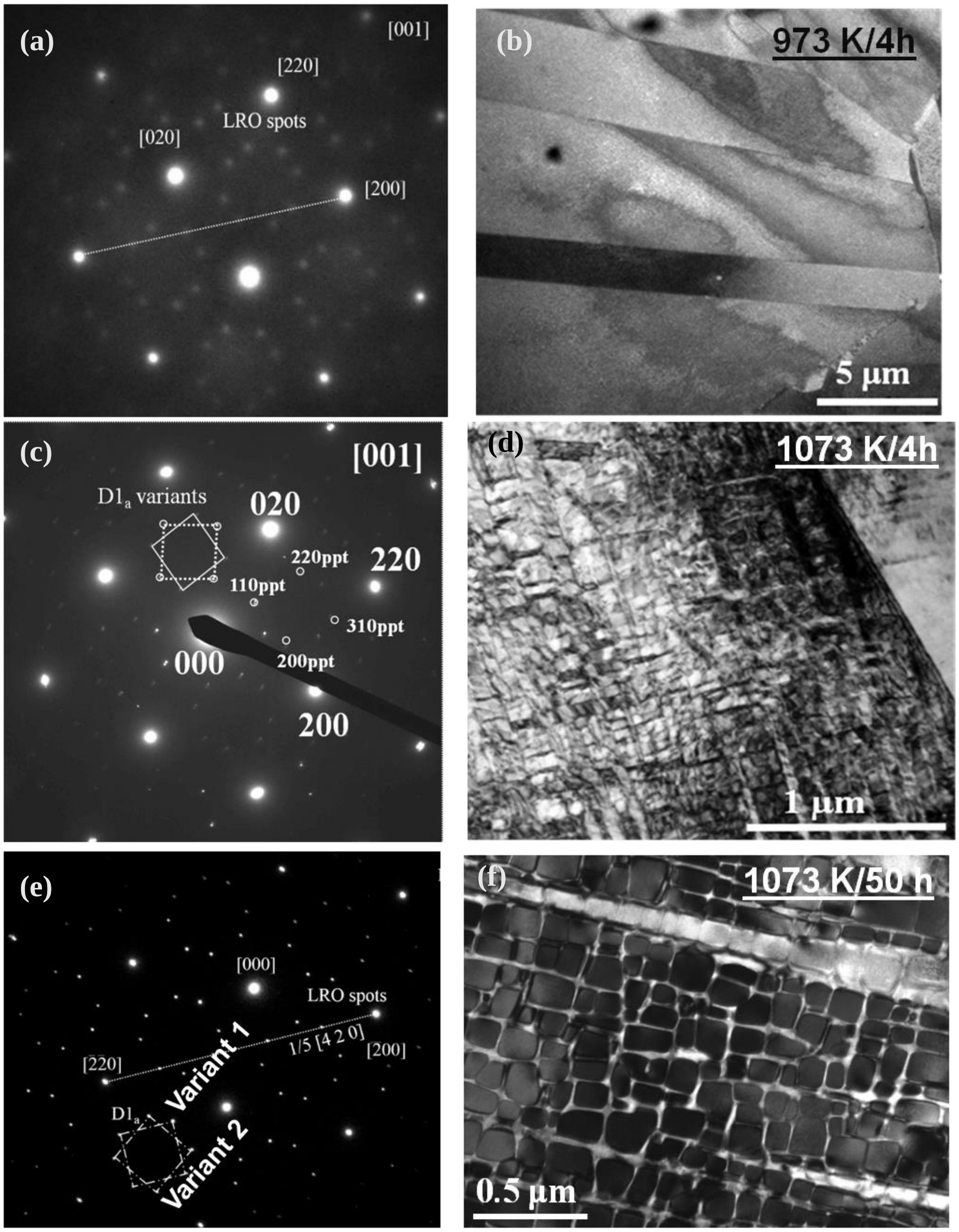

Fig. 3.2: Diffraction pattern recorded along [001] zone axis, bright field image for Ni_4Mo aged at (a)-(b) 973 K for 2 h +WQ, (c)-(d) 1073 K for 4 h+WQ and (e)-(f) 1073 K for 50 h+WQ.

There are six different variants of $D1_a$ ordered domains possible which orient among themselves either in antiparallel (c-axes in antiparallel orientation in adjacent domains) or in perpendicular (c-axes perpendicular to each other) twin configurations. Fig. 3.3 (a and b) show complementary dark field images of two variants of D1_a with c axis antiparallel to each other for the alloy aged at 1073 K for 50 h. The BF image in Fig. 3.3 (c) shows a pair of perpendicular twins and anti-parallel domains within them. By DF imaging using selected super lattice reflections different variants of ordered domains could be imaged in bright contrast (Fig. 3 a and b) and their relative orientations with respect to the parent disordered fcc structure could be established (Fig. 3d). After 50 h ageing at 1073 K, these domains were mostly seen to be continuous with no parent disordered phase in between (as is shown in Fig. 3 (a)-(b)). Many of these microdomains are cuboid shaped with domain boundaries along $\{100\}_{fcc}$, for anti-parallel twins, and $\{110\}_{fcc}$, for perpendicular twin boundaries, The domain size showed a large scatter, primarily because of their joining up in one direction. On an average each unit domain was found to be ~105 nm after 50 h of ageing at 1073K.

From the analyses of the SAED patterns, the orientation relationship between the fcc matrix and the D1_a structure is also obtained as $(420)_{fcc}$ // $(110)_{D1a}$; $[001]_{fcc}$ // $[001]_{D1a}$, as shown in Fig. 3.3 (d).

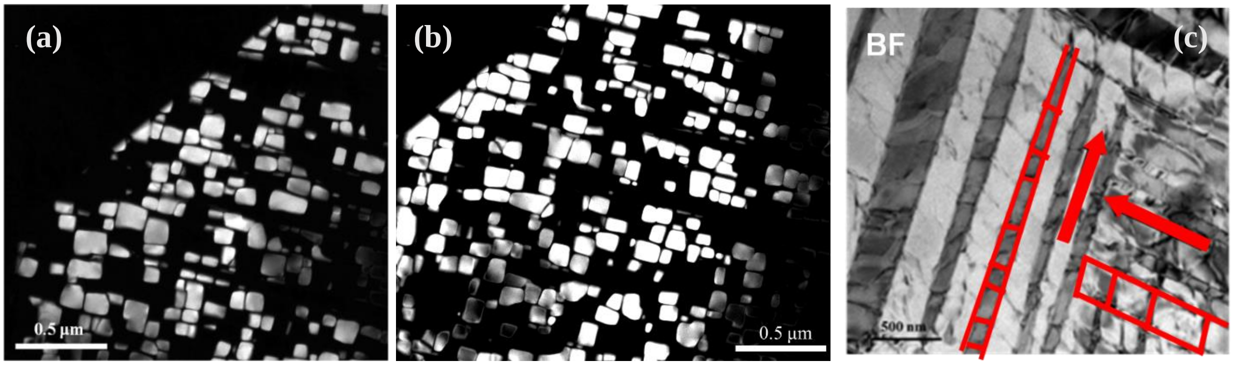

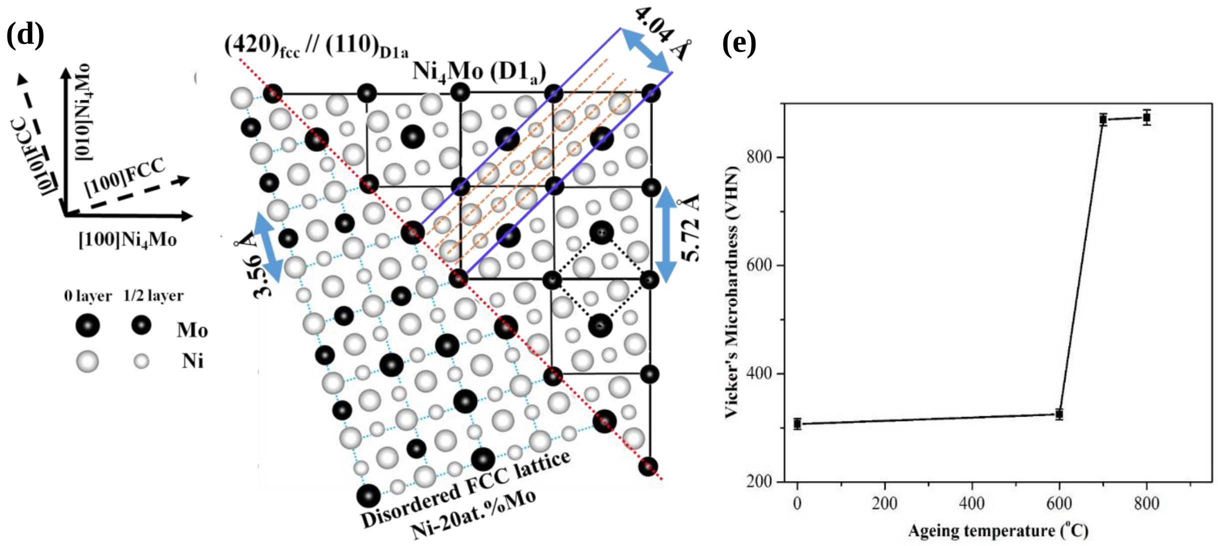

Fig. 3.3: (a)-(b) DF images taken along $\frac{1}{5}$[420] showing two variants of ordered domains with c-axis antiparallel to each other and (c) BF image showing domains with c-axis perpendicular to each other for alloy aged at 1073 K for 50 h. (d) Orientation relationship between fcc matrix and $D1_a$ phase. (e) Hardness variation of the alloy as a function of ageing temperatures for a constant ageing time of 2 h.

Furthermore, Vicker's microhardness was measured at different ageing temperatures to observe the effect of ordering on hardness of the alloy. The variation of microhardness with ageing is presented in Fig. 3.3(e). It is evident from the plot that the long range ordering of the alloy Ni_4Mo results in an increase in average micro hardness value from 307 (±10) Vickers hardness number (VHN) to 873 (±15) VHN. The increase in hardness is mainly attributed to a substantial increase in the bond strength due to ordering and the presence of coherent interface strains between adjacent domains [102-104]. The high resolution TEM images show a sharp interface indicating that the ordering transition at 1073 K is a first order transition (Fig. 3.4) and the ordered domains grow by the conventional nucleation and growth process.

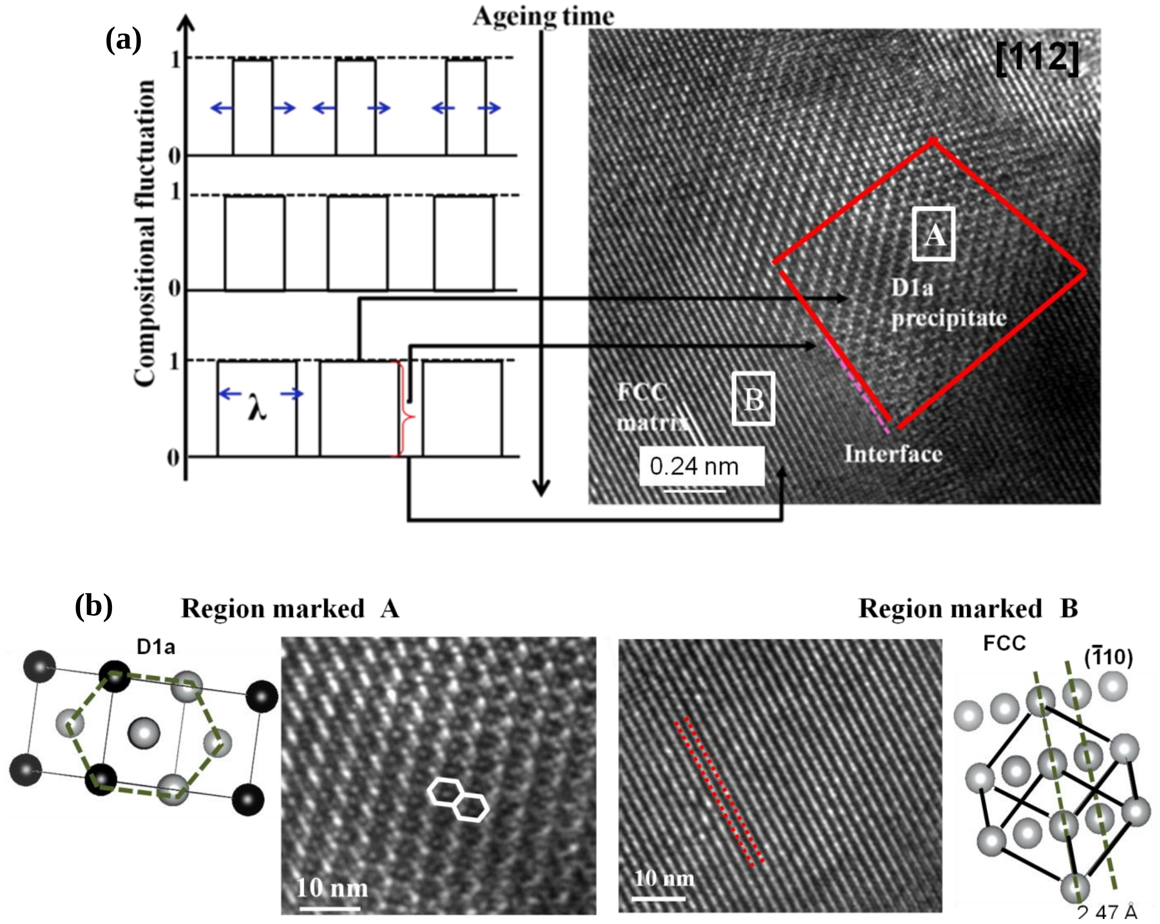

Fig. 3.4: (a) High resolution image of Ni_4Mo aged at 1073 K for 50 h recorded along [112] zone axis and the regions are correlated with the schematic showing the compositional fluctuations during nucleation and growth process. (b) Crystal projections of region marked as "A" and "B" in (a).

3.3 EXAFS study

The normalized absorption coefficient as a function of energy corresponding to Ni K_α and Mo K_α edges for both the as-quenched and the aged Ni-20 at.% Mo alloy (ageing treatment given at 1073 K for 4 h and WQ) is plotted in Fig. 3.5. The plots for the magnitude of EXAFS oscillations as function of radial distance for the as-quenched and the aged specimen corresponding to both Ni and Mo K edges are given in the insets of Fig. 3.5 (a) and (b), respectively. It is evident that there is an increase in amplitude of the peak near 2.2 Å in EXAFS oscillations ($\chi(r)$) in the Ni K_α absorption edge after ageing suggesting an increase in structural order on ageing. However, there is no change in the absorption edge of the as quenched and aged alloy wrt standard Ni foil indicating no change in oxidation state which is expected for an alloy system.

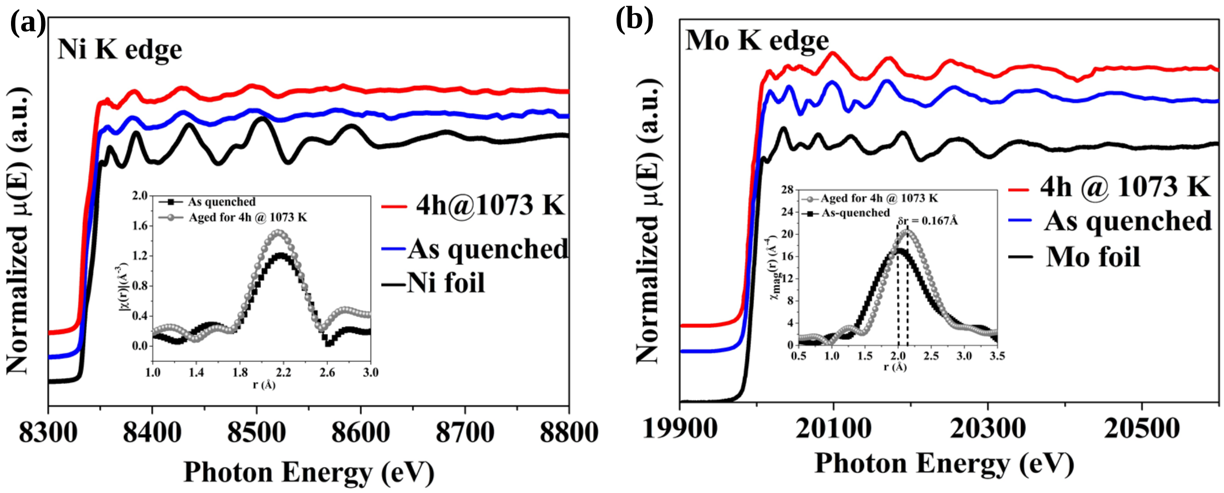

Fig. 3.5: Experimental normalized *μ(E) versus E* EXAFS plots for Ni-foil, Ni_4Mo as quenched and Ni_4Mo aged at 1073 K for 4 h corresponding to (a) Ni edge (b) Mo edge. The insets show the experimental |χ(r)| *versus* r plots for the same.

EXAFS data for as quenched and aged Ni_4Mo alloy was modelled by the disordered fcc configuration and $D1_a$ structure, respectively, using the Ni-Ni, Ni-Mo and Mo-Ni paths. The path corresponding to Mo-Mo bond was not included in the fitting as it leads to non-plausible fitted parameters. The experimental *μ(E) versus E* plots, *|χ(r)| versus r* curves along with their simulated best fit curves are plotted in Fig. 3.6. The fitting results are summarized in Table 3.2.

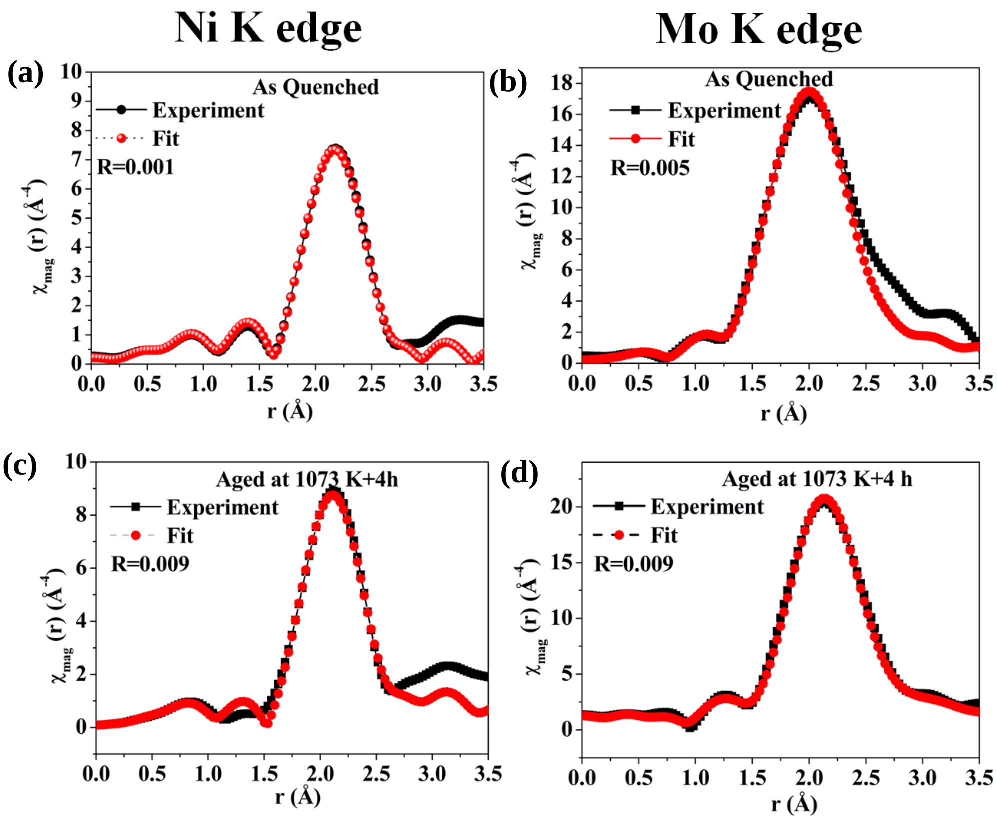

Fig. 3.6: Experimental |χ(r)| *versus* r plots along with their simulated fits for (a)-(c) Ni-edge, (b)-(d) Mo edge corresponding to as quenched Ni_4Mo alloy and alloy aged at 1073 K for 4 h and WQ, respectively.

Table 3.2: Results of EXAFS fitting for as quenched and aged (4h at 1073 K and water quenched (WQ)) Ni-20 at.% Mo alloys. The input crystal structures for EXAFS fitting are the fcc structures for as quenched alloy and $D1_a$ structure for the aged alloy. The values r, N and σ^2 correspond, respectively, to the bond distances, coordination number and Debye Waller factor which is a measure of the fluctuations in the bond lengths in the first coordination shell.

Bond	**Ni-20 at.% Mo as quenched (fcc structure)**			**Ni-20 at.% Mo aged at 1073 K/4 h ($D1_a$ structure)**		
	r (Å)	**N**	**σ^2(Å^2)**	**r (Å)**	**N**	**σ^2(Å^2)**
Ni-Ni	2.57±0.01	8.95±0.19	0.0149 ±0.0002	2.59±0.01	8.9±0.5	0.0119±0.0009
Ni-Mo	2.64±0.01	2.91±0.17	0.0098±0.0005	2.62±0.01	2.7±0.64	0.0025±0.0012
Mo-Ni	2.48±0.02	10.8±0. 7	0.0048±0.0009	2.52±0.03	9.9±0.9	0.0048±0.0011

In a completely disordered Ni-20 at.% Mo alloy the number of Mo atoms surrounding a Ni atom as its first near neighbour will be 2.4, which is a product of the average Mo-atom fraction and the co-ordination number. An increase in this number will indicate an ordering tendency (SRO /LRO). In as quenched alloy, Mo and Ni show preference for the unlike atoms as its first nearest neighbours since the number of Ni-Mo and Mo-Ni bonds is > 2.4. The mismatch in Ni-Mo and Mo-Ni bond lengths (Table 3.2) is also attributed to SRO induced local structure change around the Mo atoms which is also reflected in the decrease in the value of Debye-Waller factor for the Ni-Ni and Ni-Mo bonds for the aged sample consistent with the TEM observations showing ordering transition in the aged specimen.

3.4 Cluster expansion (CE) based calculations

The cluster expansion of Ni-Mo alloys was carried out upto 10 atoms/cell. Comparison of energy per atom for several stable and metastable phases across the composition range calculated using VASP calculations and back calculation using CE show that they are in good agreement. The root mean square error in the CE fit is very small (± 28 meV/atom) and distributed evenly over the whole range of calculations.

3.4.1 Ground state cohesive properties

The convex hull showing the energy as a function of Mo concentration is presented in Fig. 3.7. The configurations which lie along the line of convex hull are the mainly the ordered structures of Ni-Mo system, *viz.*, $L1_o$ type-NiMo, Pt_2Mo type -Ni_2Mo, $L1_2$ type -Ni_3Mo, $D1_a$ type -Ni_4Mo. All these ordered ground states have negative formation enthalpy suggesting that the phases are stable at 0 K. Amongst these, NiMo is the most stable structure in Ni-Mo system as compared to the other configurations since it has the lowest formation energy (-0.966 eV/atom). In addition to known ground state structures, the CE approach predicts energy of possible metastable states at different compositions at 0 K. The cohesive energies for selected ordered structures (Mo: 0-50 at.%) along with their lattice configurations projected along [001] is also shown (Fig. 3.5 (e)).

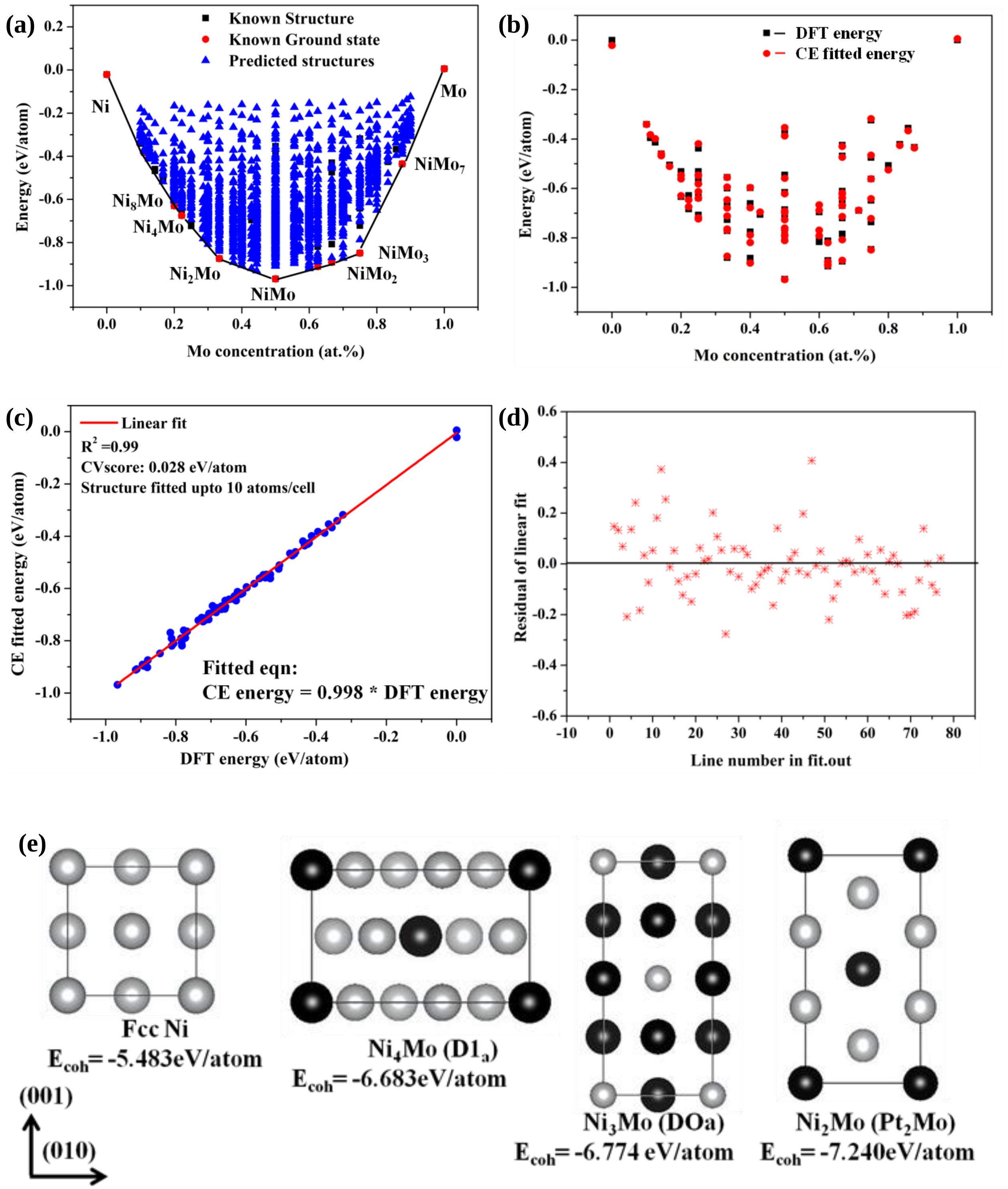

Fig. 3.7: Output of MAPS algorithm for Ni-Mo binary system showing (a) Calculated energies of different stable and metastable phases as a function of Mo concentration, (b) Energies calculated by VASP as well as by CE fitting plotted as a function of Mo concentration, (c) Actual energy (by VASP) *versus* energies calculated by CE model and (d) residual of fitting of VASP calculated energies with those obtained from CE (e) [001] projection of selected ordered structures along with their cohesive energies.

3.4.2 Nature of ECIs obtained

The clusters generated were pair, triplets and quadruplets. The pair clusters generated had a maximum diameter of 7.42 Å (upto 9th NN). Few selected clusters are presented in Fig. 3.8 (a) along with the cluster multiplicity (Fig. 3.8 (b)). The ECI values are diminished for multi-body (triplets and quadruplets) clusters as compared to pair clusters indicating a good convergence of CE model. Additionally, it was observed that for each type of cluster the magnitude of the ECI decreases with increase in cluster diameter which indicates that only the first few nearest neighbour interactions play a crucial role in the configurational energy of the alloy.

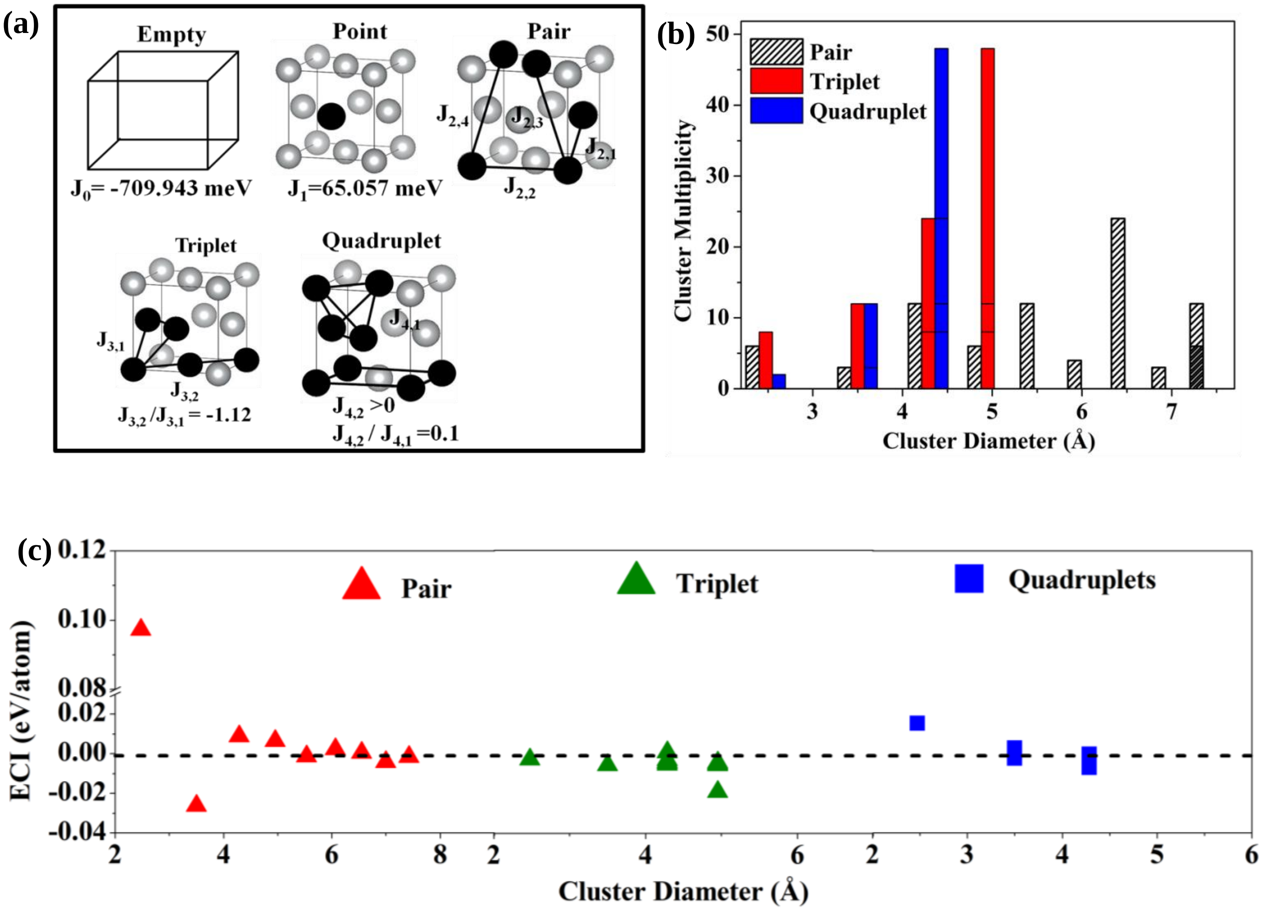

Fig. 3.8: (a) The truncated set of clusters generated for Ni-Mo system considering 10 atoms/cell (CV score=28 meV/atom). The $J_{i,j}$ are the ECIs where i denotes the type of cluster (0=empty, 1=point, 2 =pair and so on) while j denotes the jth nearest neighbour, (b) Cluster multiplicity, (c) ECIs for pair, triplet and quadruplet clusters as a function of cluster diameter.

The positive values of pair ECIs denote tendency for ordering while negative values suggest clustering [91-92, 105]. From the sign of the normalized ECIs, it is evident that Mo prefers Ni as its first and third nearest neighbour. The ECIs for smallest triplet is positive suggesting ordering. Kulkarni *et al.* [56, 59, 62] and Hata *et al.* [31-32, 58, 106] have calculated the pair interaction energies for calculating the stability of different Ni-Mo phases which are compared with the ECIs and are presented in Fig. 3.9. The variation in the values could be attributed to the fact that in other studies the multisite contributions are ignored while in present study both pair as well as multisite interactions are considered to describe the energetics of the system. The Tight-binding linear muffin-tin orbital (TB-LMTO) approach [14] calculates the composition dependent ECIs while the ECI obtained in the cluster expansion method is valid over the whole range of the Ni-Mo composition. The ECIs obtained using CE approach is volume dependent but is assumed to remain constant with respect to temperature.

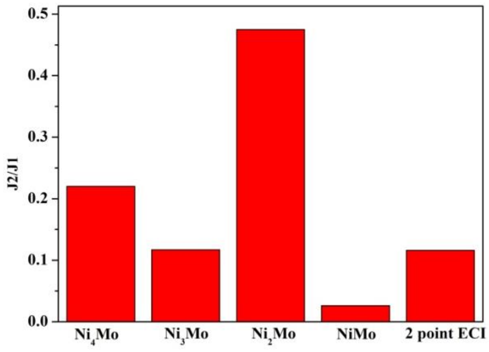

Fig. 3.9: Comparison of compositionally dependent and compositionally independent ECIs [102].

3.5 First principles calculations on disordered fcc

SQS algorithm was used to generate cells of disordered Ni$_4$Mo comprising 20, 25, 30 and 35 atoms/unit cell. Of these, the cell modelled using 25 atoms/unit cell resulted in the best pair and multisite correlation match with that of a perfectly random alloy. The SQS with 30 and 35 atoms/cell did not give best correlation match as the objective function, which is a measure of matching of correlation functions between those of an ideal disordered solid solution and the simulated one, could not be minimized. This indicates that the set of clusters considered for present case (upto 4th nearest neighbour) was sufficient to minimize the correlation functions for a cell with 25 atoms. To minimize the cell with 30 and 35 atoms, number and diameter of the clusters considered would have to be increased. However, doing so will only increase the computational time as the SQS with 25 atoms efficiently describes the disordered alloy and its energetics.

The structural data for 25 –atoms SQS fcc structure is given in Table 3.3. The maximum diameter considered for pair, triplet and quadruplet cluster are 5.1 Å, 5.1 Å and 3.6 Å, respectively. The optimized disordered fcc configuration for Ni_4Mo along with the $D1_a$ ordered structure is presented in Fig. 3.10.

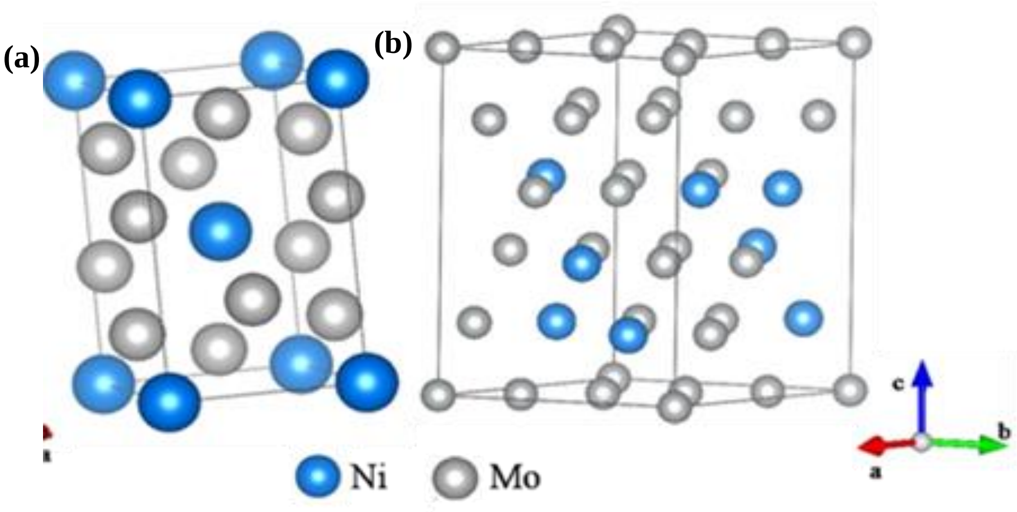

Fig. 3.10: Ordered and disordered configuration of Ni_4Mo.

Table 3.3: Correlation functions for the disordered configuration of fcc Ni_4Mo.

Cluster type n_α	Cluster Diameter (Å) l_α	Calculated Correlation (ρ)	Actual correlation (ρ_a)	Mismatch (ρ-ρ_a)
2	2.55	0.36	0.36	0
2	3.61	0.36	0.36	0
2	4.42	0.36	0.36	0
2	5.11	0.36	0.36	0
3	2.55	-0.24	-0.216	-0.024
3	3.61	-0.226	-0.216	-0.0106
3	4.42	-0.226	-0.216	-0.0106
3	4.42	-0.187	-0.216	0.029
3	4.42	-0.200	-0.216	0.016
3	5.11	-0.226	-0.216	-0.010667
3	5.11	-0.220	-0.216	-0.004
3	5.11	-0.200	-0.216	0.016
4	2.55	0.200	0.129	0.0704
4	3.61	0.17	0.129	0.043
4	3.61	0.146	0.129	0.017

The enthalpy of formation for the $D1_a$ as well as fcc configuration of Ni-Mo alloy was calculated from the equation

$$\Delta H(Ni_{0.8}Mo_{0.2}) = E\ (Ni_{0.8}Mo_{0.2}) - 0.8E(Ni) - 0.2E(Mo) \qquad 3.1$$

where $E(Ni)$ and $E\ (Mo)$ are the reference energies of the pure components in their respective ground states. The spin polarized calculations were performed only on ferromagnetic fcc Ni and not for bcc Mo as it is non-magnetic [14]. Using the values $E(Ni_{fcc})$=-5.51 eV/atom and $E\ (Mo_{bcc})$= -9.84 eV/atom, the enthalpy of formation of disordered phase was calculated to be -

0.289 eV/atom. The enthalpy of formation for $D1_a$ ordered phase was calculated to be -0.298 eV/atom which is in close agreement with the value reported by Arya *et al.* [14] and Zhou *et al.* [30]. The values are slightly overestimated as Mo_{bcc} structure was used to calculate energy in present case. The ordering energy is estimated to be $E= E_{ord}-E_{dis}$=-0.01 eV/atom also matches closely with the value of 0.012 eV/atom [14] as reported by Arya *et al.* For the disordered Ni_4Mo, Ni had both Mo and Ni as the nearest neighbour at a distance of 2.55 Å. Similarly, Mo also had both Ni and Mo as nearest neighbour situated at 2.55 Å which are matching closely with bond lengths obtained via the EXAFS analyses of the as-quenched alloy. The disordered fcc Ni_4Mo is different from the case of ordered Ni_4Mo structure where Mo does not have Mo as its nearest neighbour.

3.6 Monte Carlo simulations

Monte Carlo simulations were performed to evaluate Warren Cowley parameters α(i) as a function of temperature, for different neighbouring shells "i". For Ni_4Mo, the negative values of α(1), α(4), α(6) shell suggest Ni prefers Mo as its first, fourth and sixth NN (Fig. 3.11).

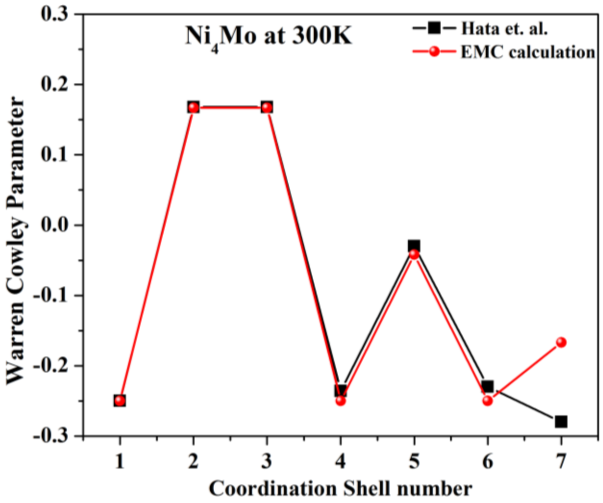

Fig. 3.11: Calculated Warren Cowley parameters corresponding to different coordination shells for $D1_a$ structure of Ni_4Mo alloy at 300 K. The calculated values are compared with those reported by Hata *et al.* [32].

These values match well with those reported by Hata *et.al.* [31-32]. Similarly, positive values of $\alpha(2)$, $\alpha(3)$ and $\alpha(5)$ suggest that Ni prefers Ni as its second, third and fifth nearest neighbour.

3.7 Discussion of results

The comparison between theoretically evaluated bond lengths and nearest neighbour configurations for the as-quenched alloy with the values obtained experimentally from EXAFS fit are presented in Table 3.4. It is evident that Ni-Ni, Ni-Mo and Mo-Ni bond lengths as well as the coordination numbers obtained experimentally and by first principles calculation on SQS model match reasonably well. The difference observed in Ni-Mo and Mo-Ni bond lengths could be attributed to SRO characteristics of the alloy which causes a local structural change around Mo and Ni atoms. No Mo-Mo bonds were observed indicating that Mo is surrounded by only Ni atoms in the first coordination shell.

The value of $P_i(BA)$ (formulae and symbols have been discussed in section 2.4.5) is calculated from EXAFS fit by calculating the number of A-B bonds [96,97]. From the number of bonds in EXAFS fit, the Warren Cowley parameter for the first coordination shell of as – quenched alloy was calculated to be -0.228 (±0.004). The value was found to be in close agreement with the reported value of -0.22 by Chakravarty *et. al* [107]. The negative value indicates the preference of Ni atoms for Mo atoms which is in accordance with the extensive reports available on Ni-Mo system [4-16, 36]. The rigorous EXAFS analysis clearly establishes the preference for unlike atom at first nearest neighbour position in the as-quenched alloy.

Table 3.4: Comparison of bond lengths for Ni-Ni and Ni-Mo as obtained from EXAFS fit, DFT-GGA calculations on the SQS structure, N_2M_2 structure (LRO as well as cluster in the fcc matrix) and the theoretical fcc structure corresponding to as-quenched Ni-20 at.% Mo alloy. The error in the estimation of number of unlike bonds is <0.2.

		Bond Lengths (Å)			
Bond type	**EXAFS fit**		**N_2M_2 cluster in fcc matrix**	**SQS (DFT-GGA)**	**Theoretical fcc**
	As quenched Alloy (fcc structure)	**As quenched alloy (fcc based Non-stoichiometric N_2M_2 LRO)**			
Ni-Ni	2.57±0.01	1.89	2.47	2.51±0.08	2.51
Ni-Mo	2.64±0.01	1.85	2.47	2.60 ±0.2	2.51
		Number of unlike bonds			
	2.9	8.6	2.6	2-3	3
		Warren Cowley Parameter (for 1st NN)			
		-0.249 (Present study) **-0.224 [Ref. 106]**			

Furthermore, fitting of EXAFS oscillations with theoretical paths generated from LRO N_2M_2 structure leads to non-plausible parameters (extremely low values of the bond lengths) indicating that the SRO is not a manifestation of LRO type N_2M_2 structure, but could be due to localized sub-unit cell sized N_2M_2 type stacking. The calculations performed on SQS model though do not provide information on the ordering tendency of the alloy, but provide a reasonably good estimate of the bond lengths and enthalpy of formation.

Similarly, EXAFS fit in case of alloy aged at 1073 K for 4 h and WQ is shown in the Table 3.5 along with the theoretical calculations. The LRO parameter for the alloy is calculated to be 0.85. The difference between the bond lengths calculated from first principles calculations on $D1_a$ structure and those evaluated from EXAFS fit is attributed to the presence of untransformed fcc matrix. In case of aged specimen also, Mo had only Ni as its first nearest neighbour. The preference for unlike atom at first nearest neighbour distance in both as-quenched and aged condition is due to the ordering tendencies in the alloy. These ordering tendencies are stabilized by the enthalpy which in turn depends on the ECI values. As discussed in sec. 3.3.2, the ECI value corresponding to first NN distance are positive for the Ni-Mo system which show the ordering tendency and corroborates well with the EXAFS and TEM study.

Table 3.5: Comparison of the number of bonds (Ni-Ni, Ni-Mo and Mo-Ni type), bond lengths obtained from EXAFS fit for Ni_4Mo alloy aged at 1073 K for 4 h and WQ with $D1_a$ structure and first principles calculations performed on SQS structure.

		Coordination number
Element /Bond	**EXAFS fit**	**VASP calculations**
Ni	11.6	12
Mo	10	12
		Bond lengths(Å)
Ni-Ni	2.59±0.01	2.47
Ni-Mo	2.62±0.01	2.47
Mo-Ni	2.52±0.03	

From the MC simulation, the estimated value of Gibbs free energy for the ordered Ni_4Mo ($D1_a$ structure) phase was found to change from -0.62 eV/at 300 K to - 0.39 eV/at 1000 K. At ~1000 K, the calculated Warren Cowley parameters for first seven coordination shells for Ni_4Mo approach values close to zero, which correspond to the disordered fcc phase with no preference for like or unlike atom indicating initiation of order ($D1_a$) to disordered (fcc) phase transition above ~1000 K (Fig. 3.12 (b)). Similarly, the LRO parameter (η) (Fig 3(c)) is found to change from -0.99 at 300 K to -0.72 at 1000 K, indicating the tendency of dis-ordering at temperature higher than 1000 K. On extrapolating the plot, the temperature at which is $\eta=0$ is found to be 1155 K. It is to be noted that the order-disorder transition in Ni_4Mo alloy occurs at 1140 K while the calculations show that the transition can occur at a lower temperature. This is owing to the fact that the vibration effects are neglected in the calculations.

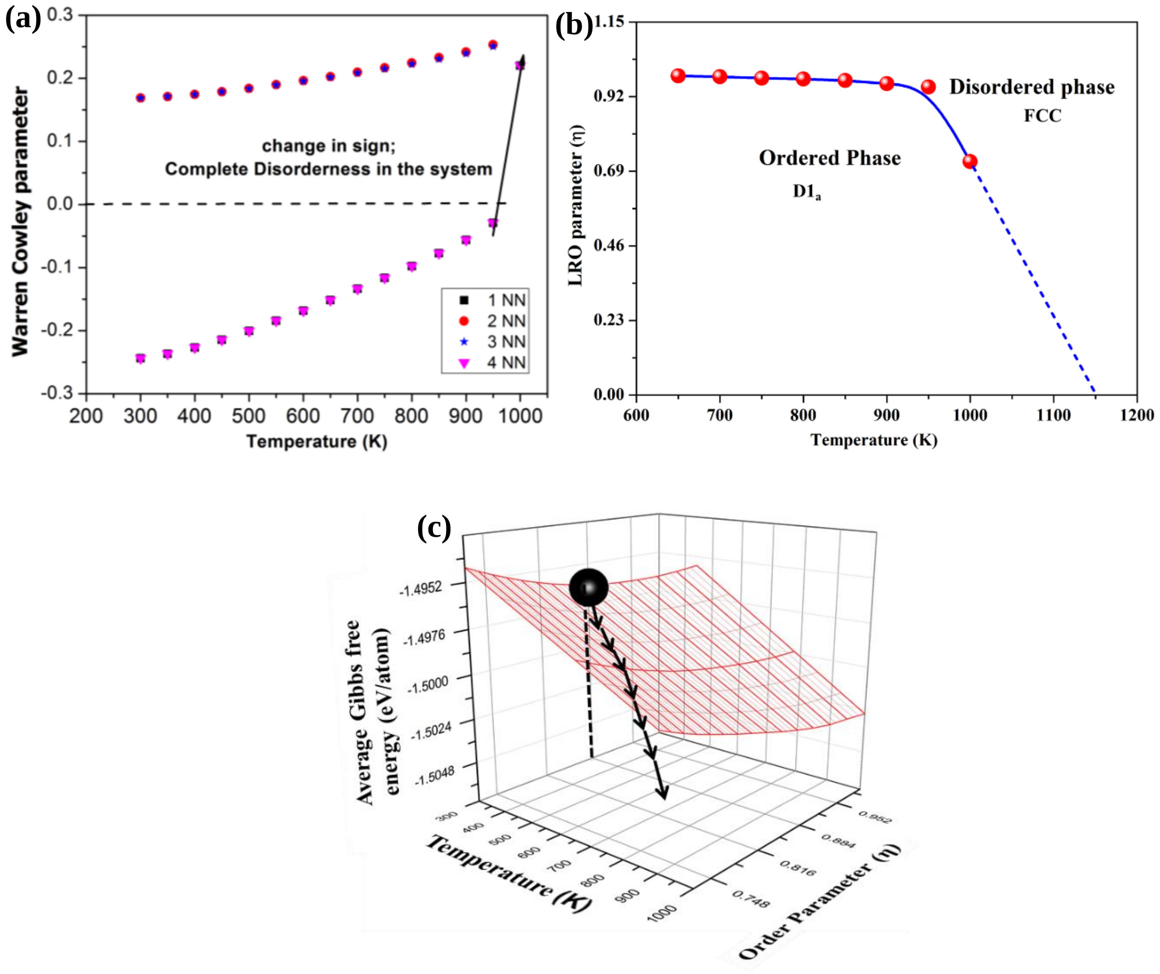

Fig. 3.12: Variation of (a) Warren Cowley parameters for the first four coordination shells with temperature and (b) LRO parameter of ordered Ni_4Mo with temperature. (c) Plot showing Gibbs free energy of ordered Ni_4Mo as function of temperature and order parameter.

3.8 Summary

On the basis of present work following conclusions can be made:

(i) In the SRO structure of the alloy, the local environment around the Ni and Mo atoms are different as indicated by unequal values of Ni-Mo and Mo-Ni bond lengths. Moreover, Mo has all Ni atoms as its first nearest neighbour, but no Mo atoms.

(ii) The LRO structure of the alloy is described by the $D1_a$ phase which grows coherently with the fcc matrix. The NN configuration around Mo atom shows that it has all Ni atoms at the first nearest neighbour distance, but no Mo atoms. Also, the bond lengths obtained experimentally were in close agreement with the theoretically evaluated bond lengths.

(iii) The CE approach was used to evaluate the ECIs as a function of nearest neighbour distances. The positive values of ECI indicate the preference for unlike atoms at first NN distance and hence facilitates the formation of ordered precipitates (both SRO and LRO).

(iv) Warren Cowley parameters for both as quenched and aged alloy were evaluated from CE method and found to be in concordance with the experimentally observed values. The CE approach was further used to evaluate the change in free energies as a function of temperature (T) and order parameter (η) for Ni_4Mo system.

Chapter 4 : Ordering in Ni-Mo-Cr Alloy

4.1 Background

Ni-16 wt.% Mo-7 wt.% Cr (Mo+Cr =20 at.%) based alloys, *viz.*, Hastelloy N, GH3535 alloy are solid solution strengthened single phase alloys which are being considered as potential candidates for use in MSR as structural materials [2, 17]. The selection of these alloys has been with the expectation that a prolonged use of these alloys in the service condition in the medium to high temperature regime will not lead to formation of coherent ordered precipitates. In order to confirm this conjecture, it is important to investigate the ordering characteristics in Ni- 16 wt.% Mo- 7 wt.% Cr alloy for evaluating its performance at high temperatures for prolonged time as well as for gaining an understanding of the role of Cr in influencing the ordering characteristics of this ternary system (Fig. 4.1).

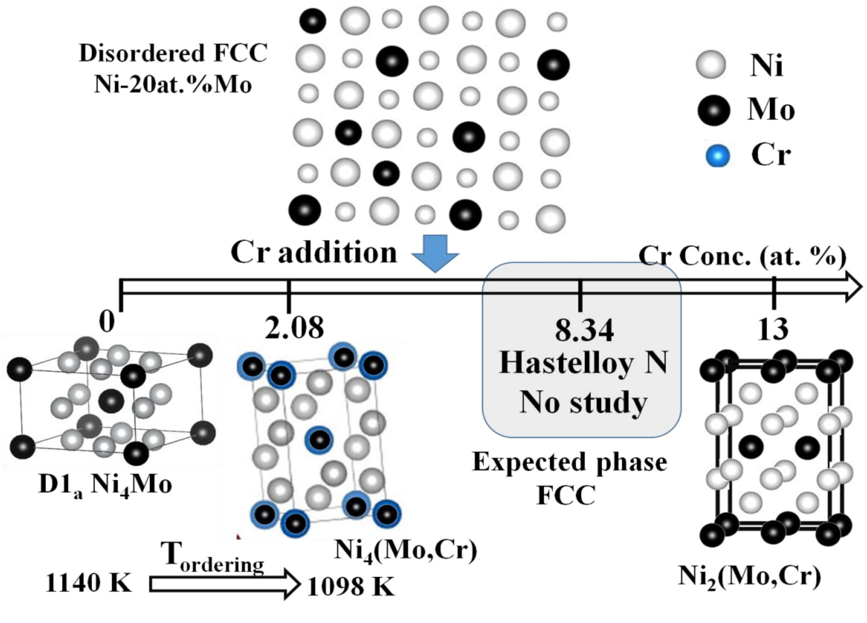

Fig. 4.1: Schematic diagram showing LRO transitions in Ni-Mo alloys with Cr addition.

In present study, the ordering tendencies in Ni-20 at.% Mo and Ni- 16 wt.% Mo- 7 wt.% Cr alloys (Mo+Cr ~20 at.%) are characterized using the EXAFS technique and TEM studies. The observed microstructure and nearest neighbour configurations obtained from the experimental investigations are correlated with the nearest neighbour interaction configurations and ground state energies evaluated from cluster expansion based approach coupled with first principle energy calculations for ordered and disordered systems. Based on experimental and simulation results, the role of Cr in altering the ordering characteristics of the alloy is rationalized.

Table 4.1: Composition of the alloy used in the present study.

Alloy	**Nominal composition (wt.%)**			**Experimentally determined composition (wt.%)**					
				EDS			**XRF**		
	Ni	Mo	Cr	Ni	Mo	Cr	Ni	Mo	Cr
Ni-Mo-Cr	77.0	16.0	7.0	76.4± 0.3	15.5± 0.3	7.1± 0.3	76.79± 0.09	16.22± 0.05	6.94± 0.01

4.2 Microstructural evolution in aged alloy

4.2.1 TEM investigations

SAED patterns recorded along the [001] zone axis for Ni-Mo-Cr alloy in as quenched condition show $<1\ \frac{1}{2}\ 0>_{\gamma}$ type SRO similar to the case of the binary Ni_4Mo alloy (Fig. 4.2 (a)). The $\{1\ \frac{1}{2}\ 0\}_{\gamma}$ spots for the ternary system are observed to be weaker in intensity as compared to the binary Ni_4Mo alloy. Such a result is not unexpected as the atomic scattering factors for electrons in Ni and Cr are very close, unlike the high contrast in the case of Ni-Mo. The presence of the SRO structure in Ni-Cr alloys has been unequivocally established by using neutron diffraction [108] and scattering experiments [109], where a large contrast between the scattering factors is present [110].

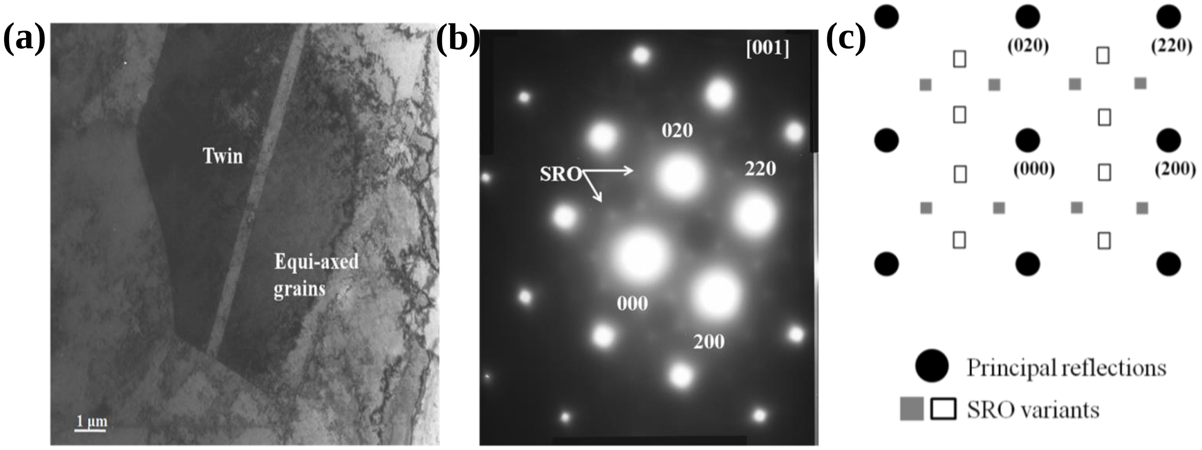

Fig. 4.2: (a) BF image and (b) diffraction pattern recorded along [001] zone axis for as quenched structure of Ni-Mo-Cr alloy and (c) a schematic showing SRO tendencies in alloy.

Ni-Mo-Cr alloy when subjected to same heat treatments as Ni_4Mo alloy, *viz.*, ageing at 1073 K for 4-50 h did not result in formation of any long range ordered phase of either Pt_2Mo or $D1_a$ type (Fig. 4.3 (a)-(b)) indicating that addition of Cr plays a major role in altering the nearest neighbour interaction energies and hence alters the ordering sequence. The EDS analysis of both the as quenched and the aged (at 1073 K for 4 h and 24 h) alloy samples match well with the composition chosen for the ternary alloy. In addition, fine inter-granular precipitates were observed in the aged alloy which are of type $(Ni_xMo_{1-x})_6C$, in agreement with the extensive literature reports [111-114]. No $Cr_{23}C_6$ type precipitates were observed in aged alloys. Han *et al.* [115] have shown that the type of carbide formed after ageing is dependent on relative concentrations of alloying additions and defined a quantity CR expressed as [114-115]

$$CR = \frac{Cr\ (at.\%)}{(Cr+Mo) in\ at.\%} \tag{4.1}$$

It was stated that when CR> 0.72, $Cr_{23}C_6$ type carbides dominate while when CR< 0.72, Mo rich M_6C type carbides form. For the Ni-Mo-Cr alloy, Cr and Mo contents are, respectively, 9 at.% and 10.8 at.% and hence, the quantity CR is evaluated to be 0.432 indicating that Mo rich M_6C carbides will form in the alloy after ageing. However, the phase fraction of these precipitates was not appreciable (<5wt.%) as they could not be observed in the XRD patterns and hence are expected to have minimal effect on ordering tendencies in the Ni-Mo-Cr alloy. Since electronic structure factors for Ni and Cr are very similar due to close atomic numbers, EXAFS study was undertaken to investigate the local structural change in Ni-Mo and Ni-Mo-Cr alloy under different heat treatments. Similarly, the measurement of Vicker's hardness for the alloy aged at 973 K as a function of ageing time indicate that there is no appreciable change in the hardness values as no LRO precipitates have developed after ageing.

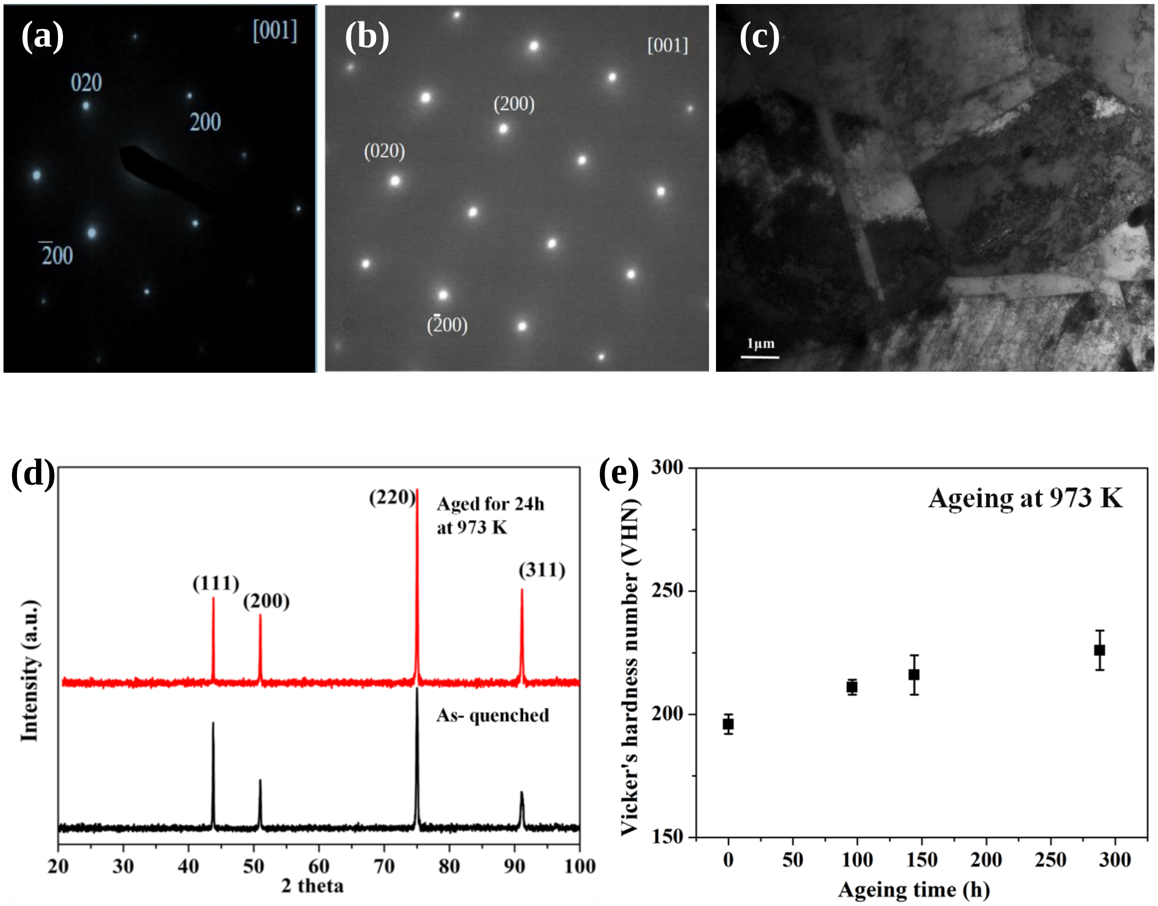

Fig. 4.3: Diffraction pattern recorded along [001] zone axis for Ni-Mo-Cr alloy aged at (a) 973 K for 4 h and WQ, and (b) 973 K for 24 h and WQ. (c) Bright field image of the alloy aged for 24 h and WQ, (d) XRD patterns for as quenched and aged alloy, and (e) Variation of Vicker's hardness number as a function of ageing time.

4.2.2 EXAFS study

The experimental EXAFS spectra ($\mu(E)$ *versus* energy (E) plot) for as quenched Ni_4Mo and as quenched Ni-Mo-Cr alloy corresponding to Ni K_α edge is presented in Fig. 4.4. The inset shows the FT-EXAFS spectra ($|\chi|_{mag}(r)$ *versus* r plot) which provide information about the distances of the neighbouring atoms from the centre of the absorbing atom Ni. From the figure, it is evident that a prominent peak occurs at~ 2.2 Å for both the binary and the ternary alloy. There is no appreciable change in the peak positions but the peak heights are decreased in the as quenched Ni-Mo-Cr alloy as compared to the as quenched Ni_4Mo alloy. Since the peak height in EXAFS oscillations depends on the surrounding atoms, it indicates that addition of Cr leads to changes in the local atomic structure around the Ni atoms at the first near neighbour distance. After Cr addition, the structural disorder around the Ni atoms is increased as indicated by the decrease in the peak amplitude for the ternary alloy. Similar observations were recorded in case of Al-Si-Sr and Al-Sr alloys where Si addition changes the local atomic environment around Sr atoms [116].

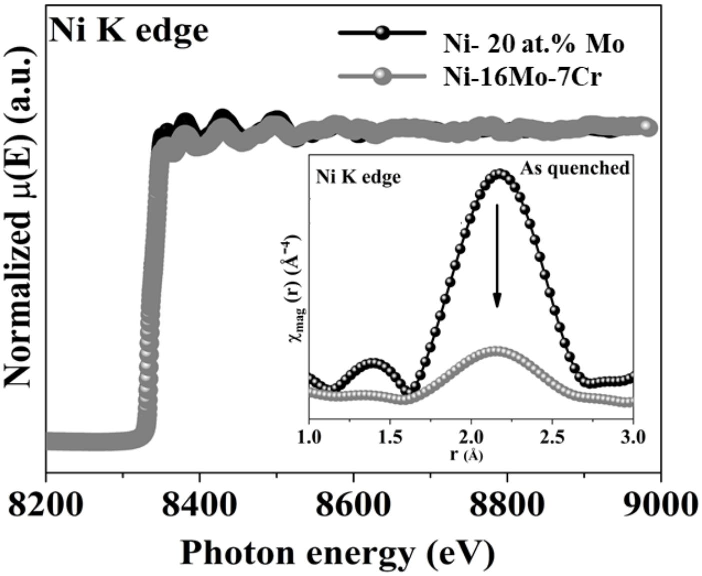

Fig. 4.4: Plot of normalised μ(E) *versus* E for as quenched Ni_4Mo and Ni-Mo-Cr alloy. The inset shows a plot of $|\chi|_{mag}(r)$ *versus* r for the same.

The EXAFS spectra corresponding to Ni, Cr and Mo K_α edge is shown in Fig. 4.5. There is no change in the absorption edges of Ni, Cr and Mo for the as-quenched and aged alloy indicating that that there is no change in the chemical state of the element as expected.

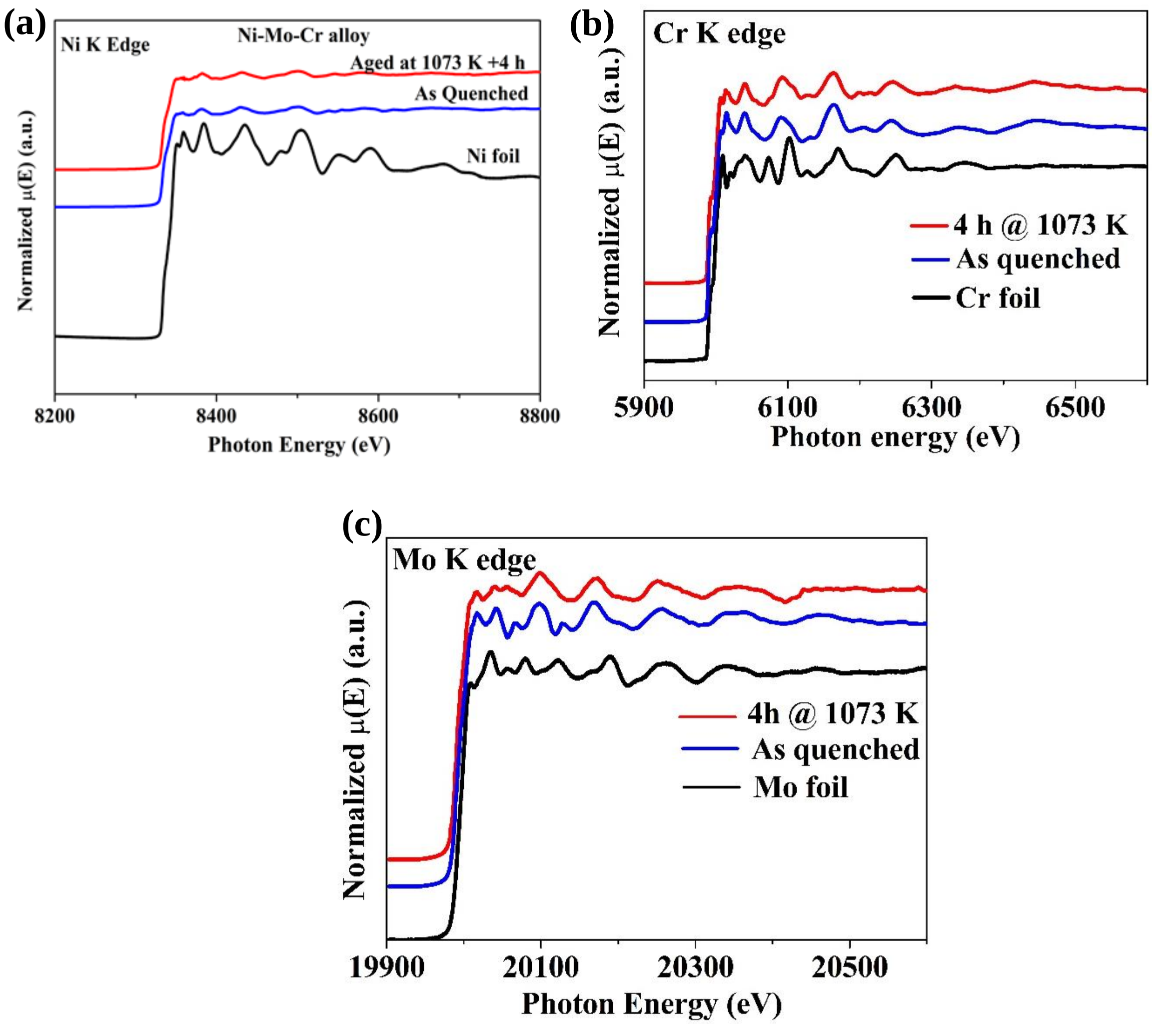

Fig. 4.5: Experimental EXAFS spectra recorded at (a) Ni, (b) Cr and (c) Mo K absorption edges for as-quenched Ni-Mo-Cr alloy and Ni-Mo-Cr alloy aged at 1073 K for 4 h (and WQ). The spectra recorded for standard Ni, Cr and Mo foils for calibration are also shown for comparison.

The experimental FT-EXAFS spectra are fitted with the theoretically simulated $|\chi|_{mag}(r)$ *versus* r plots. The theoretically simulated spectra were modelled from an fcc lattice having a lattice parameter of 3.58 Å with Cr/Mo concentration set equal to the experimental alloy composition. The lattice parameter was calculated from the modified Vegard's relationship expressed by [117]

$$a_{alloy} = a_{Ni} + (20-x)\,V_{Cr} + x\,V_{Mo} \tag{4.2}$$

where a_{Ni} is the lattice parameter of pure nickel (= 3.525 Å) [117, 118], V_{Cr} = 0.0022 Å/at.% and V_{Mo}=0.0051 Å/at are Vegard's coefficients for Cr and Mo, respectively [119]. The experimental plots of $|\chi_{mag}(r)|$ *versus* r along with their theoretical best fitted curves for both as quenched and aged Ni-Mo-Cr alloy are presented in Fig. 4.6. From the fit, the values of bond lengths (r), coordination number around the atoms (N) and Debye Waller factors (σ^2) corresponding to the corresponding to the first coordination shell are evaluated, and, are presented in Table 4.2.

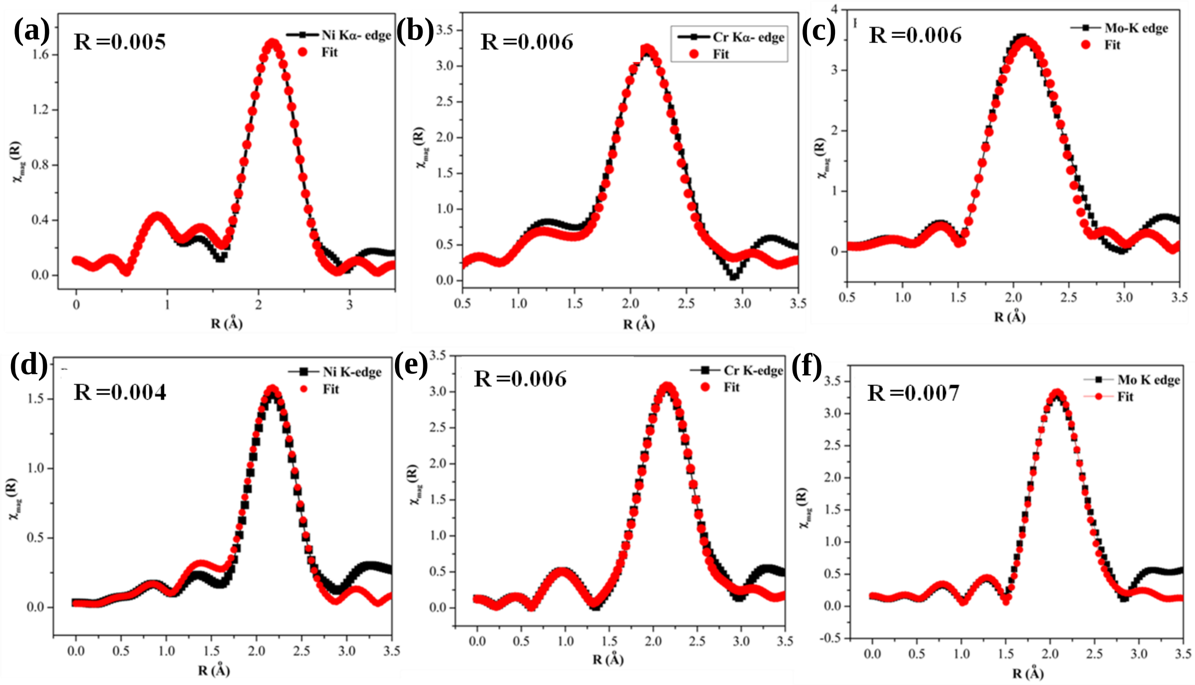

Fig. 4.6: Experimental $|\chi_{mag}(r)|$ *versus r* plots for (a)-(d) Ni K edge, (b)-(e) Cr K edge and (c)-(f) Mo K edge for as the quenched and the aged alloy samples (ageing treatment given at 1073 K for 4 h and WQ).

It is evident from Fig. 4.6 that there is no significant change in the bond lengths or Debye Waller factors for Ni, Cr and Mo atoms with the ageing treatment. Both Cr and Mo are coordinated with 12 Ni atoms in the first shell with slightly different bond lengths indicating that ageing treatment did not induce any appreciable change in the local structure around Ni, Cr and Mo atoms. In addition, no Cr-Mo bonds were observed. The Ni-Mo bond length obtained from the EXAFS measurements are in close agreement with the values reported by Li *et al.* [120]. The slight difference in the observed value of Ni-Cr bond length and those reported in literature is mainly attributable to the fact that the Ni-Ni bonds are considered for the fitting in present study while it is not considered by Li *et al.* [120] in their analyses which results in the overall minor difference between the Ni-Cr bond lengths.

Table 4.2: EXAFS fit for as quenched and aged (1073 K/4 h+WQ) Ni-Mo-Cr alloy showing the values of the bond lengths (r), average coordination number around the atom (N) and the Debye Waller factor (σ^2) corresponding to the first coordination shell. The values in the parenthesis are the reported values in literature [120,121].

		Ni-Mo-Cr as quenched (fcc str.)			**Ni-Mo-Cr aged at 1073 K /4 h (fcc str.)**		
Edge	Bond type	r (Å)	N	σ^2(Å^2)	r (Å)	N	σ^2(Å^2)
Ni edge	**Ni-Ni**	2.49±0.01	9.9±0.8	0.00099 ±0.0008	2.49±0.01	8.7±0.6	0.0097±0.0010
	Ni-Mo	2.51±0.02	1.9±0.5	0.0048±0.0006	2.53±0.03	1.5±0.5	0.0038±0.0013
	Ni-Cr	2.47±0.01	1.4±0.3	0.0015±0.0007	2.48±0.02	1.1±0.3	0.0011±0.0008
Mo edge	**Mo-Ni**	2.50±0.01 (2.53)	12.3±0.7 (11.6 ±0.7) [120]	0.0061±0.0004	2.51±0.01	10.2±0.8	0.0049±0.0019
Cr edge	**Cr-Ni**	2.45±0.03 (2.50)	11.6±0.6 (11.2±0.7) [120,121]	0.0070±0.0011	2.47±0.01	9.3±0.9	0.0053±0.0010

4.3 First principles calculations

The structural parameters obtained from EXAFS were further compared with the results of the first principles calculations performed on the disordered fcc matrix of the Ni-Mo-Cr alloy generated by the SQS approach as developed by Zunger *et al.* [98]. To observe the effect of Cr addition on the stability $D1_a$ structure, which forms in case of binary Ni-Mo alloys, but could not be found in Ni-Mo-Cr alloys, first principles calculations were performed on Cr-doped $D1_a$ structure with Cr occupying Mo site.

4.3.1 Generation of optimized SQS configuration

In the present study the SQS structure for the fcc configuration of Ni-Mo-Cr alloy was generated using 20 atoms/unit cell. The optimized SQS structure is shown in Fig. 4.7 and the corresponding lattice vectors and atomic positions are summarized in the Table 4.3. The maximum diameter considered for pair and triplet cluster are 4.4 Å and 3.59 Å, respectively.

Table 4.3: Atomic positions of Ni, Cr and Mo in 20-atom/unit cell SQS structure.

Lattice Vectors	Atomic Positions (Fractional Coordinates)			
$a_x=(-1,\frac{1}{2},\frac{-3}{2})\ a_0$	Ni	0.5	1.0	1.0
	Ni	1.0	1.0	1.0
	Ni	0.6	0.2	0.2
$a_y=(\frac{3}{2},\frac{1}{2},1)\ a_0$	Ni	0.75	0.5	1.0
	Ni	0.10	0.2	0.2
	Ni	0.25	0.50	1.0
$a_z=(\frac{3}{2},2,\frac{-3}{2})\ a_0$	Ni	0.55	0.1	0.6
	Mo	0.70	0.4	0.4
	Ni	0.85	0.7	0.2
a_0 is the lattice parameter of the fcc structure	Ni	0.05	0.1	0.6
	Ni	0.2	0.4	0.4
	Mo	0.35	0.7	0.2
	Ni	0.65	0.3	0.8
	Cr	0.8	0.6	0.6
	Ni	0.95	0.9	0.4
	Ni	0.15	0.3	0.8
	Ni	0.3	0.6	0.6
	Cr	0.45	0.9	0.4
	Ni	0.9	0.8	0.8
	Ni	0.4	0.8	0.8

The generated pair and triplet correlation functions are compared with the theoretical correlation functions for completely random alloy to verify whether the SQS structure embodies the short-range statistics of the random alloy (Table 4.4) or not. From the table, it is observed that the pair and triplet correlations match well with the actual correlations with a small mismatch in the range -0.00625 to 0. 025. The SQS can mimic the actual disordered fcc configuration of the alloy up to third nearest neighbour with reasonable accuracy.

Table 4.4: Pair and triplet correlation functions for the 20 atom/unit cell SQS structure and completely random fcc solid solution with Mo=0.1 and Cr=0.1 atomic fraction.

Cluster type n_α	**Cluster Diameter (Å) l_α**	**Calculated Correlation (ρ)**	**Actual correlation (ρ_a)**	**Correlation Mismatch (ρ-ρ_a)**
2	2.54	0.49375	0.49	0 .00375
2	2.54	0	0	0
2	2.54	-0.00625	0	-0.00625
2	3.59	0.475	0.49	-0.015
2	3.59	0	0	0
2	3.59	-0.025	0	-0.025
2	4.40	0.49375	0.49	0.00375
2	4.40	0	0	0
2	4.40	-0.00625	0	-0.00625
3	2.54	-0.339	-0.343	0.00394
3	2.54 (2)	0	0	0
03	2.54	0.00156	0	0.00156
3	3.59	-0.3625	-0.343	-0.0195
3	3.59 (3)	0	0	0
3	3.59	0.625	0	0.00625
3	3.59	0.025	0	0.025

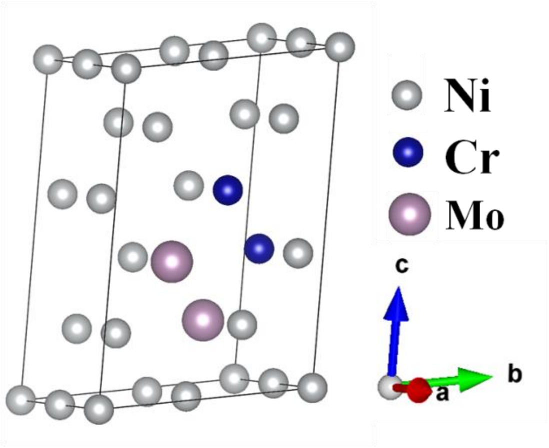

Fig. 4.7: Optimized 20-atom/unit cell SQS for disordered fcc configuration of Ni-Mo-Cr alloy.

4.3.2 Enthalpy of mixing and bond length analysis

The enthalpy of mixing for the Ni-Mo-Cr alloy was calculated from the equation

$$\Delta H\ (Ni_{0.8}Mo_{0.1}Cr_{0.1}) = E(Ni_{0.8}Mo_{0.1}Cr_{0.1}) - 0.8E(Ni) - 0.1E(Mo) - 0.1\ E(Cr) \qquad 4.3$$

where *E(Ni), E(Mo)* and *E(Cr)* are the reference energies of the pure components in their respective ground states. The spin polarized calculations were performed on the ferromagnetic fcc Ni and the anti-ferromagnetic bcc Cr, but not for the bcc Mo as it is non-magnetic. All the Ni-Mo-Cr phases are non-magnetic [122]. The first principles calculations on bulk Ni, Mo and Cr yields the respective energy values -5.51 eV/atom, -9.84eV/atom and -9.46 eV/atom. The enthalpy of formation for the SQS Ni-Mo-Cr alloy is found to be -0.32 eV/atom. The negative value of enthalpy of formation for SQS Ni-Mo-Cr alloy shows that the disordered fcc phase is stable at 0 K. Furthermore, this value is higher than the enthalpy of formation of SQS fcc Ni-20 at.% Mo structure (-0.28 eV/atom) which suggests that the addition of Cr in Ni-Mo alloys stabilizes disordered fcc structure.

The bond lengths for the optimized SQS structure were analyzed and it was observed that the average Ni-Ni, Ni-Mo and Ni-Cr bond lengths are equal having a value of 2.50±0.1 Å. The value is close to the value obtained from the EXAFS fit (Table 4.5). However, the SQS model could not detect the minute variations in the Ni-Cr, Ni-Ni and Ni-Mo bond lengths which are easily observable in EXAFS analysis which emanates from the SRO structure present in the alloy.

Table 4.5: Ni-Ni, Ni-Mo, Ni-Cr bond lengths for the first coordination shell obtained from EXAFS fit of the spectra for as quenched and aged Ni-Mo-Cr alloy compared with the predicted values from VASP calculations on SQS structure and theoretical fcc structure.

Bond type	Bond lengths (Å)			
	As quenched alloy EXAFS Result	Alloy aged at 1073 K for4h EXAFS Result	SQS structure	Theoretical FCC
Ni-Ni	2.49±0.01	2.49±0.01	2.5±0. 1	2.51
Mo-Ni	2.51±0.02	2.53±0.03	2.5±0. 1	2.51
Cr-Ni	2.47±0.01	2.48±0.02	2.5±0.1	2.51

4.3.3 Cr substituted $D1_a$ phase

VASP calculations performed on ordered Ni_4Mo phase ($D1_a$ structure) with Cr substituted at Mo site show that the enthalpy of formation for the binary $D1_a$ phase with no Cr addition (-0.298 eV/atom) is more negative that of Cr substituted at Mo site in $D1_a$ phase (-0.13 eV/atom). This indicates that with Cr addition the stability of $D1_a$ phase decreases which is consistent with the present results and those reported earlier by Arya *et al.* [14, 123]. On the other hand, the enthalpy of formation for disordered fcc Ni_4Mo is found to be -0.289 eV/atom; while that of disordered fcc Ni-Mo-Cr alloy (with Mo+Cr concentration) was obtained as -0.325 eV/atom indicating that the disordered phase is stabilized with Cr addition. The evaluated trend in Gibbs free energy is in accordance with the study carried out by Song *et al.* [124]

4.4 Cluster expansion based calculations

Rigorous EXAFS analysis and first principles calculations show that the Cr addition leads to a change in the local structural environment around Ni/Mo atom. This may result in the variation of the nearest neighbour interaction energies which dictate the ordering tendencies. Based on the EXAFS studies on Ni-Mo-Cr alloys, we observe that Cr and Mo are surrounded by 12 Ni atoms *i.e.*, Cr and Mo preferentially bonds with Ni. Hence, we can qualitatively observe the change in ordering tendencies by comparing the effective interaction parameters for Ni-Mo and Ni-Cr system. The comparison is expected to be valid since Mo and Cr concentration is low and these atoms can have all Ni atoms as their first nearest neighbour.

4.4.1 Ni-Cr system

The DFT energies calculated by VASP as a function of solute concentration for Ni-Cr system based on the fcc lattice is generated from the pure Ni, Cr and known Ni-Cr intermetallics. The convex energy hull obtained for Ni-Cr system is presented in Fig. 4.8. The DFT energies are then fitted with CE model to extract the pair and multisite interaction energies (ECIs) upto 11^{th} nearest neighbour duplets, 4^{th} nearest neighbour triplets and 1^{st} nearest neighbour quadruplet. The empty cluster interaction defines the total energy of the disordered state at equiatomic concentration; while the point cluster interaction energy depends on the concentration of solute in a linear fashion [88, 91, 100]. The fit between DFT and CE energies is a straight line with a small deviation distributed evenly over the whole range of calculations given by a small value of cross validation score of (± 27 meV/atom). The representative clusters considered in present study and their multiplicity is plotted in Fig. 4.8 (c)-(d).

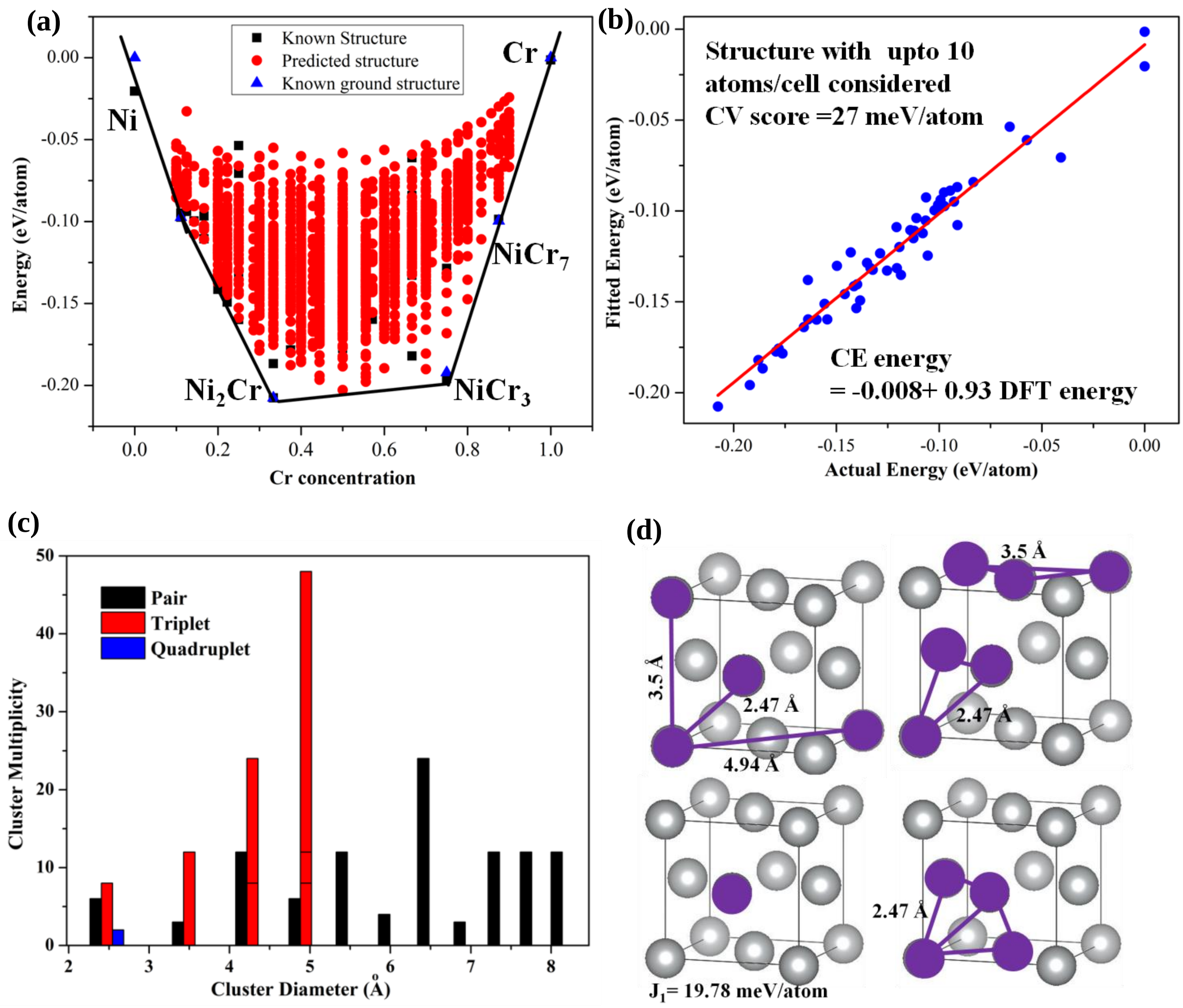

Fig. 4.8: (a) Formation energies of different stable and metastable phases present in Ni-Cr system. The black squares correspond to the energies of the structures calculated by VASP, the red dots show the energy obtained from the fitted CE energy functional and triangles in the convex hull line indicate ground states, (b) Fit between VASP calculated energies and the energy of same structure obtained by CE fit, (c) Cluster multiplicity *versus* cluster diameter and (d) representative clusters (pair, triplet and quadruplets).

The ECI values calculated for the Ni-Cr system is plotted in Fig. 4.9. The ECIs are generated by pair clusters upto 11th nearest neighbour (NN) distance (7.82 Å), triplets upto 4th NN (4.94 Å) and one quadruplet cluster (2.47 Å). The ECI parameter for the pair cluster corresponding to the first nearest neighbour has a positive value indicating the tendency for ordering. The values of ECI parameters for the multi-body (triplets and quadruplets) clusters were much smaller as compared to 2-point or pair clusters indicating a good convergence of CE model [88-92]. Additionally, it was observed that for 2-point cluster, the magnitude of the ECI decreases with increase in cluster diameter which indicates that only the first few nearest neighbour interactions play a crucial role in the configurational energy of the alloy.

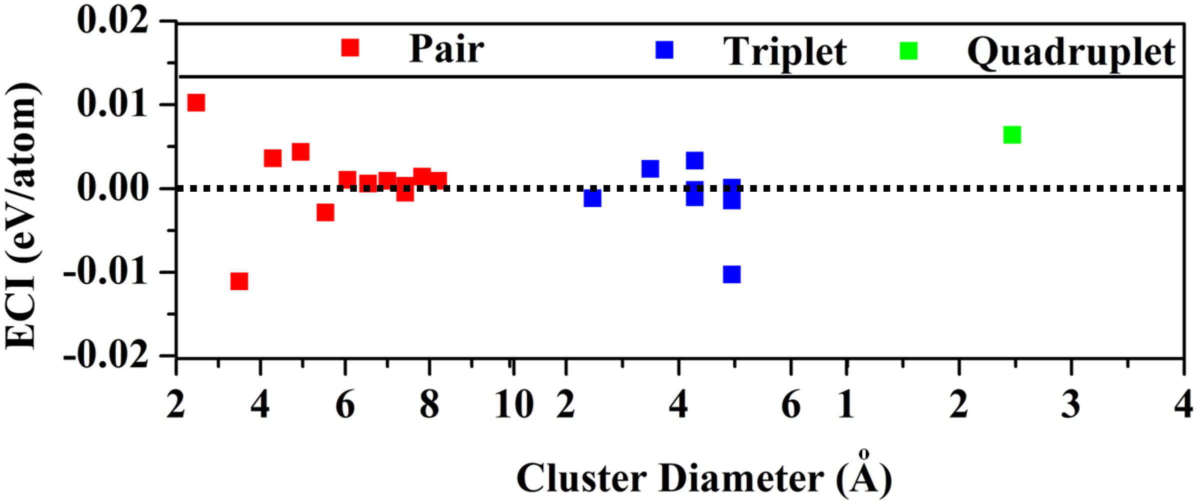

Fig. 4.9: Effective cluster interaction parameters corresponding to pair, triplet and quadruplet clusters calculated for fcc Ni-Cr system.

4.4.2 Cr-Mo system

Cluster expansion calculations to evaluate the ECI parameters were carried out for Cr-Mo system based on the fcc lattice. The convex energy hull (Fig. 4.10) shows that there are no intermetallics formed between Cr and Mo consistent with the experimental observations. A good match between the VASP calculated energies and the energies of the structure obtained by cluster expansion fit was obtained as indicated by a low value of the CV score of ± 1 meV/atom.

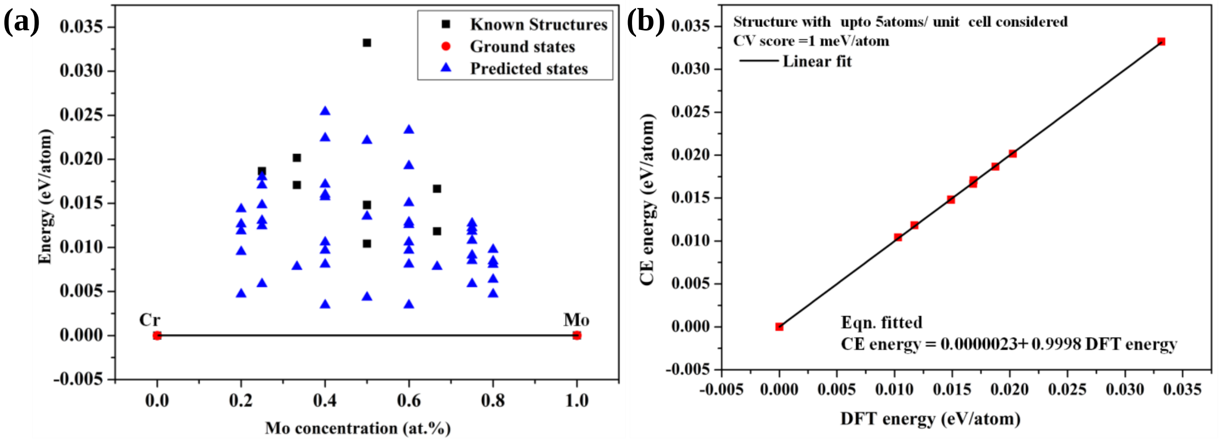

Fig. 4.10: Output of MAPS algorithm for Cr-Mo binary system showing (a) Formation energies of different stable and metastable phases present in fcc Cr-Mo system calculated by VASP and predicted by CE fit, and (b) Fit of actual energy (by VASP) *versus* energies predicted by CE model.

The ECIs are generated by pair clusters upto 5th nearest neighbour distance (6.09 Å), one triplet (3.51 Å) and one quadruplet cluster (3.51 Å). The ECI for the nearest neighbour distance has a small negative value suggesting a slight tendency for clustering between Cr and Mo atoms. The cluster diameter, multiplicity and corresponding ECIs are summarized in Table 4.6.

Table 4.6: Summary of ECIs, cluster diameter, cluster multiplicity for Cr-Mo system based on fcc lattice. Cluster diameter is defined as the longest distance between the vertices of any cluster. The cluster type 0, 1, 2 and 3 denote empty, point, pair and triplet clusters.

Cluster type	Cluster Diameter (Å)	Multiplicity	ECI (eV/atom)
0			0.013384
1			-0.003940
2	3.045000	4	-0.004377
2	3.516063	3	-0.000325
2	4.972464	6	0.000306
2	5.830731	12	0.000075
2	6.090000	4	0.000465
3	3.516063	12	0.000329
4	3.516063	6	0.000085

The ECI values for Ni-Cr system was compared with Ni-Mo [105] and Cr-Mo system. It was observed that both Ni-Mo and Ni-Cr has higher magnitude of ECI values as compared to the Cr-Mo system.

4.5 Discussion of results

4.5.1 Role of Cr in changing stability of $D1_a$ phase

The enthalpy of formation for $D1_a$ phase with Cr substituted at Mo site is -0.13 eV/atom However, comparison of the enthalpy of formation for pure $D1_a$ phase (-0.298 eV/atom) with that for Cr substituted $D1_a$ phase, indicates that with Cr addition the stability of $D1_a$ phase decreases which is consistent with the TEM and EXAFS analyses where the $D1_a$ phase was not observed in case of aged specimen.

4.5.2 Role of Cr in changing the relative stability of Ni-Mo and Ni-Mo-Cr disordered fcc alloy

As shown in previous sections, the enthalpy of formation becomes more negative for the disordered Ni-Mo-Cr fcc (-0.32 eV/atom) as compared to disordered Ni_4Mo (-0.289 eV/atom). The configurational entropy in the limit of high temperature or for completely random alloy is expressed as

$$S_{random} = -k_B \sum c_i ln c_i \qquad 4.4$$

Where k_B is the Boltzman constant having a value of 8.617×10^{-5} eVK^{-1} of and c_i is the atomic fraction of the i^{th} constituent element. The calculated entropies for disordered fcc Ni_4Mo and Ni-Mo-Cr alloy are given in Table 4.7. It is evident from the table that the entropy increases with ternary element addition thereby making the resultant Gibbs free energy more negative for the ternary alloy.

Table 4.7: Calculated entropy for the disordered Ni_4Mo and Ni-Mo-Cr alloy.

Alloy	**Elemental concentration (atom fraction) (c_i)**			**Entropy**
	Ni	Mo	Cr	
Ni_4Mo	0.8	0.2	-	0.50 k_B
Ni-Mo-Cr alloy	0.8	0.1	0.1	0.64 k_B

4.5.3 Effect of Cr on ordering tendencies in Ni-Mo-Cr alloy

The ordering in any binary alloy $A_{1-x}B_x$ or ternary alloy $A_xB_yC_z$ can further be quantified using Warren Cowley parameters [96]. From EXAFS fit, the probability is calculated by calculating the number of A-B bonds and total number of bonds N is taken to be equal to the coordination number 12 for present study ($P_m^{AB} = \frac{N_{A-B}}{N}$) [125]. α is calculated to be -0.228 ($\pm$0.004) for as quenched Ni_4Mo which is close to the reported value of -0.2 [106] as discussed in chapter 3. Similarly, for ternary Ni-Mo-Cr alloy the Warren Cowley parameters corresponding to the first neighbouring shell are deduced and presented in Table 4.8. The negative values of α^{Ni-Mo} and α^{Ni-Cr} indicates a preference for the formation of bonds between unlike atoms, Ni-Mo and Ni-Cr. The value $\alpha^{Cr-Mo} = 1$ arises due to N_{Cr-Mo} =0, indicating that Cr-Mo do not prefer each other as the nearest neighbour. The EXAFS analysis clearly establishes that the SRO tendency is prevalent in Ni-Mo-Cr alloy even after ageing which could not be resolved by the conventional electron microscopy images.

Table 4.8: Warren Cowley parameters for the first NN shell calculated from EXAFS fit.

Warren Cowley parameters			
As quenched	$\alpha_{Mo-Ni} = -0.22 \pm 0.03$	$\alpha_{Cr-Ni} = -0.35 \pm 0.03$	$\alpha_{Cr-Mo} \geq 0$
Aged alloy	$\alpha_{Mo-Ni} = -0.14 \pm 0.01$	$\alpha_{Cr-Ni} = -0.25 \pm 0.01$	$\alpha_{Cr-Mo} \geq 0$

In case of Ni-Mo-Cr alloys, the absence of Mo-Cr bonds in EXAFS fit indicates the bonding of Cr and Mo atoms with Ni atoms. This bonding is preferential rather than random as the number of Mo atoms around Cr atom is not equal to its atomic concentration in the alloy (Table 4.9). This indicates that the Cr substitutes Mo in the fcc lattice. Similar preferential bonding between Si and Sr atoms in Al-Si-Sr type alloys is observed using EXAFS analysis [116]. Though Cr and Ni have similar atomic radius, EXAFS study as well as previous work carried out by Arya *et al.* [5, 14], Verma *et al.* [12-13, 37-38, 126] and Vasudevan *et al.* [21, 22], suggest that Cr replaces Mo in place of Ni in the fcc lattice as it changes the chemical interaction energies which govern ordering characteristics of Ni-Mo-Cr alloys.

Table 4.9: Number of Ni-Ni, Ni-Mo and Ni-Cr bonds in as quenched and aged Ni-Mo-Cr alloy, and their comparison with the SQS structure as well as theoretical fcc structure.

	Number of bonds			
Element	**EXAFS fit As Quenched alloy**	**EXAFS fit 1073 K+4 h**	**SQS structure**	**Theoretical dis. fcc**
Ni-Ni	9.9±0.8	8.7±0.6	9-10	9.6
Ni-Mo	1.9±0.5	1.5±0.5	2-3	1.4
Ni-Cr	1.4±0.3	1.1±0.3	1-2	1

If Cr were distributed randomly in the fcc lattice, then Cr would have occurred in positions of both Ni and Mo atoms resulting in decrease in Ni-Mo bonds and presence of Cr-Mo bonds, but absence of these bonds excludes the possibility of Ni substitution by Cr (Fig.4.11). The EXAFS study along with first principles calculations clearly establish that Cr substitutes Mo and destabilizes the LRO phase of $D1_a$ type.

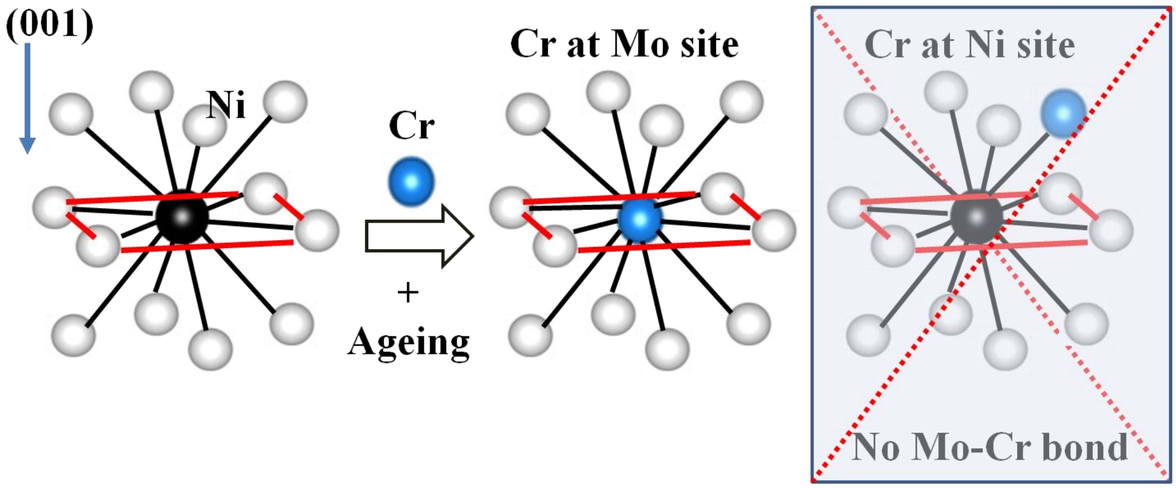

Fig. 4.11: Schematic showing the first NN shell around Mo atom in binary Ni-Mo alloy and subsequent Cr atom substitution in the fcc lattice.

Furthermore, the ECIs obtained from CE calculations on Ni-Cr, Ni-Mo and Cr-Mo systems reveal the relative ordering tendencies in the alloy. Cr-Mo interaction energies are very less and can be neglected as compared to Ni-Mo and Ni-Cr systems. Also, the ECI values for Ni-Cr and Ni-Mo system are appreciable till 4th NN distances indicating that the interactions upto 4th NN play a dominant role in determining the configurational energy of the alloy consistent with the reported literature. The values of pair ECI for the first and third nearest neighbour for both Ni-Mo and Ni-Cr systems are positive indicating ordering tendencies, but the magnitude decreases for Ni-Cr system indicating that the strength of first NN interaction decreases (Fig. 4.12). Similarly, the sign for the triplet ECIs also change for first nearest neighbour triplet (Fig. 4.12). Overall, the pair and multisite interaction energies are such that the ordering tendency is reduced after Cr addition.

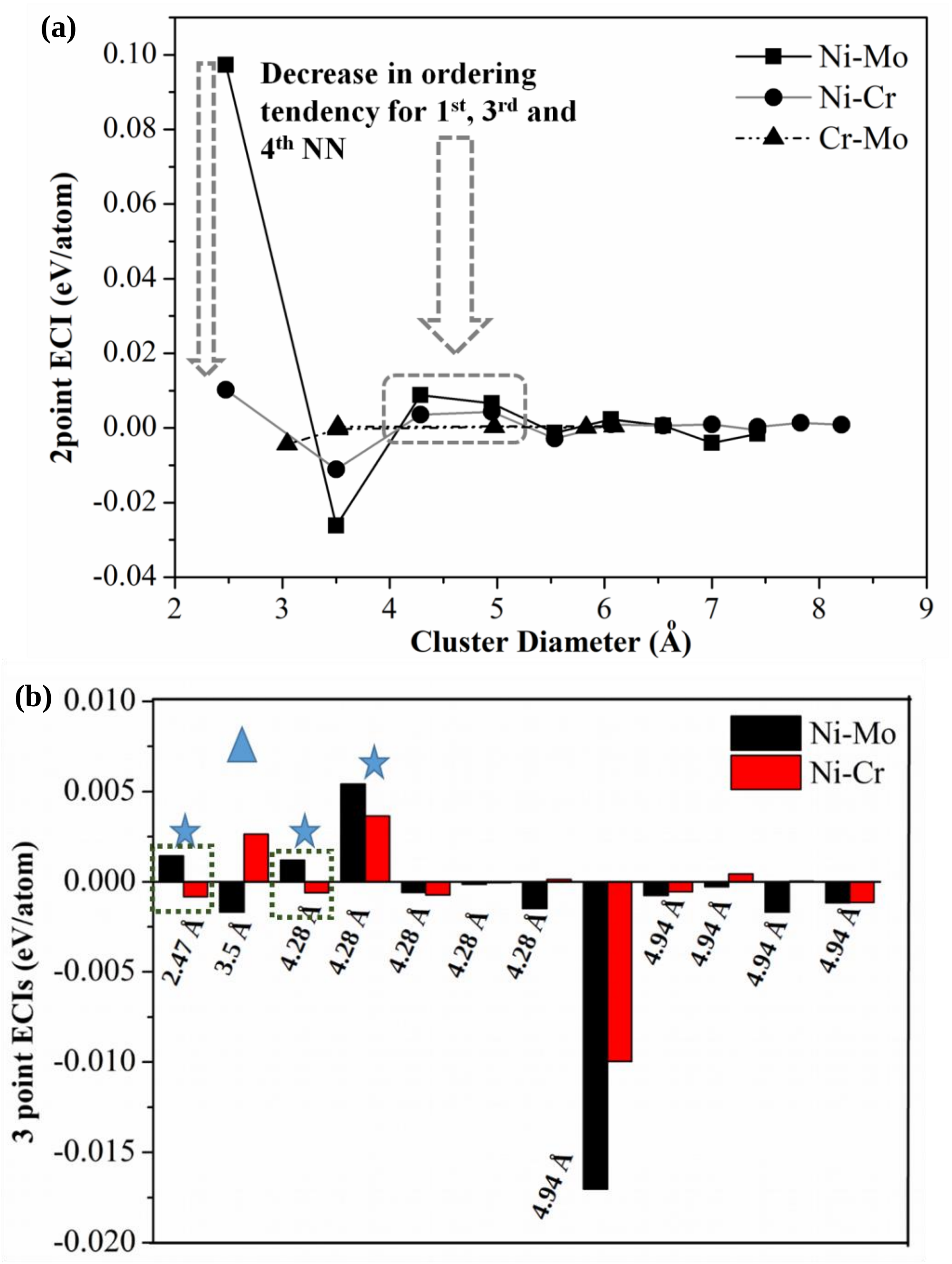

★ **Decrease in ordering tendency for 1st ,3rd and 4th NN triplets**

▲ **2nd NN triplet increases ordering tendency but 2nd NN pair cluster is more dominant which has the disordering tendency**

Fig. 4.12: Comparison of (a) pair interaction parameters and (b) triplet interaction parameters for Ni-Mo and Ni-Cr system.

The addition of ternary element, Cr thus changes the thermodynamic driving force for ordering (both SRO and LRO) by suitably altering the entropy as well as the enthalpy. In enthalpy part, the ternary element addition leads to a change in the pair and multisite interaction energies.

This is opposite to the case of irradiation where kinetics of phase formation is altered and many metastable states are also observed [6]. The disordered fcc phase of Ni-Mo-Cr alloy is more stable as compared to fcc Ni_4Mo alloy since Cr stabilizes the disordered phase by lowering the formation energy. A similar trend is observed with Fe addition [6, 42]. The $D1_a$ configuration, however, is destabilised with Cr addition since Cr is known to promote the formation of $Pt_2(Mo,Cr)$ type phase over $Ni_4(Mo,Cr)$ phase and Ni_4Cr is not thermodynamically stable. Mo on the other hand stabilises both SRO and LRO [6]. Chan *et al.* [127] and Hu *et al.* [128] suggested that the formation energy of $Ni_2(Cr, Mo)$ is lowered by Mo addition upto 8.3 at.% Mo. However, in the present study no Pt_2Mo type precipitates were observed as Mo+Cr content was < 33 at.% and Mo content was > 8.3 at.%. Furthermore, Mo addition results in lowering of diffusivity of Cr in a Ni-base alloy [6]. Thus the thermodynamic driving force as well as kinetics both are not favourable for the formation of the ordered $Ni_2(Cr,Mo)$ phase. The absence of $Ni_2(Mo,Cr)$ in the ternary alloy can thus be rationalized.

A schematic Gibbs free energy diagram depicting the effect of Cr addition on Ni-Mo alloys is presented in Fig. 4.13 which shows that the disordered fcc phase of Ni-Mo-Cr alloy is more stable as compared to the binary fcc Ni_4Mo alloy because of the additional configurational entropy due to the ternary Cr addition, while the formation energy (or enthalpy) of the ordered $D1_a$ structure increases with Cr addition. The net result is that, at a certain level of Cr content, the disordered fcc solid solution becomes more stable than the ordered $D1_a$ phase. Results from the present experiments show that the substitution of Mo by 7 wt.% Cr in Ni-20 at.% Mo alloy definitely makes the disordered solid solution thermodynamically more stable than the corresponding ordered ($D1_a$) structure.

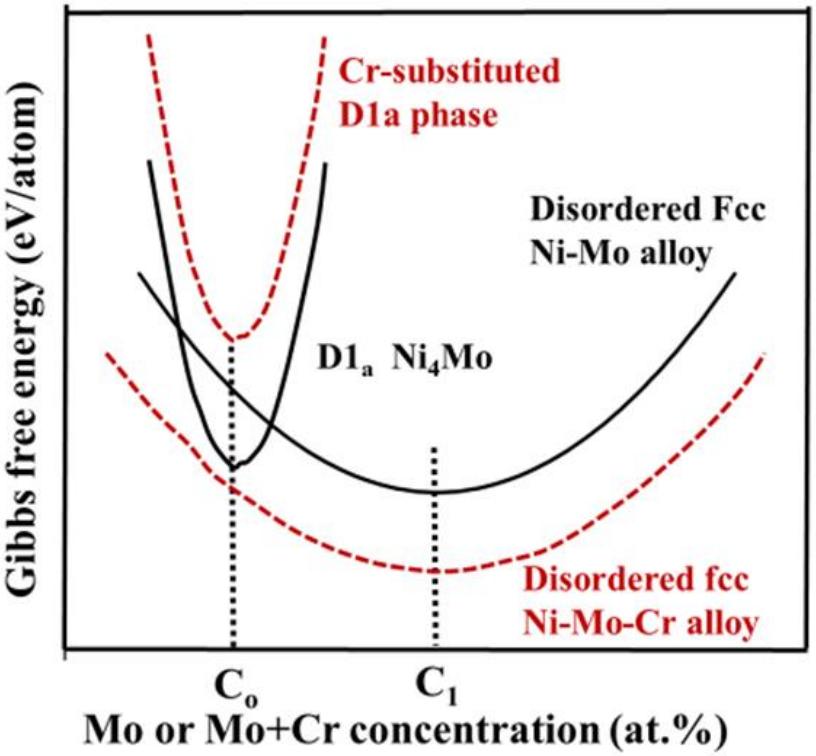

Fig. 4.13: Schematic diagram showing the effect of Cr concentration on Gibbs free energies of ordered and disordered phases of Ni-Mo and Ni-Mo-Cr alloys. The dashed vertical line marked C_0 corresponds to 20 at.% Mo or Mo+Cr and that marked C_1 corresponds to 50 at.% Mo or Mo+Cr in the diagram.

4.6 Summary

Present study investigates the ordering tendencies in Ni_4Mo and Ni-Mo-Cr alloy (Mo+Cr content =20 at.%) using experimental and simulation techniques and elucidates the role of Cr addition on the ordering characteristics of the Ni-Mo-Cr alloy. The binary Ni-20 at.% Mo shows formation of long range ordered precipitates upon ageing while the formation of the long range ordered $D1_a$ phase is suppressed in the ternary alloy when given the same heat treatments. This is attributed to the change in local chemical environment around the Ni atoms caused by Cr atoms which replace Mo atoms in the fcc lattice. As a result, the sign of nearest neighbour chemical interaction energies which govern the ordering tendency is reversed and the tendency for the formation of $D1_a$ phase is suppressed.

Chapter 5 : Microstructure property correlation in the Ni-Mo-Cr alloy exposed to FLiNaK salt

5.1 Background

The resistance of any material to severe corrosive attack is determined by the stability of protective surface films and the efficacy of their acting as a diffusion barrier against the outward diffusion of the constituent elements from the alloy matrix [129]. In most of the Ni-based alloys, Cr and Al are added in the alloy to promote the formation of alumina (Al_2O_3) or chromia (Cr_2O_3) in high temperature oxidizing environment thereby providing the required oxidation resistance [130, 131]. However, in a molten salt environment the formation of protective surface films is precluded and the alloy under goes a corrosive attack [38, 132].

Corrosion of the structural alloys by fluoride melts is thermodynamically driven where selective dissolution of alloying elements occurs into the molten fluoride [38, 133-134]. The dissolution tendency of different metals in fluoride melt is dictated by the Gibbs free energy of fluoride formation. Other mechanisms of corrosion include (a) impurity driven corrosion due to the presence of moisture, HF and high valence ions such as Cr^{3+} [38, 134], (b) galvanic corrosion between the elements in molten salt and a chosen structural alloy [38, 134], (c) temperature gradient-driven corrosion due to temperature dependent elemental solubility in molten salt and (d) salt redox potential [38, 132] which are discussed in section 1.6.1. As outlined in chapter 1, oxygen in molten fluoride either as an impurity or an accidental ingress will lead to the formation of surface films which may or may not be protective in fluoride environment. Compatibility studies between the structural alloys such as GH3535 alloy [135], stainless steel 316 [136], Hastelloy N [137] with molten fluoride salt are mainly addressed to the issue of Cr dissolution in fluoride melt [38, 135-136]. However, no detailed study has been carried out on the surface films formed.

Present study is carried out with the objective of identifying the surface film formed on Ni-based alloys with varying Cr contents when exposed to oxygen containing fluoride melt and the possible role of different films in enhancing or prohibiting the migration of various elements from alloy to melt, and vice-versa. Such a study is important since alloys with different Cr contents will form different surface films which can have different stability towards fluoride attack.

5.2 Microstructural characterization of unexposed alloy coupons

The Ni-based alloys used in the present study are Alloy 690, Alloy 693, commonly used in melter pots in nuclear waste vitrification plants [138-139] as well as the Ni-Mo-Cr alloy. The standard compositions of these alloys are presented in Table 5.1.

Table 5.1: **Elemental composition of Alloy 690, Alloy 693 and Ni-Mo-Cr alloy used in the present study.**

Alloy/Wt.%	Ni	Cr	Mo	Fe	Al	Others
Ni-Mo-Cr alloy	77	7	16			
Alloy 693	Balance	29.2	-	3.96	3.19	Nb: 1.86 Ti: 0.42
Alloy 690	Balance	30.8	-	10.3	<0.50	Cu +Mn< 1.0

Microstructural examination of coupons of the Ni-Mo-Cr alloy (solution annealed at 1450 K for 2 h and WQ) shows that the alloy matrix is devoid of any precipitates containing only equiaxed grains (Fig. 5.1(a)). This observation is consistent with the composition of the alloys studied and the fact that the laboratory melted Ni-Mo-Cr alloy contains a much lower carbon level. The microstructures of alloys 693 and 690 have revealed a distribution of precipitates in the matrix of equiaxed grains of the fcc matrix. EDS analyses of these precipitates have identified these precipitates to be carbides of type $Cr_{23}C_6$ (in both Alloy 690 and Alloy 693) and aluminides of Ni_3Al type (in Alloy 693) (Fig. 5.1). In addition, Alloy 693 showed formation of isolated blocky precipitates of NbC while Alloy 690 contained randomly distributed isolated precipitates of Ti(C, N). Detailed microstructural aspects of Alloy 693 and Alloy 690 are summarized by Halder *et al.* [138] and Dutta *et al.* [139].

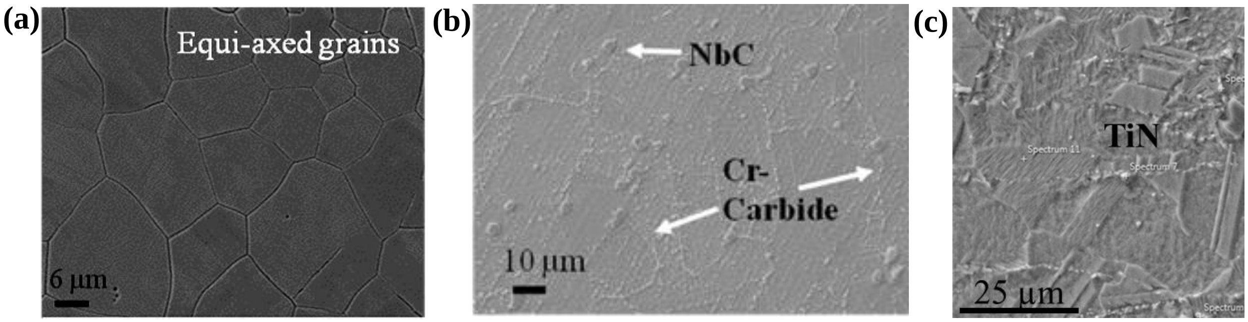

Fig. 5.1: As received microstructure of (a) Ni-Mo-Cr alloy (solution annealed at 1450 K for 1 h and WQ), (b) Alloy 693 in mill-annealed condition and (c) Alloy 690 in mill annealed condition.

5.3 Microstructural studies on alloy coupons after exposure to molten salt environment

After exposure to FLiNaK melt at 973 K for 3 h in ambient atmosphere, patches of reaction products (oxide layer were formed on alloy surfaces. It has been noticed that the areas from where the reaction layer were spalled off are those on which extensive local corrosion attack has taken place. The presence of pits and grain boundary attack in these areas are evidences of such localized corrosion. Micro-analyses of the pits and affected grain boundaries of different alloys are carried out in depth by EDS and the surface film is characterized by XPS. The observations are discussed in detail as follows.

5.3.1 Ni-Mo-Cr alloy

The Ni-Mo-Cr alloy, after exposure to FLiNaK melt developed an inhomogeneous microstructure with a patchy oxide layer on the surface having a non-uniform coverage. The alloy surface devoid of oxide patch showed grain boundary attack and extensive pit formation within the grains (Fig. 5.2). This pitted microstructure results from the selective dissolution of Cr into melt which is consistent with the previous observations made on Hastelloy B3, N etc. [133-137].

This selective depletion of Cr from various alloys under fluoride attack is attributable to negative Gibbs free energy of formation of Cr-fluoride (-160 Kcal/mol F_2) [133]. The formation of pits is mainly attributed to the coalescence of vacancies generated by outward diffusion of Cr through lattice diffusion [69, 140]. The grain boundary is rich in Cr and oxygen which show formation of Cr-rich oxide at the grain boundary.

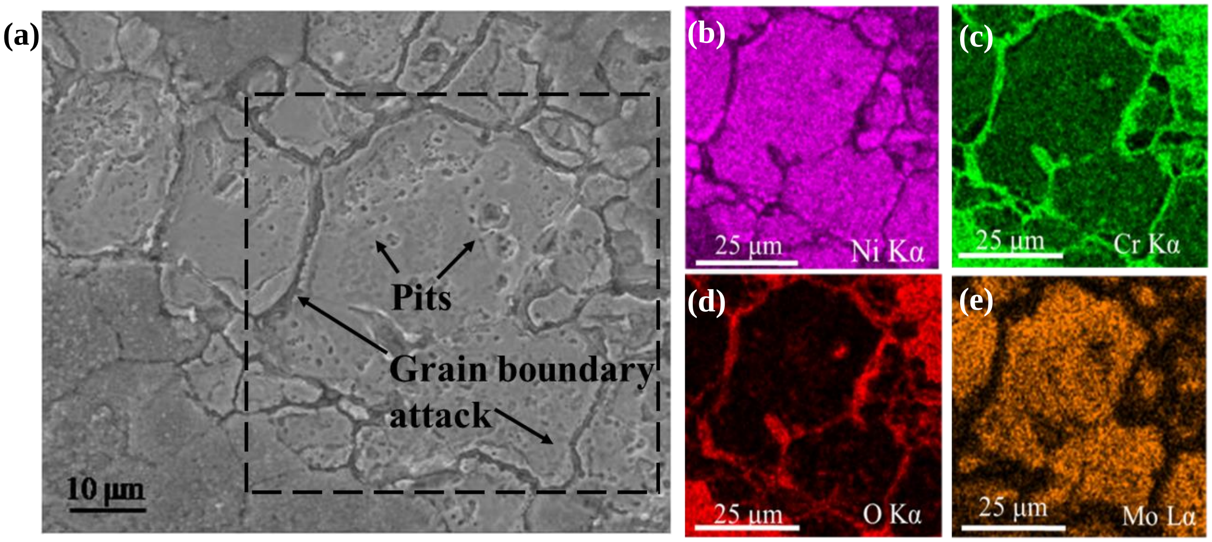

Fig. 5.2: (a) Microstructure of exposed surface of Ni-Mo-Cr alloy showing formation of pits within grain along with the X-ray maps for (b) Ni K_{α}, (c) Cr K_{α}, (d) OK_{α} and (e) Mo L_{α}, showing Cr and O enrichment along grain boundary.

Microstructural analyses of the alloy cross-section after exposure show that an oxide layer rich in Ni and Cr (~3 µm) is formed at the surface (Fig. 5.3(a)-(b)). Below the surface oxide layer, a pitted microstructure depleted in Cr is observed (~6 µm) (Fig. 5.3 (a)-(b)) which was followed by a modified region of the alloy comprising Mo-rich precipitates (Fig. 5.3(c)). EDS analyses identify these precipitates to be Mo_2C type carbides (Fig. 5(d)) which are thermodynamically favoured at this temperature as they have a negative value of Gibbs free energy ~ -54.55 KJ/mol [141-142].

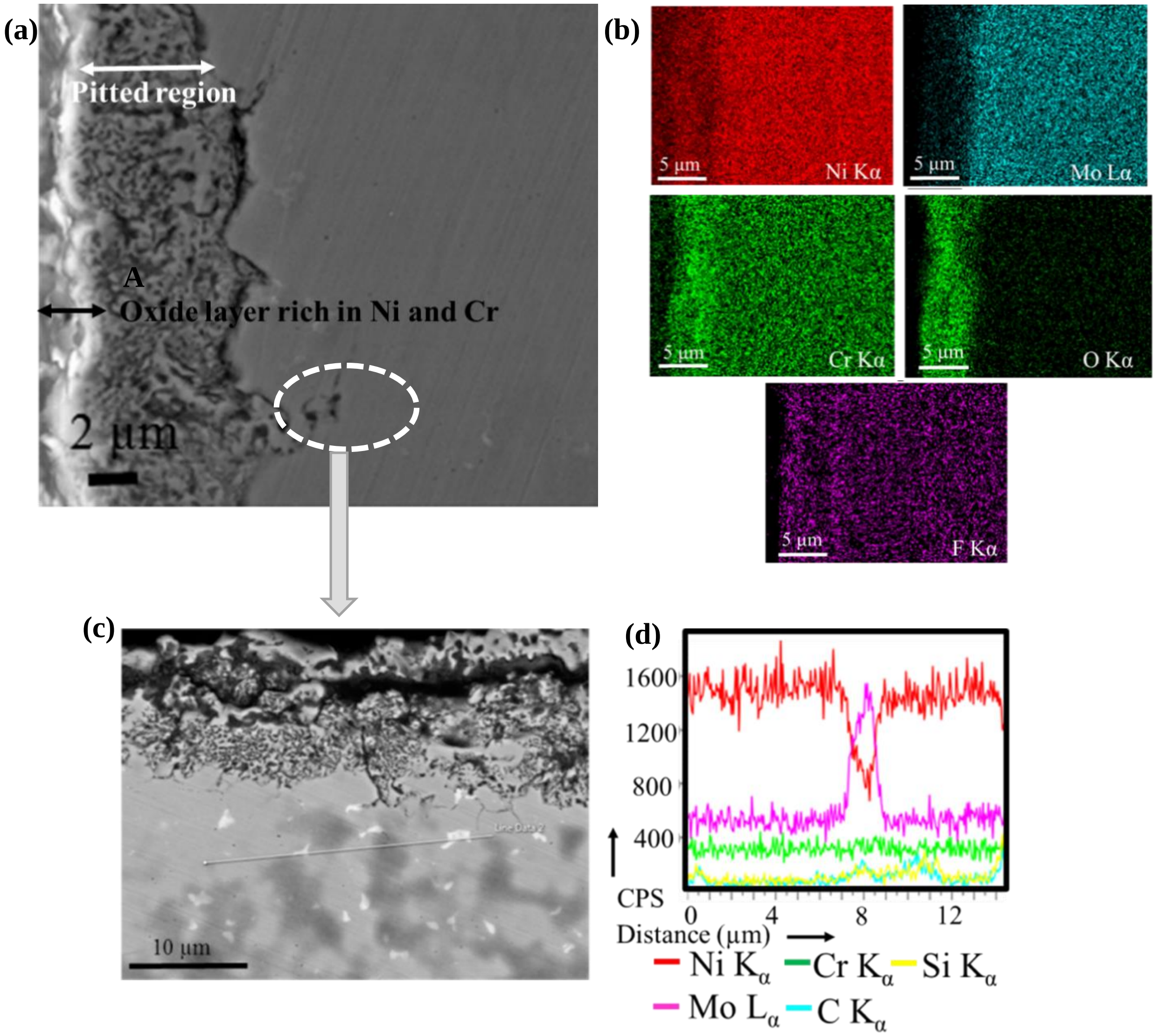

Fig. 5.3: (a) SE image along the alloy cross section, (b) X-ray maps of Ni Kα, Mo Lα, Cr Kα, O Kα and F Kα showing formation of Ni and Cr rich oxide at surface in Ni-Mo-Cr alloy, (c) BSE image and (d) EDS line scan of the alloy cross-section after exposure to molten FLiNaK salt showing formation of Mo-rich carbides.

XRD analysis of the post-corroded alloy reveals that a mixed oxide of type NiO and Cr_2O_3 is developed at the surface in concordance with the SEM-EDS results (Fig. 5.4).

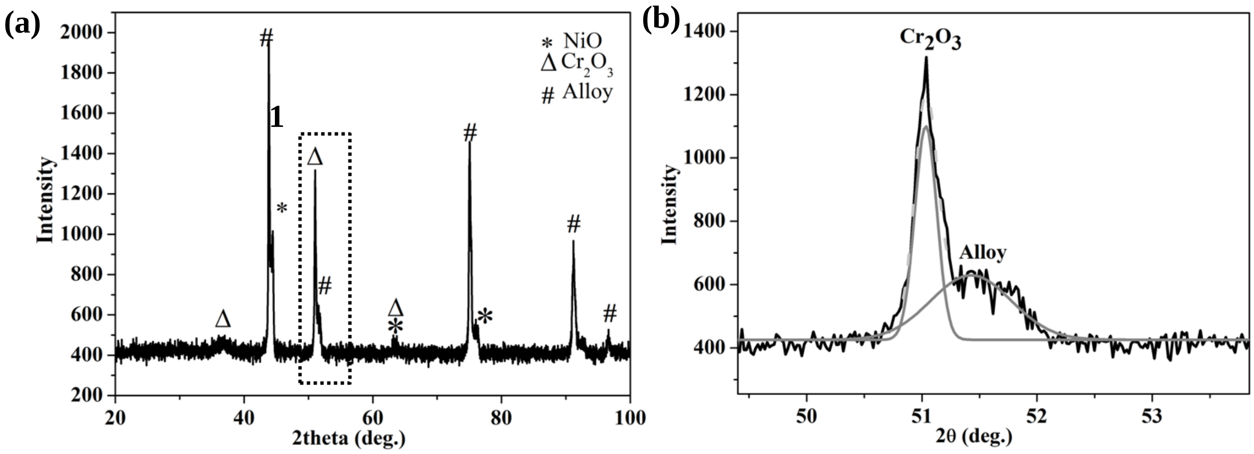

Fig. 5.4: (a) XRD pattern recorded for the exposed Ni-Mo-Cr alloy, (b) shows the de-convoluted peaks corresponding to region marked as "1" in (a).

5.3.2 Alloy 693

Alloy 693, after exposure to FLiNaK melt formed a patchy black surface layer. Detailed examination of the alloy surface and cross-section containing the surface layer (Fig. 5.5) by SE imaging and elemental X-ray maps reveal that the surface layer formed is rich in O, Cr and Al (~2 μm). The Al rich type surface oxide developed over the grain matrix, but remained depleted in grain boundaries. This suggests that the grain boundary diffusion mechanism is responsible for dissolution of Al into the melt in case of Alloy 693.

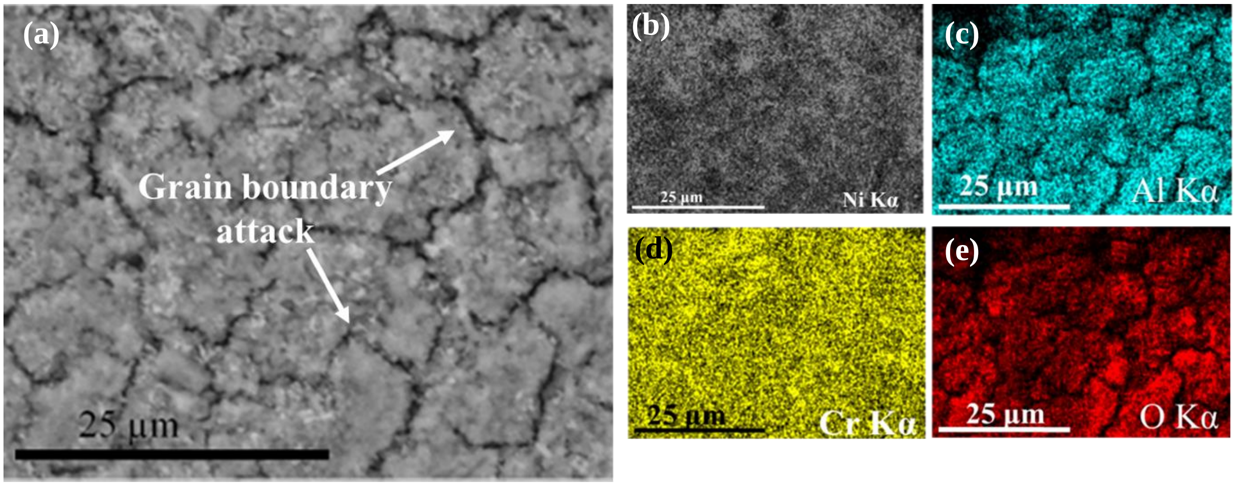

Fig. 5.5: (a) SE image of exposed alloy surface and the corresponding elemental X-ray maps for (b) Ni K_α (c) Al K_α (d) Cr K_α (e) O K_α.

Beneath the oxide layer, an Al and F enriched layer (width ~2 μm) followed by a Cr depleted and F enriched region (~ 8 μm width) containing pits was observed (Fig. 5.6). Both the Cr depletion and subsequent pit formation are attributable to selective removal of Cr from the alloy and consequent coalescence of vacancies to form voids/pitted structure [69, 133].

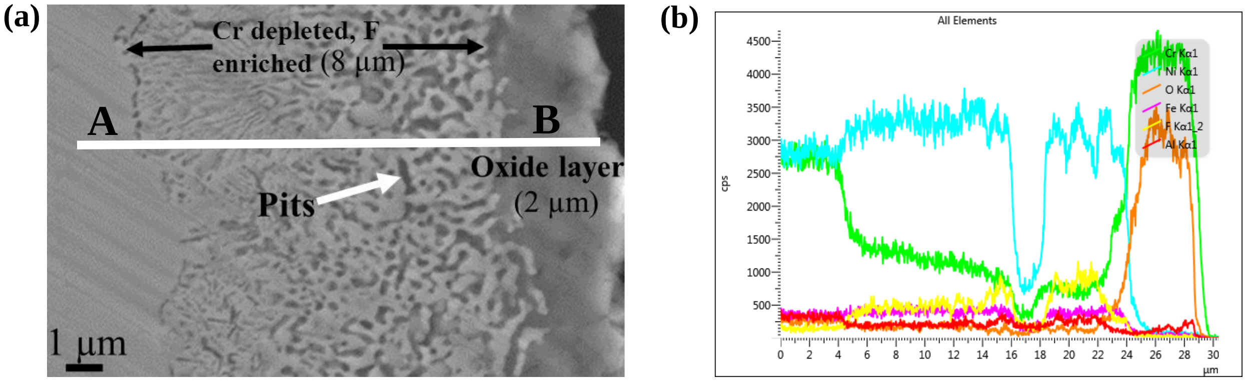

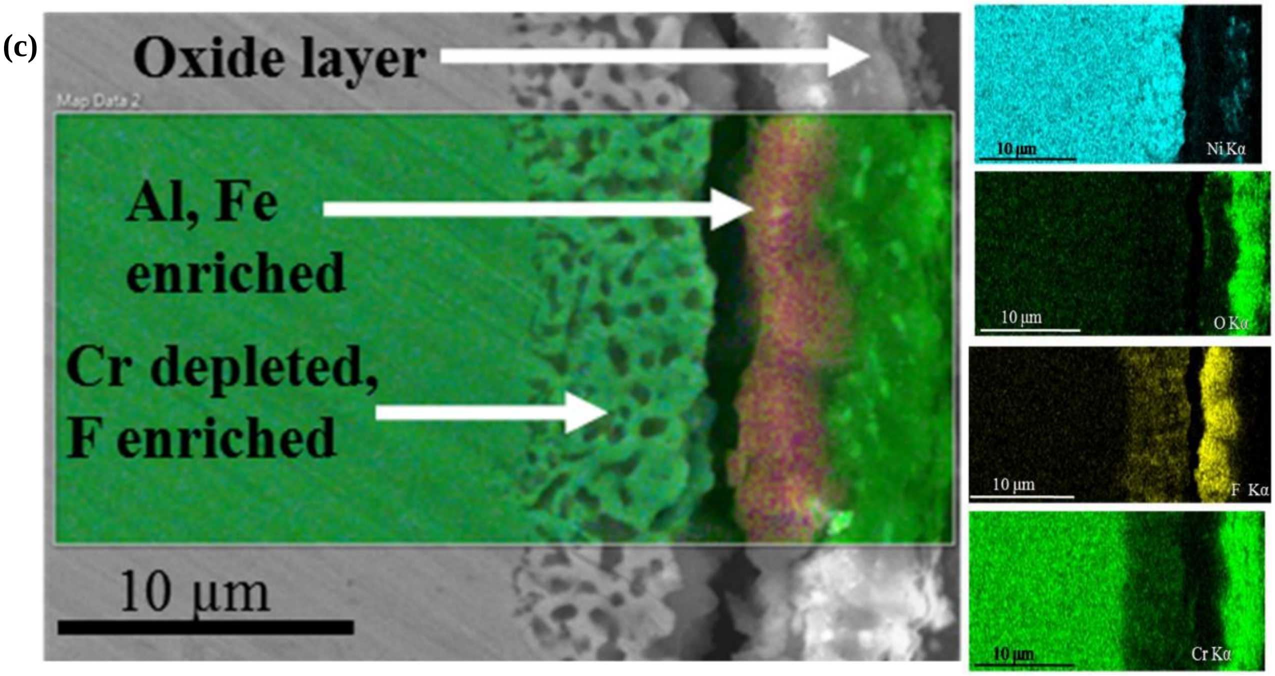

Fig. 5.6: (a) Cross sectional SE image, (b) EDS line scan along the line marked as "AB" in (a), and (c) SE image of the alloy cross-section along with the corresponding elemental X-ray maps (Ni Kα, O Kα, F Kα and Cr Kα) of exposed coupon of Alloy 693.

XRD analysis confirms that the surface layer is predominantly Cr_2O_3 and Al_2O_3 type consistent with the SEM observations (Fig. 5.7).

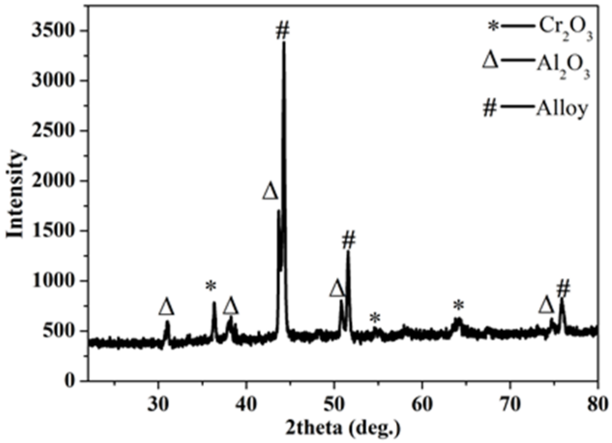

Fig. 5.7: XRD pattern for exposed Alloy 693 coupon.

5.3.3 Alloy 690

Alloy 690 after exposure, showed microstructural features similar to those obtained for Ni-Mo-Cr and Alloy 693. A Cr-rich oxide layer is formed over the surface with incomplete coverage and the surface devoid of oxide layer showed grain boundary attack and a pitted grain interior, both attributable to Cr dissolution (Fig. 5.8 (a)-(b)). Detailed EDS analyses and X-ray maps for the alloy cross-section reveal formation of Cr-oxide (~4 µm) at surface followed by a pitted region depleted in Cr and enriched in F (~12 µm width) (Fig. 5.8(c)). XRD measurements confirm that the oxide layer formed on Alloy 690 after exposure to FLiNaK salt is mainly Cr_2O_3 and NiO type (Fig. 5.8(d)).

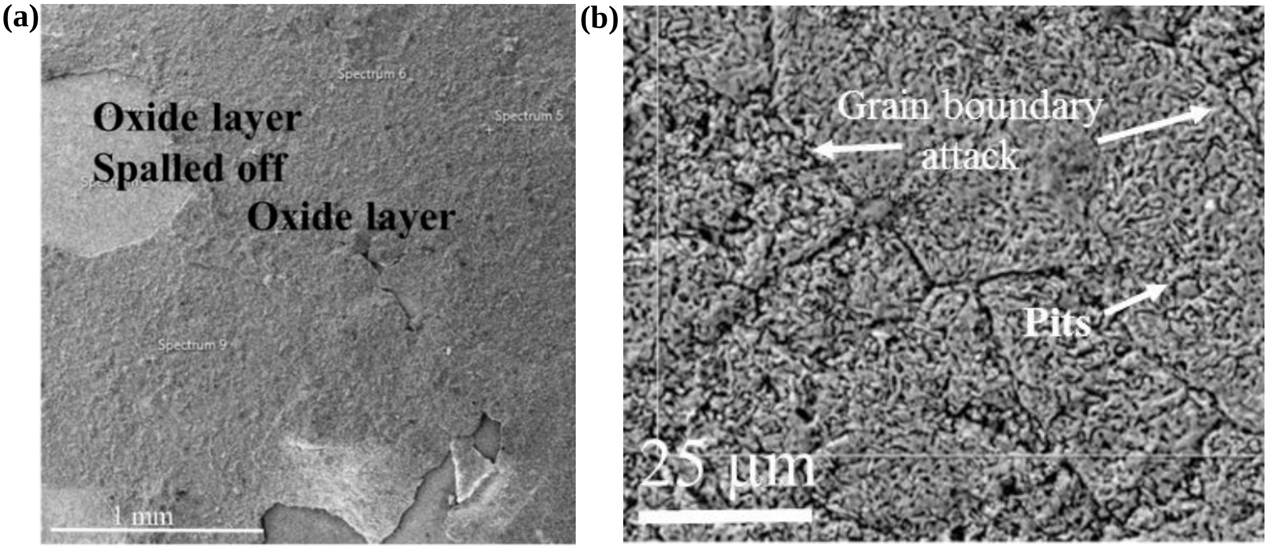

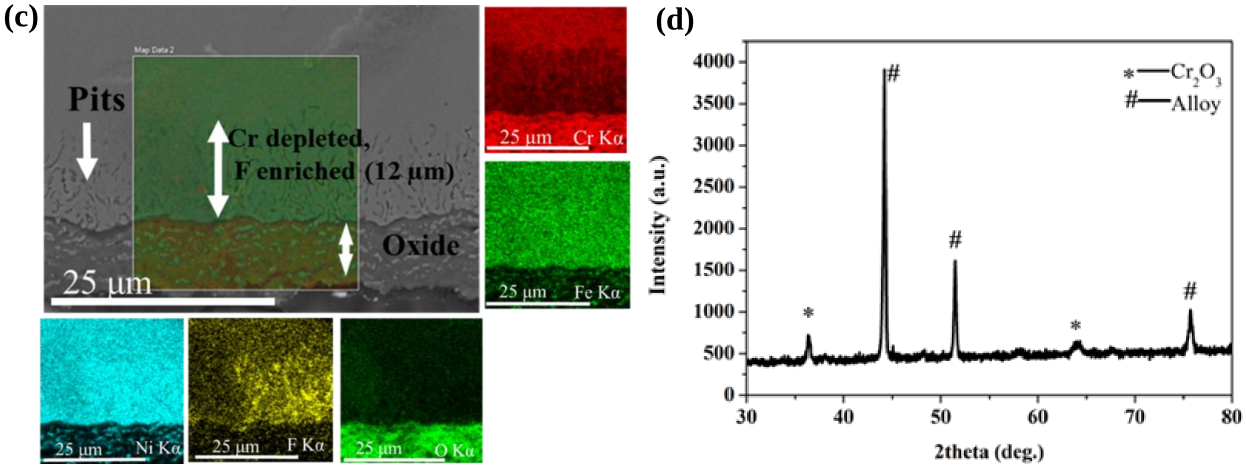

Fig. 5.8: (a) Surface morphology, (b) SE image of the alloy region devoid of oxide layer (c) Cross-sectional microstructure and X-ray maps of different elements and (d) XRD pattern of Alloy 690 after exposure to FLiNaK melt.

It is thus evident from the microstructural characterization that all the three alloys undergo intergranular attack and pit formation due to selective dissolution of Cr. The depth of Cr depletion is observed to follow the trend Ni-Mo-Cr alloy< Alloy 693<Alloy 690. Similarly, elemental quantification of the exposed FLiNaK salt show that Cr concentration is highest for the salt interacted with Alloy 690 while lowest in the salt interacted with Ni-Mo-Cr alloy (Table 5.2).

Table 5.2: Quantitative elemental analysis of the alloying elements present in the FLiNaK salt before and after interaction with Ni-based alloys.

Molten salt	**Al (%)**	**Cr (ppm)**	**Fe (%)**	**Mo (ppm)**	**Ni (ppm)**
LiF-NaF-KF mixture	-	47	0.10	8	<5
Salt-reacted with alloy 690	4.97	72	0.24	57	<5
Salt-reacted with alloy 693	3.37	67	67ppm	6	<5
Salt-reacted with alloy Ni-Mo-Cr	3.14	40	0.13	56	<5

5.4 XPS study of the exposed alloys

5.4.1 Ni-Mo-Cr alloy

The XPS measurements were carried out on an area of the alloy where no oxide layer was observed. The survey spectrum and the subsequent high energy resolution scans reveal that Ni is present in Ni^o and Ni^{2+} state having $2p_{3/2}$ peak binding energies at 852.5 eV and 858.5 eV, respectively (Fig. 5.9 (a)-(b)) [143-144]. For molybdenum, binding energy (BE) peaks corresponding to $3d_{5/2}$ and $3d_{3/2}$ were observed at 232.0 eV and 235.1 eV, respectively (Fig. 5.9 (c)) which correspond to Mo in +6 oxidation state [143-144] (Table 5.3). O 1s peak was deconvoluted to two peaks at BE values 528.3 eV and 529.9 eV indicating its presence in the form of oxides of nickel (NiO) and molybdenum (MoO_3) ((Fig. 5.9 (d)). Semi-quantitative analyses using CASA XPS indicate that contribution to O 1s peak from MoO_3 is higher (69.54%) as compared to that from NiO (30.46%). Presence of metallic state of Ni and Cr along with MoO_3 and NiO suggest that these oxides are either porous or discontinuous exposing metallic islands at places (Fig. 5.9(e)).

Table 5.3: Result of XPS analysis for the oxide scale formed on exposed alloy Ni-Mo-Cr alloy. The peaks are obtained with an energy resolution of 0.5 eV.

Spectrum	Peak position (eV)	Chemical state	FWHM (eV)
Ni $2p_{3/2}$	852.6	Ni^o	3.4
	858.5	Ni^{2+}	4.4
Mo $3d_{5/2}$	232.03	Mo^{6+}	1.3
Mo $3d_{3/2}$	235.15	Mo^{6+}	1.7
O 1s	528.3	O^{2-} (from Ni oxide)	1.6
	530.0	O^{2-} (from Mo oxide)	2.2

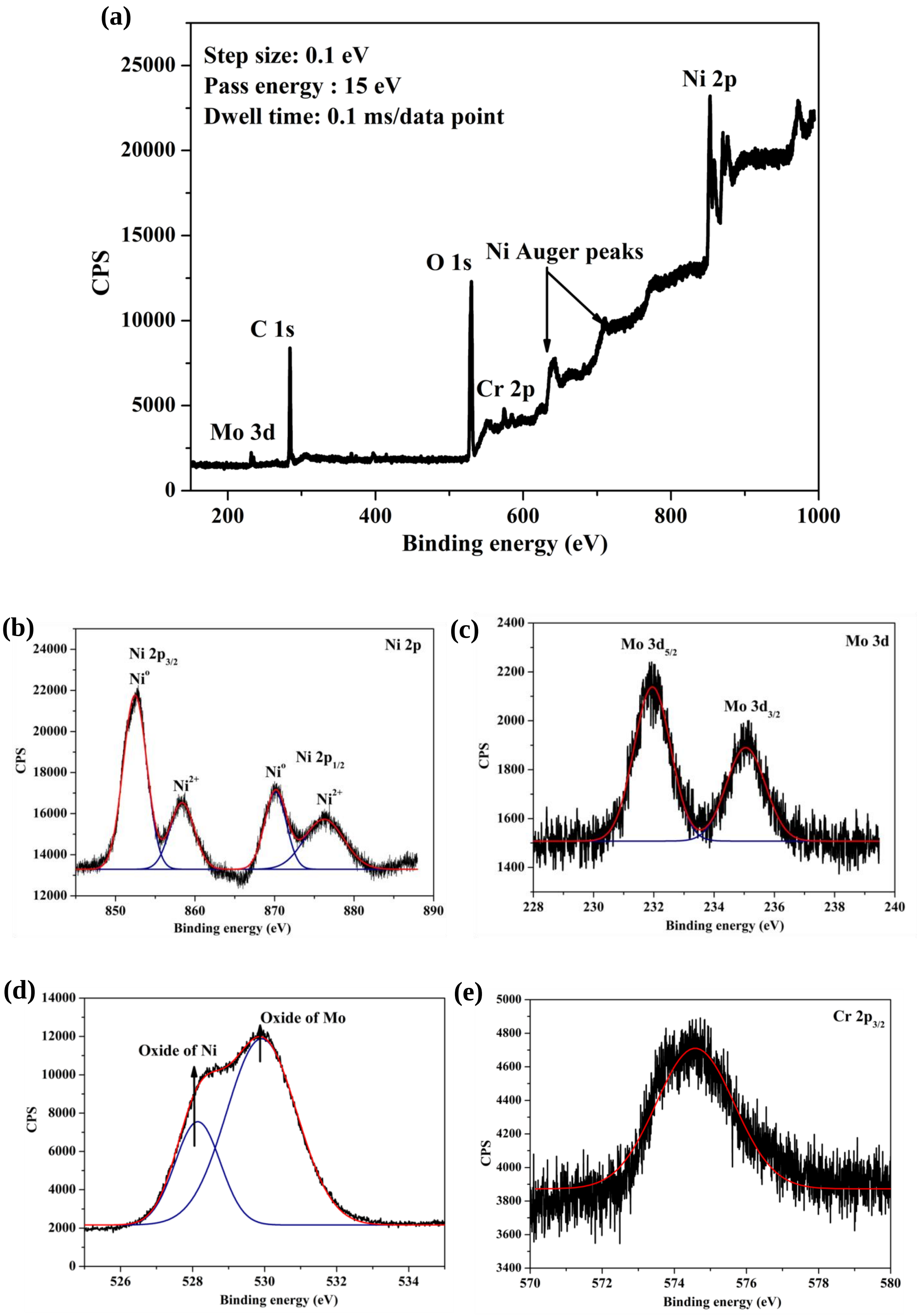

Fig. 5.9: (a) Survey scan and (b)-(e) High resolution XPS spectra for Ni 2p, Mo 3d, O 1s and Cr $2p_{3/2}$ peaks, respectively, corresponding to Ni-Mo-Cr alloy surface exposed to FLiNaK salt.

5.4.2 Alloy 693

XPS measurements on the exposed alloy surface devoid of oxide patches (as observed by SEM) revealed that Ni, Cr, Fe and Al were present in their metallic states. On the other hand, the XPS analyses of the oxide patch (Fig. 5.10) indicate that Ni and Al are mainly in their +2 and +3 states, respectively (Table 5.4). The O 1s binding energy peak on deconvolution shows peak positions at 528.4 eV (corresponding to oxide of Ni) and 530.4 eV (corresponding to oxide of Al) indicating that the surface film comprises oxides of Ni and Al mainly Al_2O_3 and NiO [145]. Furthermore, contribution to O 1s peak from the oxygen in Al_2O_3 is higher (73%) as compared to the O from NiO (17%). Formation of surface layer of Al_2O_3 in Alloy 693 is also observed when the alloy is subjected to high temperature borosilicate melt [131] or oxidizing environment [146] for providing diffusion barrier coating. No iron was identified in the surface layer.

Table 5.4: Result of XPS analysis for the oxide scale formed on exposed Alloy 693. The peaks are obtained with an energy resolution of 0.5 eV.

Spectra	Peak position (eV)	Chemical state	FWHM
Ni $2p_{3/2}$	853.6	Ni^o	2.51
	859.0	Ni^{2+}	4.45
Cr $2p_{3/2}$	574.7	Cr^o	2.53
Al $2p_{3/2}$	74.8	Al^{3+}	2.32
O 1s	528.4	O^{2-} (from Ni oxide)	1.31
	530.4	O^{2-} (from Al oxide)	2.34

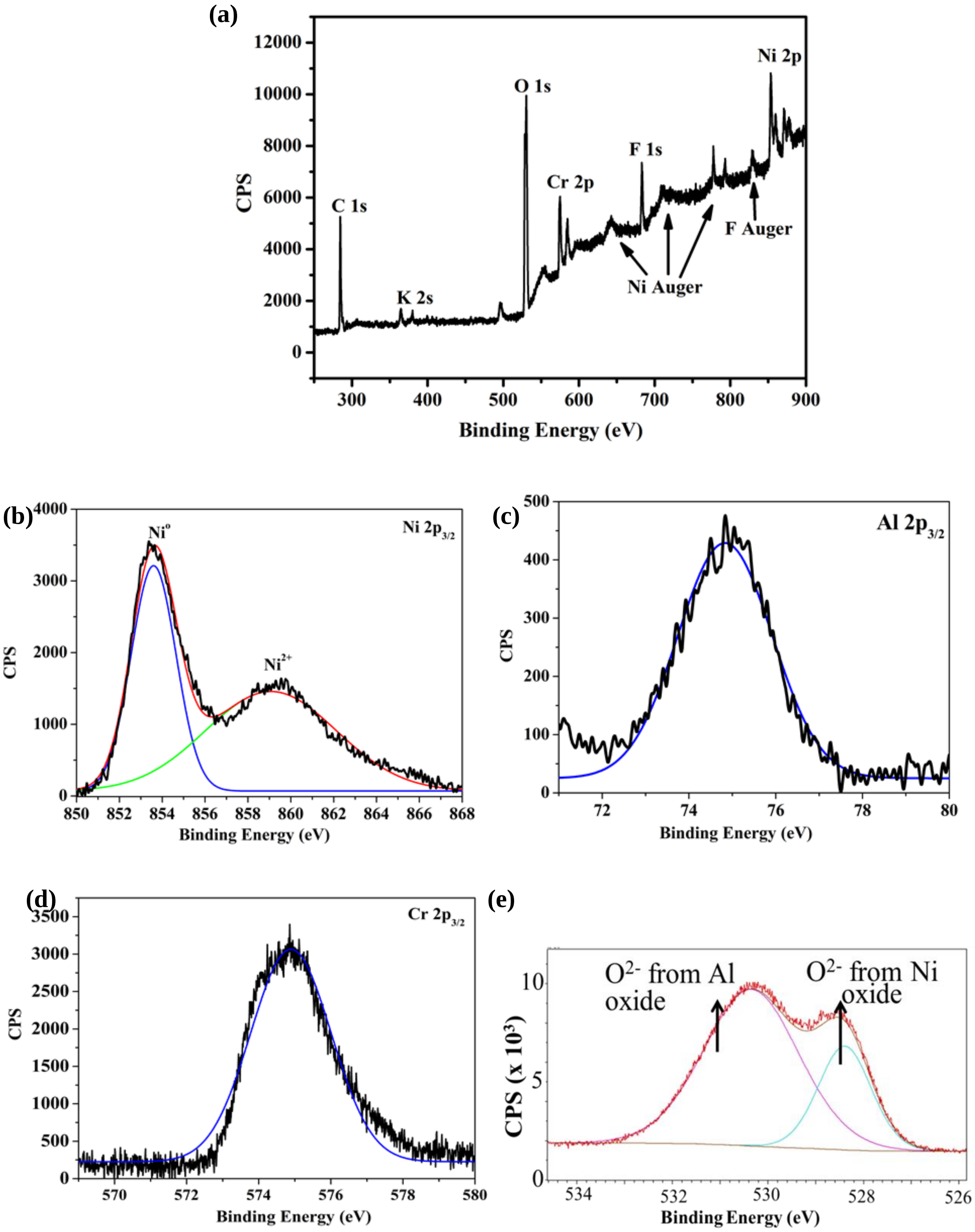

Fig. 5.10: (a) Survey spectrum and high resolution XPS spectra for (b) Ni $2p_{3/2}$, (c) Al $2p_{3/2}$, (d) Cr $2p_{3/2}$ and (e) O 1s for exposed Alloy 693 surface.

5.4.3 Alloy 690

XPS measurements on the oxide patch developed on the alloy indicate Cr is present in both Cr^{3+} and Cr^{o} states (Table 5.5). Ni is also observed to be in +2 state as well as the elemental state with its $2p_{3/2}$ peaks occurring, respectively, at 858.8 eV and 853.2 eV [143]. The deconvoluted O 1s binding energy peaks occur at a 528.0 eV (corresponding to oxide of Ni) and 530.0 eV (corresponding to oxide of Cr) indicating that the surface film comprises oxides of Ni and Cr mainly of type Cr_2O_3 and NiO [143-145].

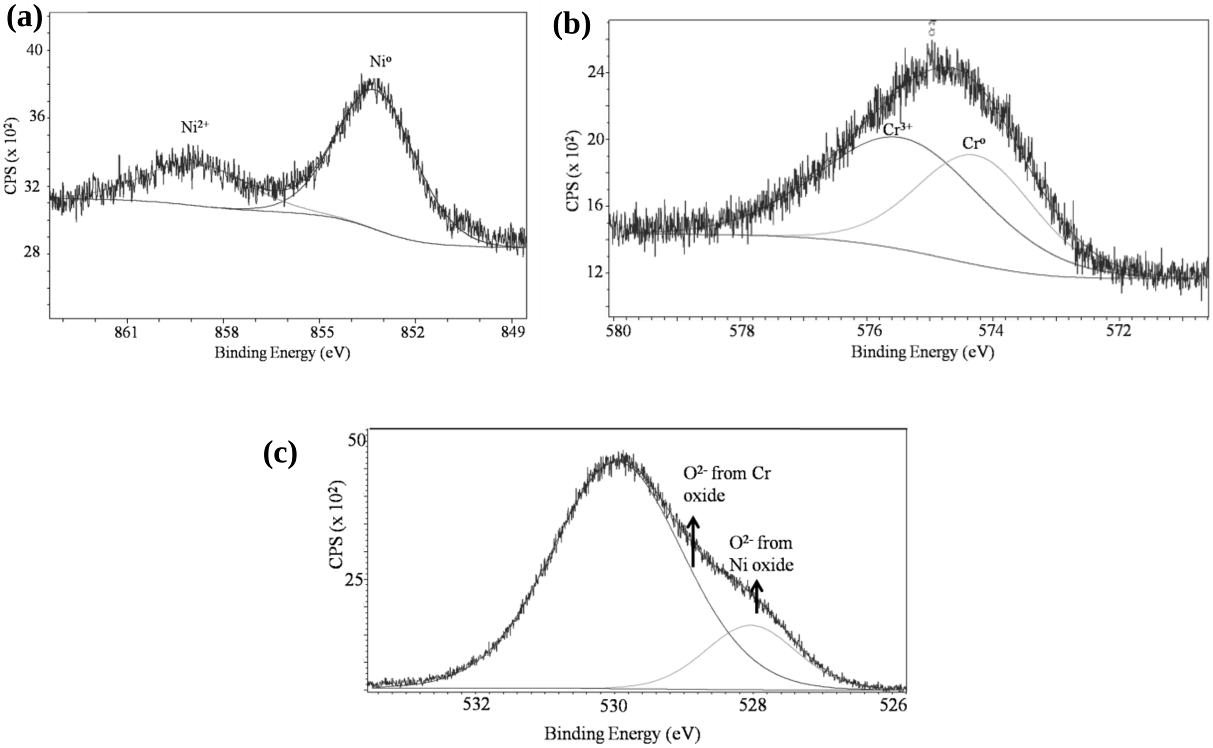

Fig. 5.11: High resolution XPS spectra for (a) Ni 2p3/2, (b) Cr 2p3/2 and (c) O 1s for exposed Alloy 690 surface.

Furthermore, from the area percentage of the deconvoluted O peaks, it is evident that contribution to O 1s peak from the oxygen in Cr_2O_3 is higher (83.6%) as compared to the O from NiO (16.4%). No iron was identified in the surface layer. Presence of metallic state of Ni and Cr suggest that these oxides are either porous or discontinuous exposing metallic islands at places.

Table 5.5: Result of XPS analysis for the oxide scale formed on exposed 690.

Spectra	Peak position (eV)	Chemical state	FWHM
Ni $2p_{3/2}$	853.2	Ni^o	2.89
	858.8	Ni^{2+}	3.81
Cr $2p_{3/2}$	574.3	Cr^o	2.2
	575.5	Cr^{3+}	3.0
O 1s	528.0	O^{2-} (from Ni oxide)	1.54
	529.9	O^{2-} (from Cr oxide)	2.23

5.5 Discussion of Results

5.5.1 Effect of Cr concentration in alloy on the surface films characteristics

The Ni-based alloys developed mixed oxide scales on the surface, *viz.*, NiO and Cr_2O_3 for Alloy 690, NiO + Al_2O_3+ Cr_2O_3 for Alloy 693 and MoO_3 + NiO + Cr_2O_3 for Ni-Mo-Cr alloy after interaction with the molten fluoride salt (Table 5.6). These oxide scales do not form fully on the alloy surfaces due to fluxing of molten fluoride as well as competitive diffusion of fluorine. Such partially protective oxide scales of Cr are also observed when Ni based alloys are exposed to molten sulphates in contrast with exposure to nitrate and nitride media where the oxide scales formed remain passive [131,143].

Cr_2O_3 and Al_2O_3 are known to provide passivity to the alloy at high temperature and the diffusivity of various elements such as Ni, Cr, Fe is reported to have magnitudes four order lower in these oxides than in pure Ni [131]. Though Al_2O_3 and Cr_2O_3 are very stable under high temperature corrosive environments as compared to NiO and MoO_3, they offer very little resistance to selective dealloying of Cr and Al in present case. Both Alloy 690 and 693 show internal penetration of F beneath the oxide layers. This results from a competitive diffusion of F and O in the alloys. The activation energy required for diffusion is 118.6 KJ/mol for fluorine while it is 182.0 KJ/mol for O in pure nickel. The diffusion coefficient at 973 K for F in pure Ni is ~4.03 x 10^{-9} cm^2/s [142] as compared to O diffusivity which is ~0.94 x 10^{-9} cm^2/s [147]. Hence fluorine forms corrosion products rich in Al and Cr. In case of Ni-Mo-Cr alloy, the surface layer is mainly NiO and MoO_3 type, but enrichment of F beneath the oxide layer is not appreciable indicating the resistance of Mo against fluoride attack.

Table 5.6: Oxide layers formed on Ni-based alloys as identified by XRD and XPS.

Alloy	XRD	XPS	Possible configuration
Alloy 690	Cr_2O_3	NiO, Cr_2O_3	NiO Cr_2O_3 Alloy
Alloy 693	Al_2O_3, Cr_2O_3	NiO, Al_2O_3	NiO Al_2O_3 Cr_2O_3 Alloy
Alloy Ni-Mo-Cr	NiO, Cr_2O_3	NiO, MoO_3	MoO_3 NiO Cr_2O_3 Alloy

5.5.2 Mechanism of interaction

To quantify the susceptibility of the alloys to molten salt corrosion, a corrosion susceptibility index (CSI) expressed by the following equation was used [148],

$$CSI = \frac{= XAl + XCr + XTi + XNb + XHf + XTa}{XNi + XFe + XCo + XMn + XMo + XW + XRe + XRu} \qquad 5.1$$

where *X* refer to molar fraction of elements present in the alloy. An alloy with lower CSI should possess better corrosion resistance in molten salts. The CSI was found to be highest for alloy 693 (0.58) followed by Alloy 690 (0.47) and Ni-Mo-Cr alloy (0.19). However, the depth of Cr depletion was more in case of Alloy 690 as compared (~12 µm) to Alloy 693 (~8 µm). Similar observations with CSI were made in case of Ni cladded GH3535 alloy where the cladding bottom layer showed severe corrosion in-spite of having a CSI of 0.06, while GH3535 alloy had a CSI value of 0.09, but showed relatively less corrosion [148]. Thus instead of CSI, one should consider

W_{Fe+Cr} (wt%) to assess the corrosion susceptibility of the alloys [142] which is a measure of corrosion resistance *i.e.*, lower the value of W, lower is the susceptibility of the alloy to corrosive attack. W_{Fe+Cr} (wt%) was found to show the trend $W_{Fe+Cr}^{Ni-Mo-Cr}(7\ wt\%) < W_{Fe+Cr}^{693}(33\%) < W_{Fe+Cr}^{690}(38\%)$ in consistency with the observed trend in Cr depletion. The depth of fluorine attack was in the order as follows: Ni-Mo-Cr alloy (~ 6 µm) < Alloy 693 (~8 µm) < Alloy 690 (~12 µm) indicating the resistance of Mo against fluoride attack.

From the microstructural and spectroscopic analyses of the alloys, a reaction mechanism is proposed for the alloy corrosion. In absence of oxygen, the corrosion occurs via dissolution of alloy elements into salt and penetration of F. The electrochemical corrosion reaction between alloy and molten salt [68,143,149] is as follows:

$$\mathrm{F} + 2e^- \Rightarrow \quad F^{2-} \qquad 5.2$$

$$\mathrm{Cr} \Rightarrow \quad Cr^{3+} + 2e^- \qquad 5.3$$

However, in presence of oxygen both F and O diffuse into the alloy with F having slightly higher diffusivity as compared to O. Hence both oxygen and fluorine (from molten salt, HF) penetrate the alloy surface resulting in the formation of oxide patches along with the formation of fluorides. From the comparison of Gibbs free energy for fluoride formation of Ni, Al, Cr and Mo, it is observed that Cr can easily form fluorides. These Cr rich fluorides formed at the surface dissolve into the molten salt (the solubility of CrF_3 in FLiNaK salt at 700 ^oC is reported to be 0.96 wt% [150]). Thus, dissolution of Cr rich fluorides sets up a concentration gradient of Cr between the alloy matrix and surface resulting in an alternate path way for faster Cr diffusion. Similar mechanism was proposed for depletion of Cr in $Cr_{23}C_6$ type carbides at high angle boundaries by Dai *et. al* [142].

The diffusivity of Cr in all the three alloys in presence of FLiNaK salt, is estimated from the Cr depletion depth (from SEM) using relation [142]

$$x = (2D_{eff}t)^{1/2} \tag{5.4}$$

where x is the depth of Cr depletion known as characteristic diffusion distance, D_{eff} is the diffusion coefficient and t is the exposure time.

The calculated diffusion coefficients for Cr are observed to follow the trend $D_{690} > D_{693} > D_{Ni\text{-}Mo\text{-}Cr}$ (Table 5.7). In presence of FLiNaK salt, diffusivity of Cr is increased at least by two orders as compared to diffusion of Cr in pure Ni ($D_{Cr/Ni}$) without salt [151]. On the other hand, the diffusivity of Cr^{2+} ion in molten salt (D_{Cr2+}/FLiNaK) is reported to be $2.9 \pm 0.8 \times 10^{-10}$ m^2sec^{-1} at 973 K [142-143].

Table 5.7: Estimated diffusion coefficients of Cr in Alloy 690, 693 and Ni-Mo-Cr alloy at 973 K under FLiNaK environment.

Alloy	**D_{eff} (x 10 $^{-15}$ m^2/s)**	**Error in estimation of D_{eff} (x 10 $^{-15}$ m^2/s)**
690	6.67	0.09
693	3.0	0.1
Ni-Mo-Cr alloy	1.67	0.06

The oxide layers formed on the alloy surfaces are ineffective in mitigating the diffusion of Cr. In fact, Cr diffusivity from alloy matrix to surface was found to increase with Cr concentration. The depth of Cr depletion region in the alloys and Cr diffusivity is higher when oxygen is present in molten salt as compared to the case where the salt is free from oxygen [143]. This indicates that Cr diffusivity is increased in the presence of an incomplete oxide layer. The incomplete oxide layer leads to the formation of galvanic micro-cell between oxide layer (more noble) and exposed alloy surface [152]. The exposed surface now becomes more active than the oxide layer and a higher concentration gradient of Cr between alloy matrix and alloy surface is set up as compared to the case where the molten salt is free from oxygen. The mechanism of interaction is depicted schematically in Fig. 5.12.

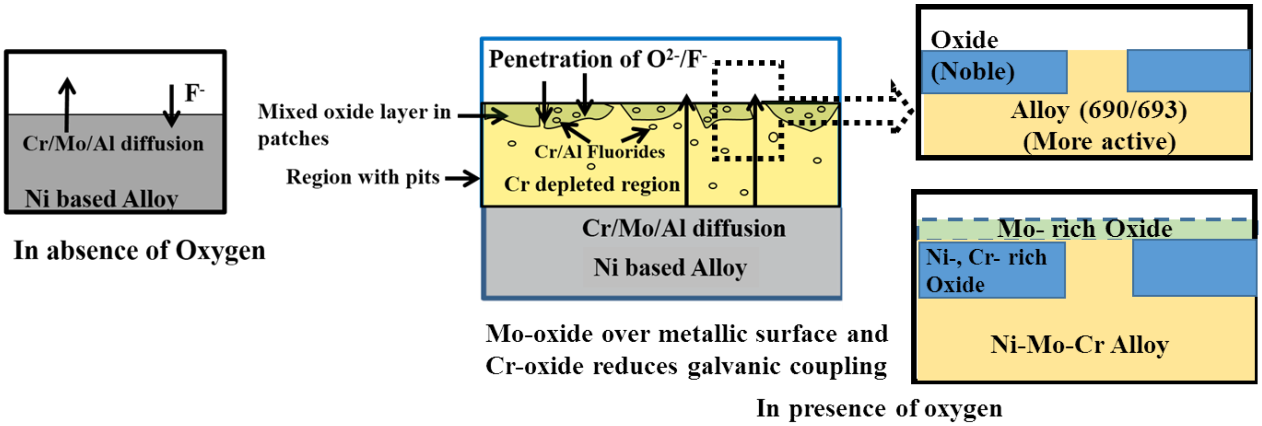

Fig. 5.12: Schematic representation of alloy corrosion in molten salt in (a) absence of oxygen and (b) presence of oxygen.

The lower Cr depletion and Cr diffusivity in case of Ni-Mo-Cr alloy as compared to Alloy 690 and 693 can be attributed to the fact that MoO_3 layer, also formed over the areas devoid of oxide patches, may prevent the formation of galvanic micro-cell between oxide and exposed surface or reduce galvanic coupling between Ni-, Cr-rich oxide and the exposed surface.

In order to predict Cr concentration profile under long term corrosive attack, solution of Fick's second law of diffusion having the following form is used [141]

$$C_{Cr}(d,t) = C_{o,Cr}(d,t)\,erf\left(\frac{d}{2\sqrt{D_{eff}t}}\right) \qquad 5.5$$

where d is the distance from alloy surface (the oxide layer is not considered), D_{eff} is the effective diffusion coefficient of Cr in alloy under FLiNaK environment and t is the exposure time. $C_{Cr}(x,t)$ and $C_{o,Cr}(x,t)$ represent the Cr concentration at distance d from the alloy surface at any time t and at t=0, respectively. Fig. 5.13 shows the simulated Cr depletion profile after 10000 hrs of exposure for the three different alloys used in present study. Alloy 690 shows the highest depth of Cr depletion followed by Alloy 693 and Ni-Mo-Cr alloy. The calculated Cr diffusion profile for Ni-Mo-Cr alloy matches well with the profile for Hastelloy N calculated from the diffusion coefficients reported by Ye *et. al* [68].

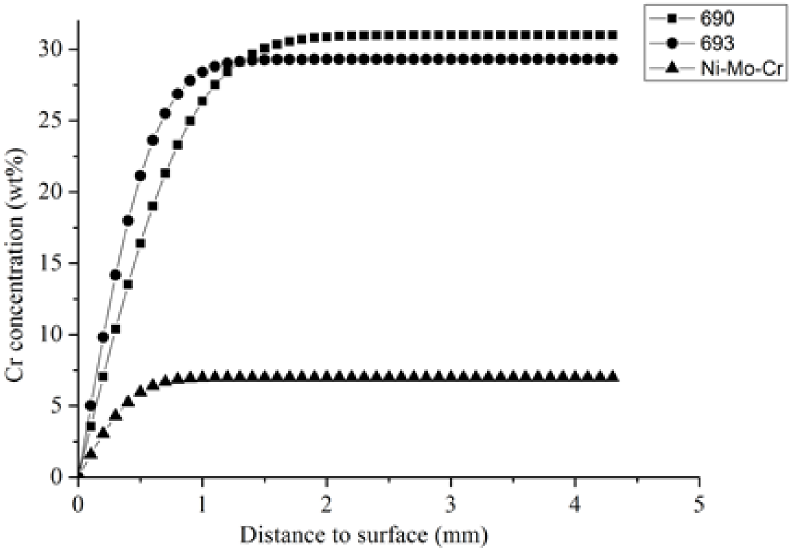

Fig. 5.13: Cr diffusion profile calculated for 10000 h exposure of Ni-Mo-Cr alloy, Alloy 693 and Alloy 690 to FLiNaK salt.

The observations suggest that for use in reactor environments, strict redox control and purification of salt/alloys is needed as diffusivity of elements is enhanced in fluoride melt. The oxide layers developed are partially protective and also do not mitigate the internal penetration of F.

5.6 Summary

Microstructural and surface characterization of Ni-based alloys, *viz.*, Alloy 690, Alloy 693 and Ni-16 wt.% Mo- 7wt.% Cr exposed to molten fluoride salt of FLiNaK at 973 K under atmospheric pressure was carried out with the aim of assessing the efficacy of the protective layers in different alloys against the corrosion attack of the fluoride. Patches of mixed oxide layers of the types: a) NiO +Cr_2O_3, b) NiO + Al_2O_3 +Cr_2O_3 and c) MoO_3 + NiO+Cr_2O_3 were observed for a) Alloy 690, b) Alloy 693 and c) the experimental Ni-Mo-Cr alloy, respectively. The corrosion susceptibility index and the diffusivity of Cr in these alloys followed the order: Alloy 690 > Alloy 693 > Ni-Cr-Mo alloy. The oxide layers developed were found to be patchy resulting in the formation of galvanic micro-couples with exposed areas, the consequent corrosion attack and the dissolution of Cr into the molten salt. The lower Cr depletion in case of Ni-Mo-Cr alloy as compared to Alloy 690 and 693 can be attributed to the fact that MoO_3 layer is also formed over the areas devoid of oxide patches which may prevent/reduce galvanic coupling between Ni-, Cr-rich oxides and exposed surface.

Chapter 6 : Tellurium induced microstructural degradation in Ni-Mo-Cr alloy

6.1 Background

Present study is aimed at investigating the microstructure of Te coated Hastelloy N subjected to annealing treatments at 973-1073 K, to identify the β2 type nickel rich tellurides. Since behaviour of Te in salts containing both fissionable and non-fissionable isotopes is the same and the cracks generated by tellurium attack are not related to the corrosion attack by fluoride melt, laboratory scale experiments, not involving any radioactive substances, can provide accurate insights on the tellurium attack on Ni based alloys [71-74]. In addition, cluster-expansion based formulation in conjunction with first principles calculations on the Ni-Te system has been performed to analyse the phase stabilities of possible nickel tellurides. Based on microstructural and theoretical studies a mechanism for formation of nickel tellurides with preferred crystal structure is proposed.

Table 6.1: Crystallographic data for β2 phase obtained in Ni-Te system [153].

Phase	Formula	Space group	Space group No.	Lattice parameter (Å)			
				a	b	c	β
β2 High Ni side	$Ni_{3+x}Te_2$	$P2_1/m$	11	7.54	3.79	6.09	91.16
β2 High Te side	$Ni_{3-x}Te_2$	Pma2	28	7.54	3.79	6.09	

6.2 Microstructural characterization

6.2.1 Surface Morphology

The microstructure of as received Hastelloy N shows that the alloy is precipitate free, but contains numerous twins (Fig. 6.1(a)). The composition of the alloy measured by XRF is given in Table 6.2.

Table 6.2: Nominal composition of Hastelloy N used in the present study.

Element	Cr	Mo	Fe	Mn	Ni
Concentration (wt. %)	7.2	15.0	3.7	0.5	Balance

The Te-coated alloy specimen reveals a homogeneous coating of Te on the alloy surface (Fig. 6.1(b)). The X-ray diffraction (XRD) pattern shows Bragg peaks for Te indicating that the deposited Te is in crystalline phase (Fig. 6.1(c)) and no intermetallic compound is formed.

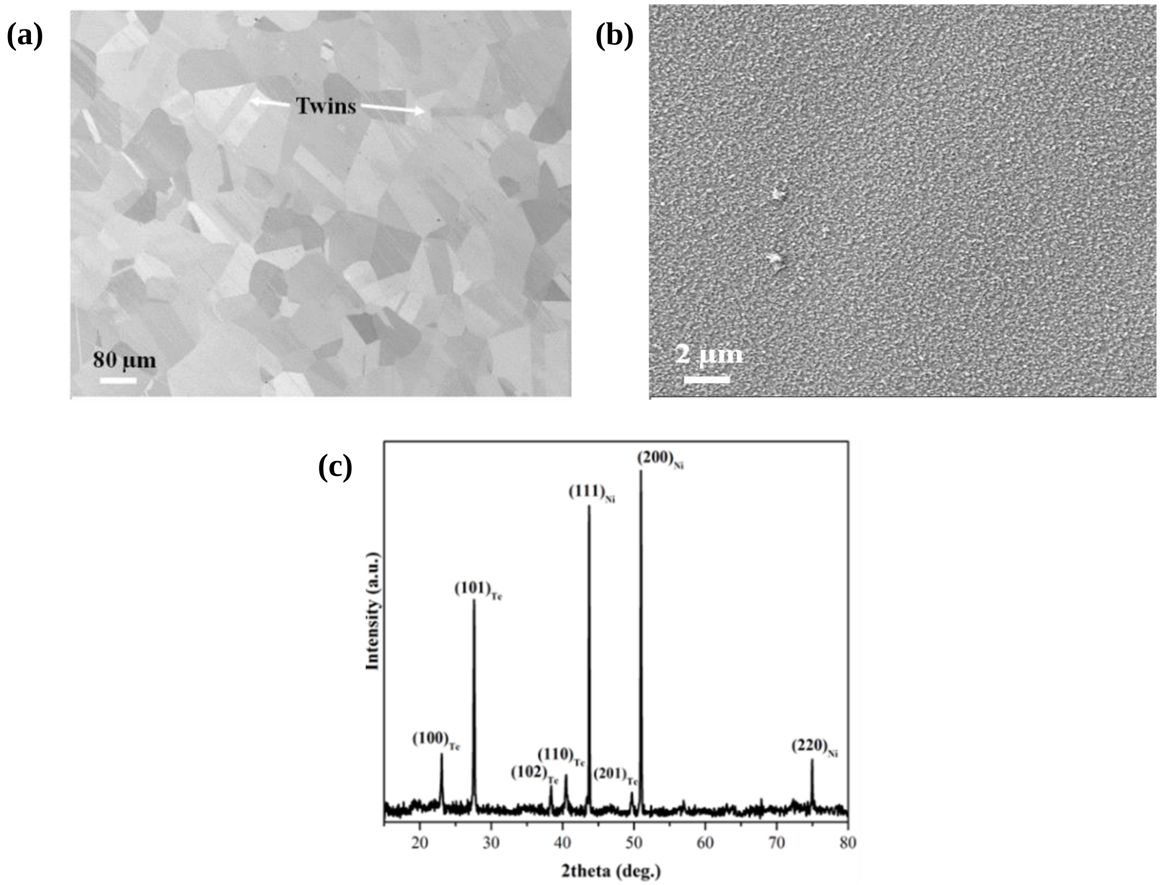

Fig. 6.1: (a) SEM micrograph of as received Hastelloy N, (b) SEM micrograph and (c) XRD pattern for Hastelloy N coated with 10 mg/cm^2 Te.

SEM observations on Te coated alloy samples annealed at 973 K for 96 h followed by water quenching have shown the presence of irregularly shaped inter- and intra-granular precipitates mainly in the size range 1-3 µm (shown in Fig. 6.2(a)) which are identified as tellurium rich precipitates from backscattered electron (BSE) images (Fig. 6.2(b)) and detailed X-ray mapping as shown in Fig. 6.2((c)-(g)). Detailed elemental analysis by EDS indicate that the nominal composition of this precipitate is 58.7 at.% Ni - 35.7 at.% Te - 4.1 at.% Cr - 1.5 at.% Mo while the alloy matrix has a composition 78.2 at.% Ni - 10.9 at.% Mo - 5.3 at.% Cr-5.5 at.% Mo. From the Ni-Te phase diagram [153], it is evident that Te concentration in Ni matrix in the range 36.8 - 43.3 at.% correspond to the beta (β2) nickel telluride Ni_3Te_2 type phase. These Ni_3Te_2 precipitates can have different crystal structures depending on the Te content such as monoclinic structure and orthorhombic structure [72-75], but are extremely difficult to differentiate owing to very close lattice parameters (Table 6.1). Owing to small size of the Te rich precipitates and signals from the surrounding Ni-Mo-Cr alloy matrix [72], it is possible that the Te concentration measured by EDS is slightly under-estimated and hence it is most likely that the Te rich phase formed in present case is Ni_3Te_2 which is the stable telluride formed at this temperature and is reported in several studies [72-75]. The exact stoichiometry, however, could not be confirmed due to small precipitate size and limitations of EDS quantification [73] and hence subsequent TEM investigations were carried out.

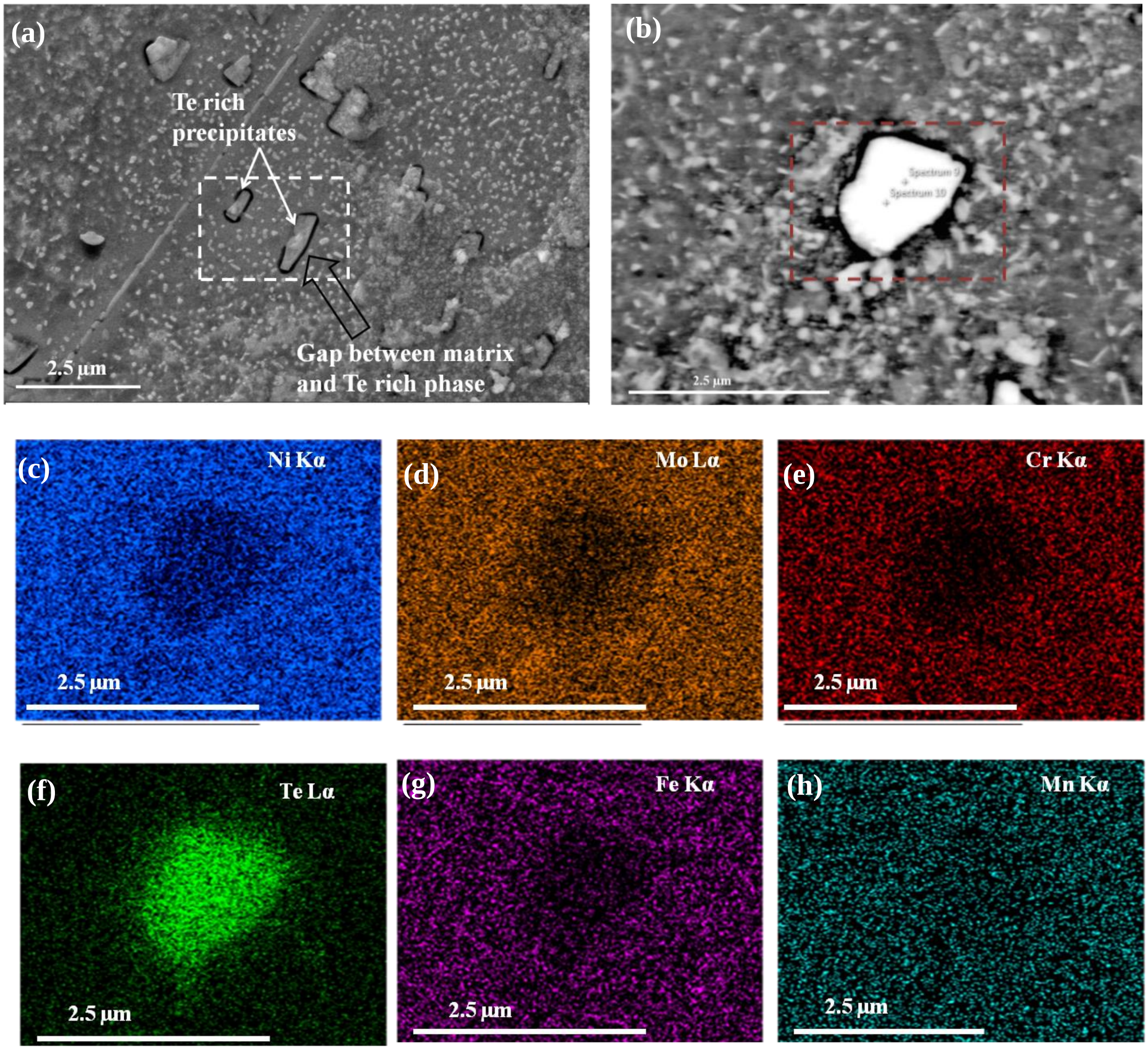

Fig. 6.2: (a) Surface morphology, (b) BSE image and X-ray maps for (c) Ni Kα (d) Mo Lα (e) Cr Kα (f) Te Lα (g) Fe Kα and (h) Mn Kα for Te coated alloy annealed at 973 K for 96 h and WQ.

Additionally, it was observed that the Te rich precipitate boundaries are often detached from the alloy matrix creating a void/free space between them. This space indicates decohesion of the precipitates from the alloy matrix which probably results from the volume change associated with the formation of these precipitates. Few Mo rich precipitates having composition 74.4 at.% Ni- 12.1 at% Mo-8.9 at% Cr - 4.1 at% Fe were also observed (not shown in fig.) and are possibly carbide phases which are also extensively studied and reported in literature [114]. Detailed analyses on the characteristics of these carbides are described elsewhere [114] and hence are not repeated in present study. No Cr or Mo rich telluride was identified on the surface.

Similar reaction products were observed in case of Te coated alloy annealed at 973 K and furnace cooled. SE images of the alloy surface indicate the formation of Te rich islands and the possible tellurides formed are Ni_3Te_2 type precipitates with a composition approximately Ni: 59.8 at.% -Te: 38.5 at.% -1.7 at.% Cr (Fig. 6.3).

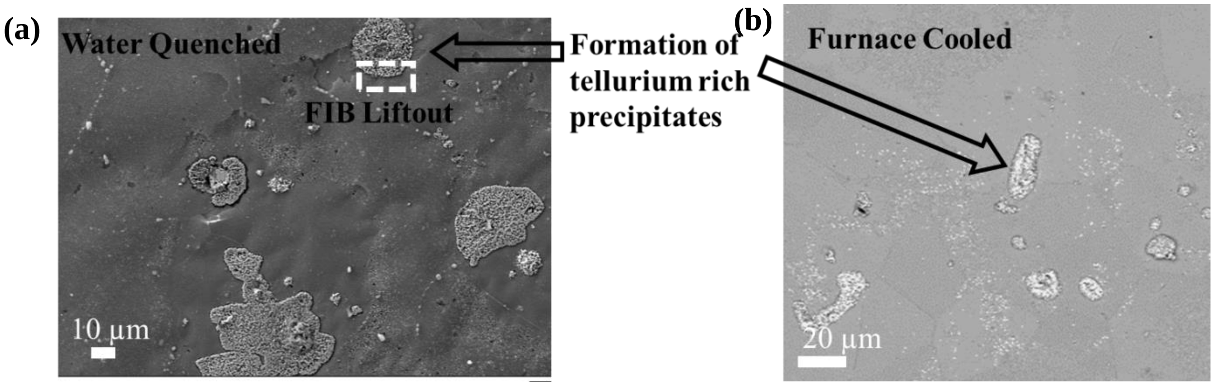

Fig. 6.3: SE image of Te coated alloy annealed at 973 K for 96 h and (a) WQ (b) Furnace cooled.

6.2.2 Microstructure along the alloy cross-section

Fig. 6.4 shows the extent of tellurium attack in the alloy. With the ingress of tellurium into the alloy, the surface of the alloy no longer remains uniform and develops a reaction layer. Since the solubility of Te in nickel is extremely low (<0.25 at.% at room temperature), it results in the formation of nickel rich tellurides. The reaction layer has a depth of ~27.7 µm from the alloy surface and shows the formation of crack along grain boundary as well as decohesion of tellurides from the alloy matrix.

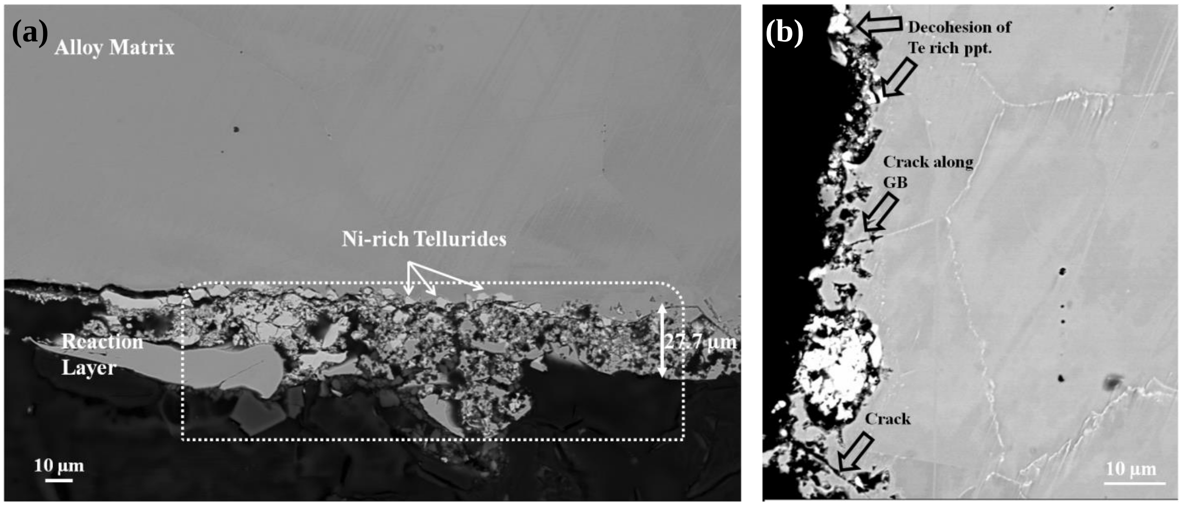

Fig. 6.4: (a)-(b) BSE micrograph for the cross-section of Te coated alloy annealed at 973 K for 96 h and WQ.

6.3 Crystallography of precipitates

High resolution HAADF images of the alloy cross-section presented in Fig. 6.5 show the Z-contrast. The reaction layer is weakly attached to the alloy matrix and mainly consists of the tellurides. The HAADF image in conjunction with the X-ray mapping show that the interaction layer comprises reaction products of type Mo-rich carbides (region marked as "A" in Fig. 6.5(b)) as well as Ni-rich tellurides (region marked as "B" in Fig. 6.5(b)). The tellurides are formed adjacent to Mo-carbides indicating that the MoC carbides act as nucleation site for the tellurides. Furthermore, a faulted structure was also observed which was identified to be Ni-rich telluride.

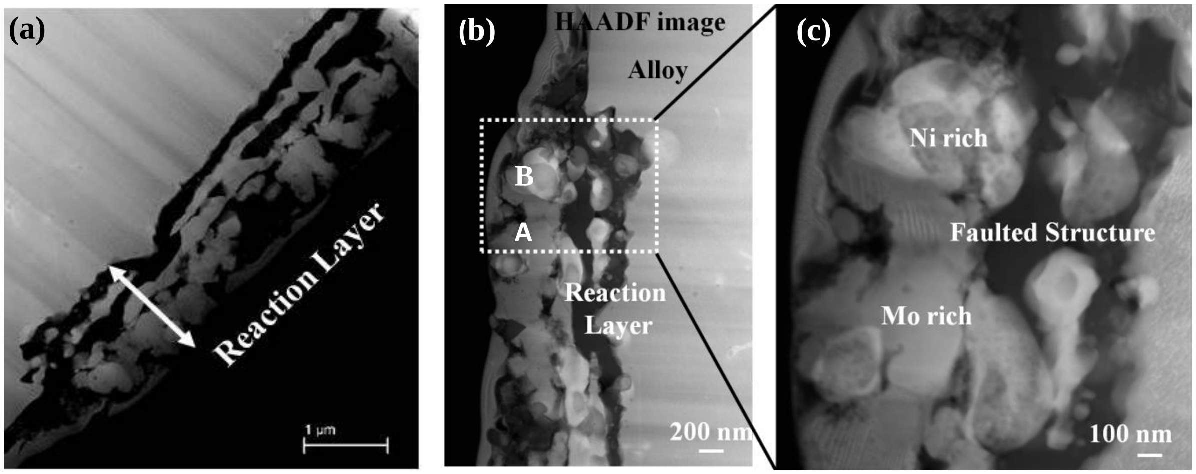

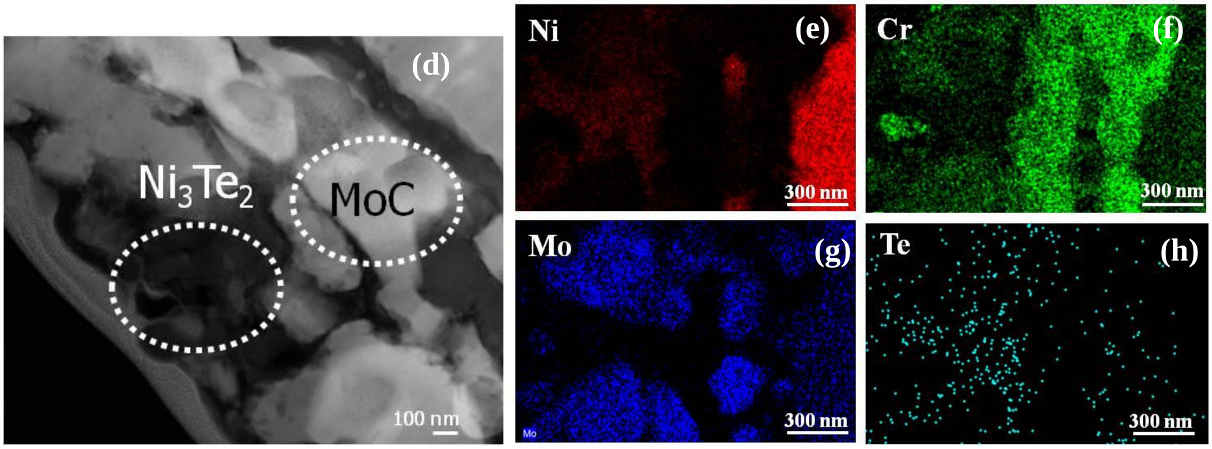

Fig. 6.5: (a)-(d) High angle annular dark field image, X-ray maps for (e) Ni Kα (f) Cr Kα (g) Mo Lα (h) Te Lα for Te-coated Ni-Mo-Cr alloy annealed at 973 K for 96 h and WQ.

The SAED patterns from the precipitate marked "A" in Fig. 6.5 (a) along the zone axes $[1\bar{1}1]$ and [012] is presented in Fig. 6.6. This Mo rich carbide is identified to be MoC type with a cubic structure having lattice parameter a=b=c= 4.30 Å and space group $Fm\bar{3}m$ (space group no. 225).

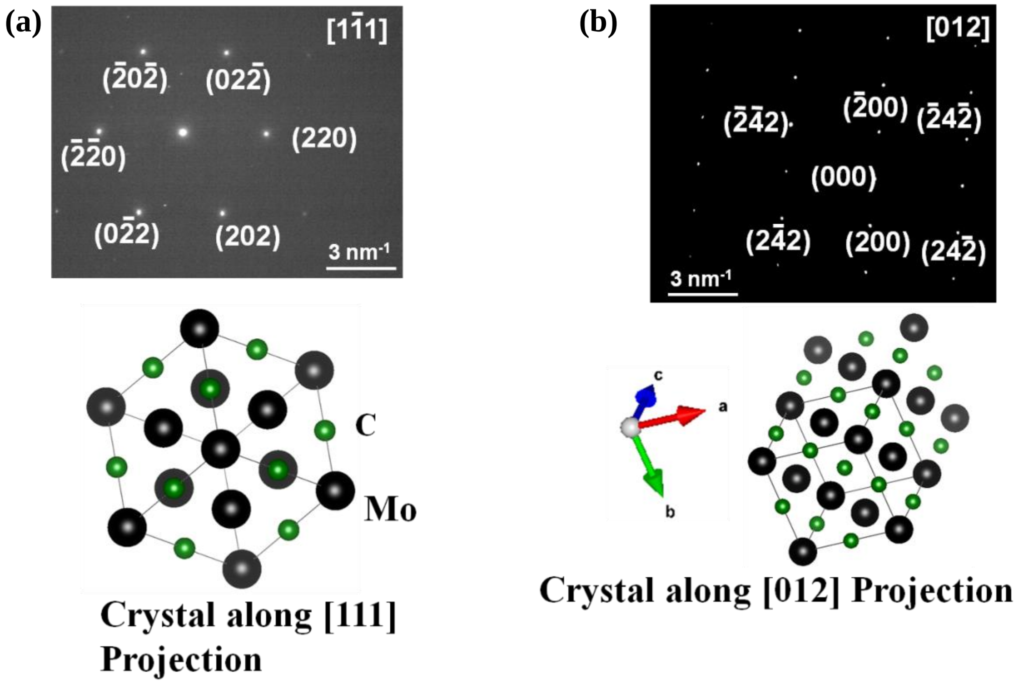

Fig. 6.6: SAED patterns for MoC precipitates recorded along $[1\bar{1}1]$ and [012] zone axis along with the corresponding projections of the crystal lattice.

From the TEM-EDS analysis of Ni-rich tellurides (including the faulted structure) the composition is found to be Ni: 56.91 at.%;Te: 42.15 at.% Rest: Mo which correspond to that of $Ni_{3\pm\delta}Te_2$. Since the monoclinic and orthorhombic structures for $Ni_{3\pm\delta}Te_2$ phase have same lattice parameters, hence the ambiguity regarding the crystal structure can be removed by considering the structure factors for different planes of each phase, computing the theoretical Bragg peak intensity and matching with the observed SAED patterns recorded at different zone axes. From the TEM analyses (Fig. 6.7), it is confirmed that the Ni rich precipitate is β2 type Ni_3Te_2 type precipitate. The details of the structure factors as obtained from the standard crystal structures of orthorhombic and monoclinic Ni_3Te_2 type structure for comparison is presented in Table 6.3.

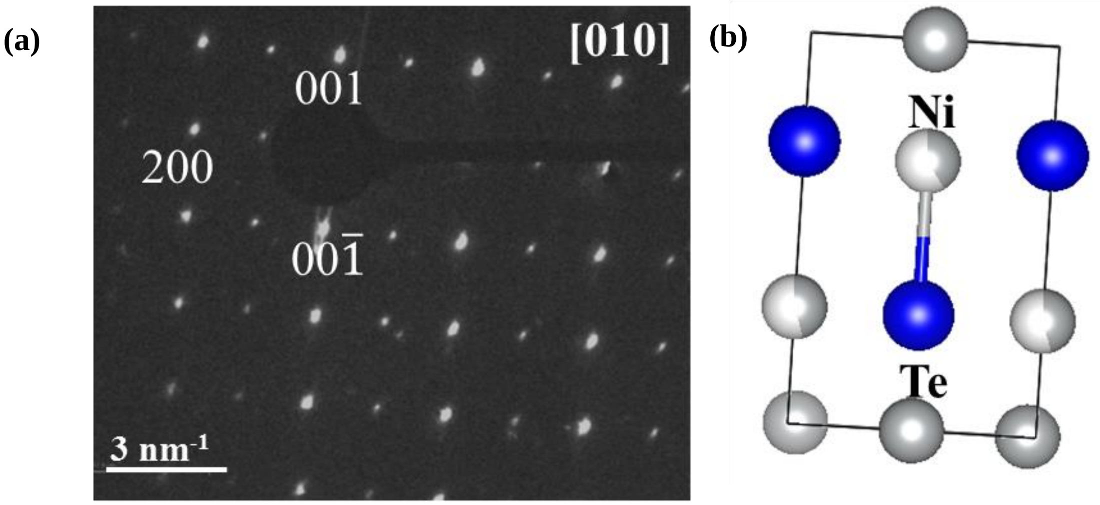

Fig. 6.7: (a) SAED pattern for $Ni_{3-\delta}Te_2$ type precipitate along [010] zone axis and (b) the projection of orthorhombic unit cell of the same phase along (010) direction.

Table 6.3: Structure factors for the Ni $_{3\pm\delta}$Te$_2$ orthorhombic and monoclinic structures.

Plane (hkl)	Magnitude of structure factor |F| for Ni $_{3\pm\delta}$Te$_2$	
	Orthorhombic	Monoclinic
001	14.9	30.4
101	65.3	37.5
200	115.4	5.98
111	61.5	19.5

6.4 Effect of temperature on alloy microstructure

The Te coated alloy sample annealed at 1073 K for 96 h and WQ also show formation of Te rich phases within the size range 1-4 µm, distributed throughout the alloy matrix. A representative image showing such irregularly shaped precipitates is shown in Fig. 6.8(a). The composition of this precipitate as obtained by EDS point scan (Table 6.4) suggests that the precipitate is enriched in Mo and Te. This is further confirmed by the detailed X-ray mapping of the elements (Fig. 6.8 (b)-(f)).

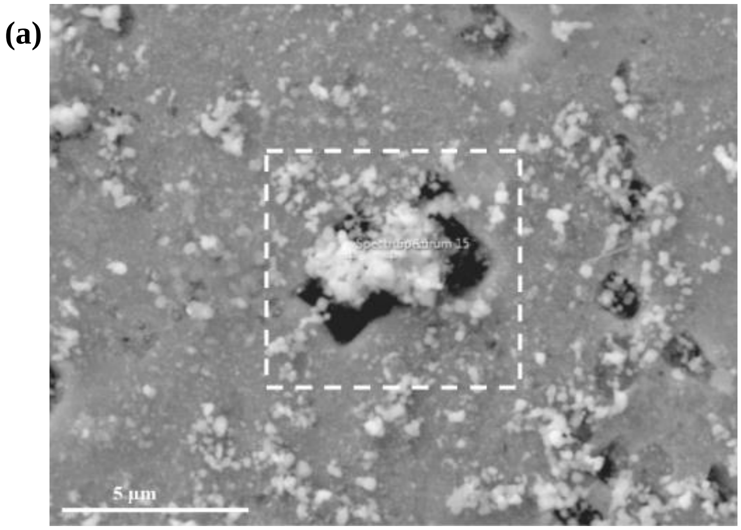

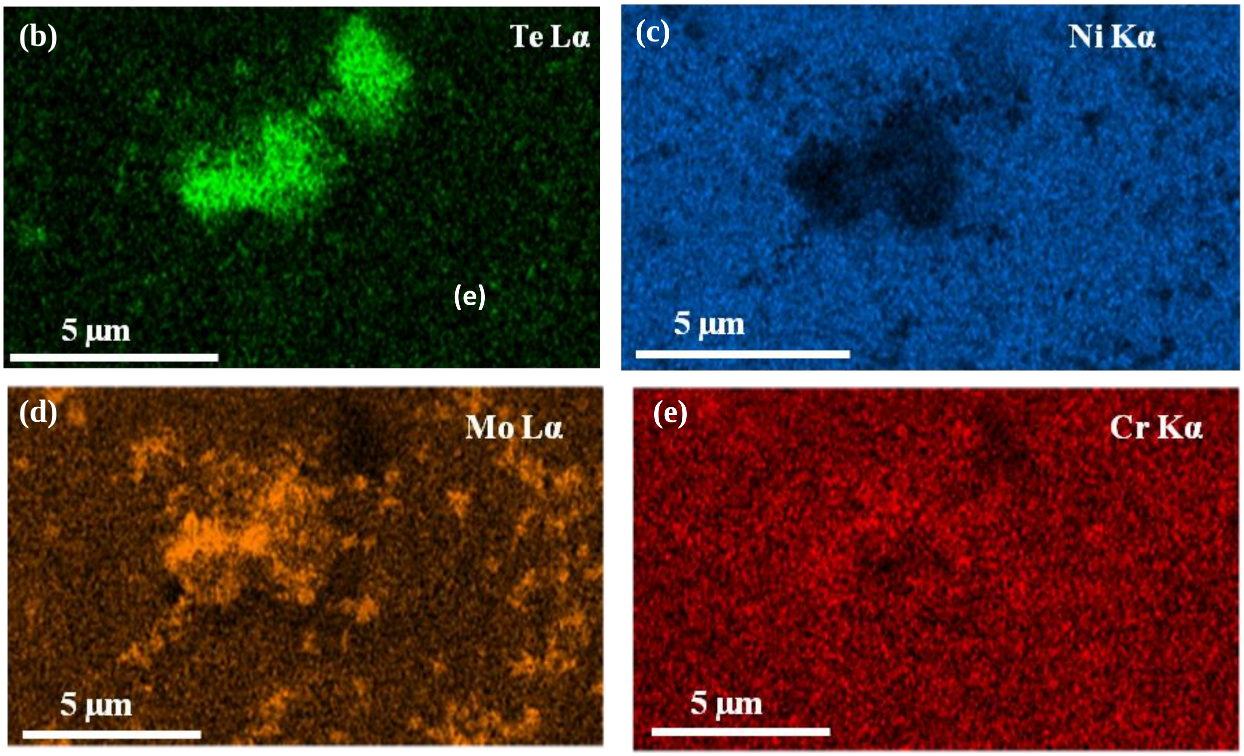

Fig. 6.8: (a) Surface morphology and (b) Te L_α (c) Ni K_α (d) Mo L_α and (e) Cr K_α elemental X-ray mapping for Te coated alloy annealed at 1073 K for 96 h (and WQ).

Table 6.4: EDS analysis of the precipitate formed in the Te-coated alloy after annealing treatment at 1073 K for 96 h and WQ.

Element	Ni	Cr	Mo	Fe	Te
Concentration (wt.%)	22.2	16.2	45.3	0.8	15.4

Due to the small size of the precipitate and limitation imposed by the interaction volume of incident electron beam with alloy it is difficult to ascertain if MoTe is formed or Mo rich carbides alongside pure Te. Formation of such Te or /and Mo rich phases in Hastelloy N when subjected to Te vapour at 1073 K is reported earlier by Cheng *et al.* [72]. Another study by ORNL [35-36] and Lu *et al.* [71] suggest that the Nickel tellurides Ni_3Te_2 which is prominent phase at 973 K undergoes disintegration through the following reaction [71-75]

$$Ni_3Te_2\ (c) \rightarrow 3Ni\ (c) + Te_2\ (g) + 128.9\ \text{kJ/mol};\ T = 1073\ \text{K} \qquad 6.1$$

In present case, no nickel rich tellurides were identified which could be attributed to disintegration of tellurides into Te and Ni at T $\geq$ 1073 K.

6.5 Cluster Expansion results

From the convex hull in Fig. 6.8 (a), it is observed that all the NiTe and Ni_3Te_2 phases are thermodynamically stable at 0 K owing to negative heat of formation. For Ni_3Te_2 phase, the stability sequence obtained for different crystal structures for same phase is Orthorhombic (-2.83 eV) > Tetragonal (-2.74 eV) > Monoclinic (-2.41 eV).

The effective pair, triplet and quadruplet interaction energies (ECIs) for Ni-Te system for the solute concentration range Te: 0-100 at.% were deduced. The first nearest neighbour interaction energy was calculated to be 0.28 eV/atom and was found to have the highest magnitude amongst all. The positive value indicated that Te prefers Ni as its first nearest neighbour. With the increase in cluster diameter the magnitudes of ECIs decrease and for a cluster diameter of 7.42 Å, the magnitude of ECI becomes almost negligible with a value of 0.001 eV/atom. Additionally, the magnitudes of ECIs for multi-body (triplets and quadruplets) clusters were much smaller as compared to the 2-point or pair clusters, indicating a good convergence of cluster expansion based model. Moreover, higher magnitudes of ECIs for pair clusters than those for triplets or quadruplets suggest that nearest neighbour pair interactions are dominant and play a crucial role in determining the configurational energy of the Ni-Te alloys.

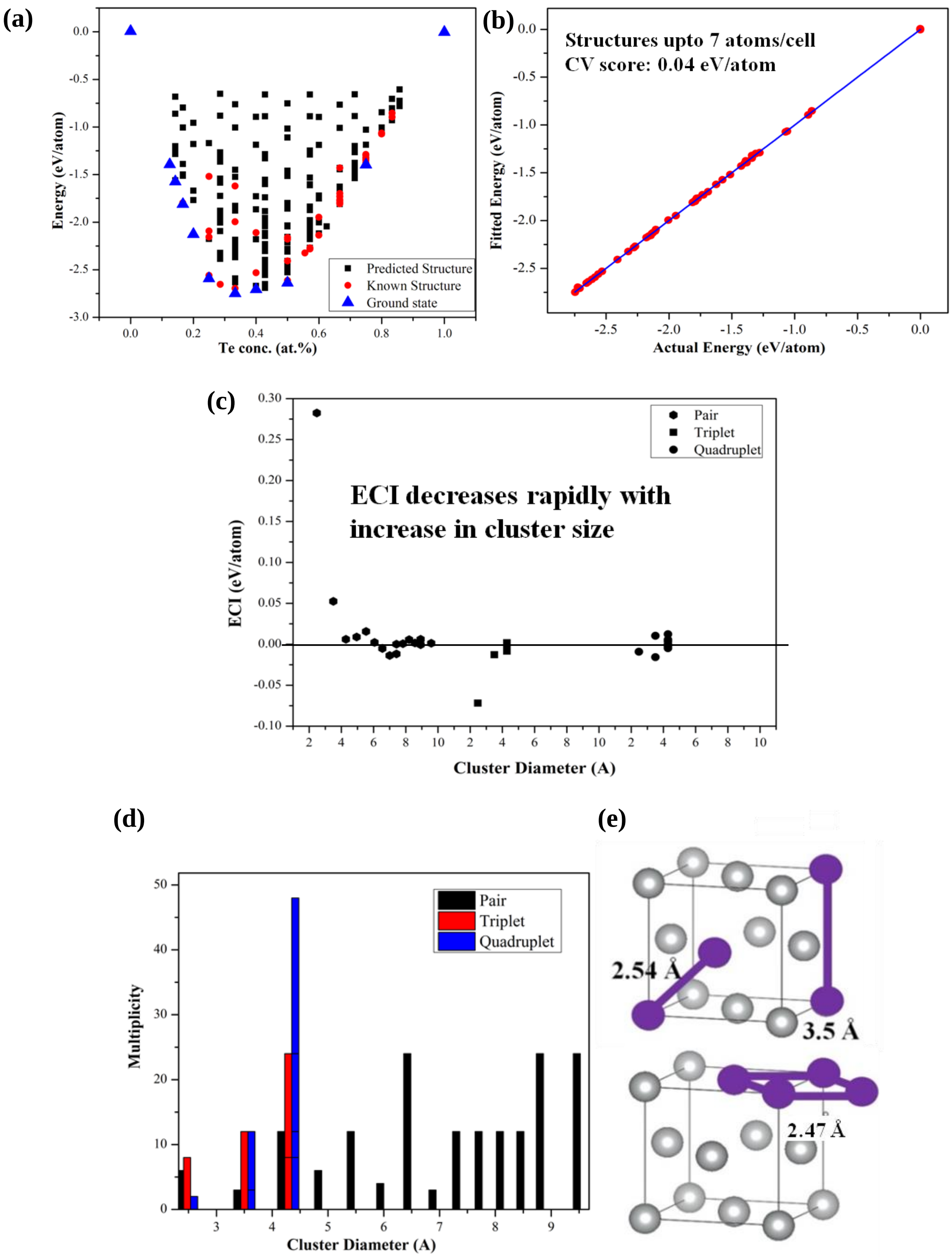

Fig. 6.9: (a) Convex hull showing energy as a function of Te concentration plot, (b) Fit between VASP calculated and CE fitted energies, (c) ECIs as a function of cluster diameter, (d) cluster multiplicity, and (e) Representative clusters. The CV score for the calculation was 0.04 eV/atom.

6.6 Discussion of Results

6.6.1 Formation of precipitates

The tellurium attack of the alloys is expected to occur in a manner analogous to internal oxidation of alloys since Te has same valence electronic configuration as oxygen. Te has a melting point of 722 K and hence at the annealing temperature of 973 K Te will melt and form droplets nearly of spherical shape due to a high surface tension. The Te liquid then reacts with the surface Ni, Cr and Mo atoms to form tellurides and Te rich islands as observed in the appearance of clusters/islands of tellurides on the alloy surface.

The formation of Ni-rich tellurides in Hastelloy N occurs via the following reaction

$$\mathrm{3Ni + 2Te \rightarrow Ni_{3-\delta}Te_2} \qquad 6.2$$

$$\mathrm{Ni + Te \rightarrow Ni\,Te} \qquad 6.3$$

The CE calculations indicate the tendency for ordering in the Ni-Te system which results in the formation of ordered intermetallic compounds/precipitates. The positive value of ECI indicates the tendency for ordering and hence facilitates the formation of ordered precipitates. Of several tellurides possible, the calculations show that NiTe phase is most stable phase in the Ni-Te system. However, in the temperature range of 873 K-973 K, the $\mathrm{Ni_{3-\delta}Te_2}$ is found to be the most stable phase [154]. It appears likely that the NiTe phase which forms at first decomposes to $\mathrm{Ni_{3-\delta}Te_2}$ at 873 K by the following reaction [71]. The observed decohesion of telluride precipitates, as observed in TEM studies, appeared to have resulted from the evolution of gaseous phase.

$$\mathrm{6NiTe \rightarrow Ni_{3-\delta}Te_2 + Te_2(g)} \qquad 6.4$$

Due to the formation of these precipitates, the modified alloy matrix gets supersaturated with other elements [155] such as Fe and C etc. This facilitates the formation of MoC type carbides which further act as the heterogeneous nucleation sites for nickel tellurides.

Upon increasing temperature above 1073 K, the nickel tellurides disintegrate into Te and Ni by the equation 6.1 and hence for the Te coated Hastelloy N annealed at 1073 K, no nickel rich tellurides were observed.

6.6.2 Diffusion of Tellurium into the alloy

Tellurium diffuses into the alloy by both lattice and grain boundary diffusion mechanism. The grain boundary diffusivity of Te in Hastelloy N at 973 K is estimated to be 2.08 × 10^{-13} cm^2/s by Cheng *et al.* [154] while the lattice diffusivity of Te in Ni-Mo-Cr alloy at 833 K is estimated is estimated to be 1.0 × 10^{-14} cm^2/s. T

he effective diffusivity (D_{eff}) of the tellurium in the alloy is expressed by the following equation as given by Jiang *et al.* [155]

$$D_{eff} = D_V + \frac{2*\delta*D_{gb}}{Alloy\ grain\ size} \qquad 6.5$$

where δ is the grain boundary width δ=0.5 nm. The effective diffusivity D_{eff} can also be estimated from the Te penetration depth as calculated from SEM investigations on the alloy cross sections annealed at 973 K for 96 h using the equation [143],

$$x = (2D_{eff}t)^{1/2} \qquad 6.6$$

where x=27.7 µm is the characteristic diffusion distance which is a measure of Te penetration depth and t=96 h is the exposure time. Using the value, the effective diffusivity of Te in the Te coated alloy annealed at 973 K for 96 h and WQ is determined to be ~1.11 x 10^{-13} cm^2/s which indicates that Te predominantly diffuses into the alloy by grain boundary diffusion mechanism.

6.6.3 Role of precipitates in microstructural degradation of the alloy

From the electron microscopy results it is evident that the nickel tellurides are completely incoherent with the alloy matrix with no orientation relationship. The c-axis is reduced in height while *a* and *b* lattice parameters are enhanced during the process of telluride formation resulting in a volume change and hence the precipitates detached from the alloy matrix (Fig. 6.10). Furthermore, it is observed that the 5-unit cells of Ni (20 atoms) will have the same number of atoms as 2-unit cells of Ni_3Te_2 (20 atoms) and comparing the volume change associated with per unit atom is calculated to be ~53.8%.

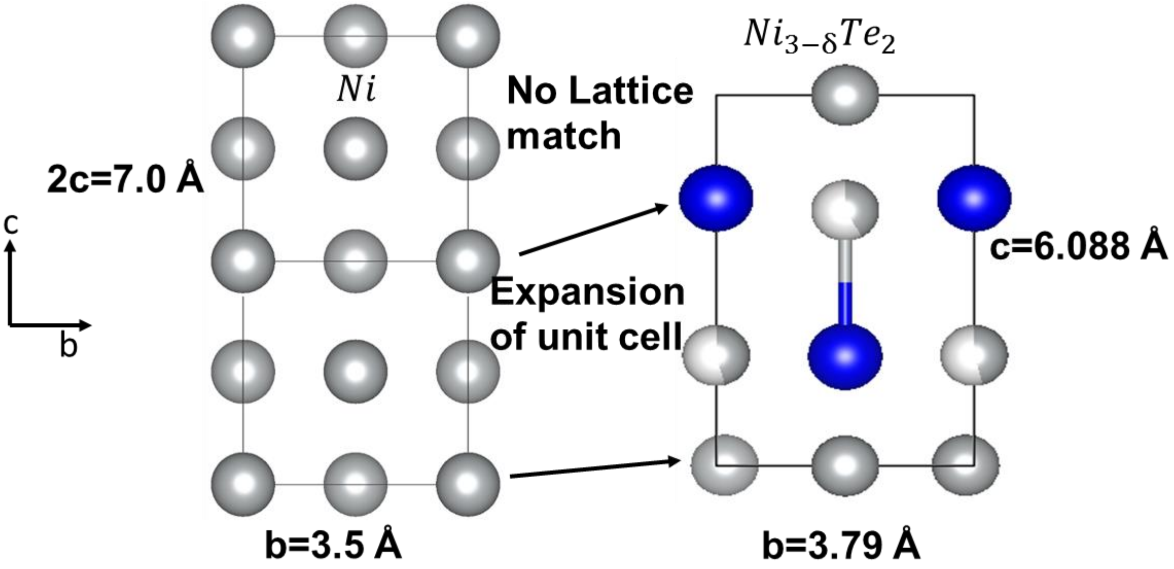

Fig. 6.10: Schematic of the 001 projection of Ni and $Ni_{3-\delta}Te_2$ unit cell.

The overall mechanism of Te attack on Ni-Mo-Cr alloy and its subsequent microstructural degradation is summarized in Fig. 6.11.

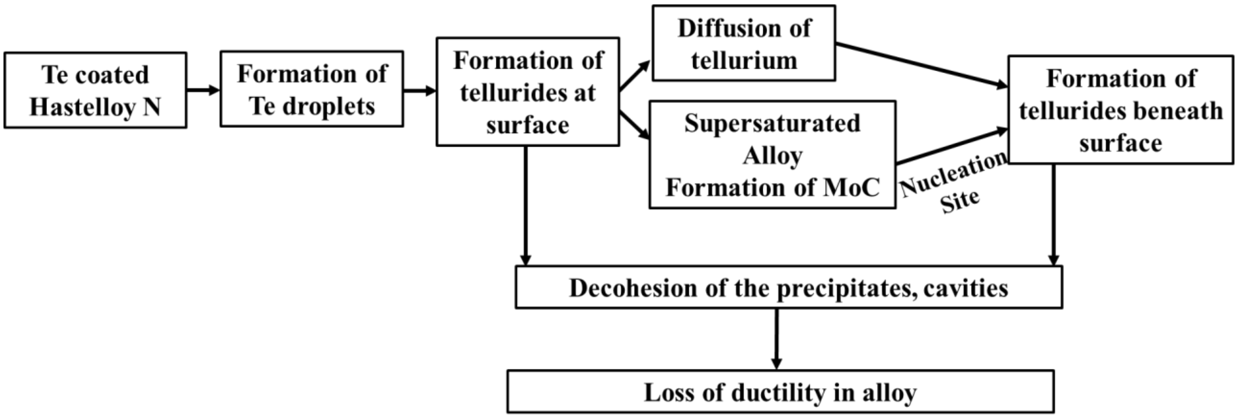

Fig. 6.11: A flowchart depicting the tellurium induced degradation of the Ni-Mo-Cr alloy.

6.7 Summary

Microstructural evolution of Ni-Mo-Cr based alloy Hastelloy N coated with Te and annealed at 973 K for 96 h reveal presence of irregularly shaped fine inter- and intra-granular Ni rich tellurides (size in the range of 1-3 μm) of $Ni_{3-\delta}Te_2$ type having orthorhombic structure. These precipitates have low adhesion with the alloy matrix which is attributed to a large volume change per atom (~53.8 %) associated with precipitation and hence are easily detached from the alloy matrix. A mechanism for formation of telluride formation and its subsequent decohesion from the alloy matrix is proposed.

Chapter 7 : Conclusions and Scope for further research

7.1 Conclusions

The main aim of the present thesis was to make some assessments on the suitability of Ni-Mo-Cr alloys as the main structural material in a molten salt nuclear reactor. Such an assessment has several components, out of which those dealt in the present thesis are as follows:

a) Studies for gaining an understanding of the stability of different chemically ordered structures in the ternary Ni-Mo-Cr alloys have been conducted with a view to examine the possibility of formation of brittle ordered intermetallic phases during an extended exposure of this structural material at an elevated operating temperature. This part of the study has been supplemented with basic studies on the nature of the short range and long range ordered structures in both binary Ni-Mo and ternary Ni-Mo-Cr alloys.

b) Studies related to the assessment of the compatibility of a Ni-Mo-Cr alloy and several commercial nickel base alloys with molten fluoride salts containing oxygen, in the operating temperature range have been carried out.

c) As fission products come in contact with the structural containment material during the operation of molten salt reactor, the degradation of this material by the ingress of tellurium, a fission product, may be its life limiting factor. The mechanism of interaction of tellurium with the Ni-Mo-Cr alloy, resulting in its microstructural changes and degradation, has been studied in detail.

The major outcomes of the investigations made and reported in the present dissertation are summarized below.

7.1.1 Ordering transformations in Ni-20 at.% Mo alloy

(i) Complementary diffraction, imaging and EXAFS studies show that the as-quenched (quenched from the dis-ordered fcc phase) structure of binary Ni-20at% Mo alloy, characterized by the presence of diffuse {1 ½ 0} reflections truly correspond to a Short Range Ordered (SRO) structure in which there is a clear preference for unlike atoms at the first nearest neighbour distance. EXAFS studies performed for the first time give evidence that no Mo-Mo bonds exist at first NN distance, and also, Ni-Mo and Mo-Ni bond lengths differ due to the presence of SRO in the as quenched alloy. Furthermore, the Warren Cowley parameters, evaluated using EXAFS fit have been found to be in close agreement with the previously reported parameters deduced from XRD patterns. The local atomic configurations of the SRO structure, obtained from the EXAFS studies have been found to be consistent with the earlier proposed static concentration wave packet model which is also a statistical description of the presence of clusters or motifs representing competing ordered structures.

(ii) Diffraction experiments have shown that the Long Range Ordered (LRO) structure of the aged (at a temperature below the reported ordering temperature) alloy is described by the $D1_a$ structure which grows coherently with the fcc matrix. EXAFS studies, additionally, establish that the Mo-Mo bonds in first coordination shell are absent and Mo has all Ni atoms as the first NN. The adjacent LRO domains are found to have either an anti-parallel twin or a perpendicular twin relationship, as expected from the crystallography of the ordering transformation.

(iii) Evaluation of the ordering tendency of the alloy was rationalized in terms of the interaction parameters. Evaluation of the pair interaction parameters (related to pair interaction energies) using Cluster Expansion (CE) approach indicates that there exists a preference for unlike atoms at first NN distance which facilitates the formation of both SRO and LRO structures. The multisite interaction parameters for the Ni-Mo alloy were evaluated for the first time and the triplet interactions were observed to stabilize the ordering tendency.

(iv) From the Monte Carlo simulations, the order-disorder phase transition temperature (T_c), high temperature Warren Cowley parameters up to fourth NN distance and LRO parameter for Ni_4Mo system have been evaluated. The value of T_c has been found to be in close agreement with the transition temperature reported from experimental investigations.

It is thus established that the diffraction and EXAFS measurements in conjunction with the CE based calculations can be applied with reasonable accuracy to demonstrate the order-disorder phase transformation behaviour of the Ni-Mo alloys.

7.1.2 Role of Cr in altering the ordering characteristics in Ni-Mo alloy

(i) The SRO structure characterized by diffuse {1 ½ 0} reflections could not be observed in ternary Ni-Mo-Cr alloys with the conventional electron microscopy. However, the presence of SRO in the chosen alloy has been detected from the EXAFS measurements. It has been shown that both Cr and Mo preferentially bond with Ni atoms and there is no Mo-Cr bond at the first NN distance. The EXAFS analyses provide direct evidence that Cr replaces Mo in the fcc lattice, thereby, conclusively validating the previous models for the Ni-Mo-Cr alloys.

(ii) The addition of Cr is found to stabilize the disordered fcc configuration and destabilize the $D1_a$ phase. This is supported by the detailed first principles calculations which show that the enthalpy of formation for $D1_a$ phase becomes less negative with Cr addition while the entropy of the disordered fcc phase of the ternary alloy becomes more negative thereby increasing the stability of the later.

(iii) The change in the enthalpy of formation of the fcc and $D1_a$ phases with Cr addition was rationalized in terms of the pair and multisite interaction parameters. The ECIs for Ni-Mo and Ni-Cr system were compared since both Mo and Cr had Ni as its first NN. The calculations show that the sign and the magnitude of ECIs for pair and multisite interactions are changed for the two systems confirming the experimental observations that the ordering tendency is less in case of the Ni-Cr system as compared to the Ni-Mo system.

(iv) The absence of Pt_2Mo type ordered structure in the chosen ternary alloy has been rationalized in terms of the Mo+Cr concentration (~20 at.%) which was considerably less than that required for satisfying the stoichiometry (33 at.%) of the Pt_2Mo type structure. Moreover, the tendency of Mo to destabilize the Pt_2Mo structure is likely to reduce the thermodynamic force for Pt_2Mo type precipitation.

Thus, during the long-term exposure of the chosen ternary Ni-Mo-Cr alloy in the high temperature environment, no ordered intermetallic phase is likely to form and the alloy is expected to remain in the disordered fcc phase.

7.1.3 Microstructural evolution of Ni-Mo-Cr alloy in molten fluoride

(i) Ni-Cr based alloys, devoid of Mo, (as in cases of Alloy 693 and Alloy 690) upon exposure to the molten FLiNaK salt containing oxygen results in the formation of fluorides as well as oxides at the surface. These oxide layers (primarily, Cr oxide) are found to be partially covering the alloy surface, forming galvanic micro-couples with the exposed surface. As a result, the fluoride attack on the exposed alloy surface is further aggravated. The consequent Cr dissolution from the exposed alloy surface to the molten salt is thus increased. The elevated temperature of operation allows Cr diffusion from the bulk to the exposed surface and aids to the dissolution of Cr from the alloy to the molten salt.

(ii) The present work has clearly shown that in the case of the Ni-Mo-Cr alloy, presence of Mo-rich oxide layer over the areas devoid of oxide patches in Ni-Mo-Cr alloys reduces the galvanic coupling between Ni-, Cr-rich oxides and exposed surface. This results at lower Cr depletion from the alloy as compared to Alloy 693 and Alloy 690 which could not develop a continuous adherent oxide layer on the surface.

It is also shown that the oxygen impurity in FLiNaK salt is highly deleterious even in small concentration since the Cr depletion is enhanced in the presence of oxygen and remains so, even after the dissolved oxygen in the salt is used up due to the micro-galvanic couple formation.

7.1.4 Microstructural evolution of Ni-Mo-Cr alloy under tellurium attack

(i) Te- coated Hastelloy N annealed for 96 h at 973 K and WQ has shown that incoherent precipitation of nickel tellurides occurs at the surface owing to the reaction between Te and surface Ni atoms. Diffraction experiments establish the precipitates formed are β2 type Ni_3Te_2 precipitates. It is further concluded that the formation of Ni-rich tellurides causes super-saturation of Mo in the alloy. This leads to the formation of cubic MoC type precipitates that act as sites for the Ni-tellurides nucleation thereby causing further degradation.

(ii) Effective diffusivity of Te in the alloy was evaluated and its comparison with the available literature reports show that the diffusion of Te in the alloy is predominantly through the grain boundaries.

(iii) The observed decohesion of the precipitates from the alloy matrix is explained on the basis of volume change associated with precipitation and Te gas evolution which lead to cavity formation at the interface between the matrix and the telluride precipitates which eventually lead to surface cracks.

(iv) The formation of Ni-Te type precipitates can be explained on the basis of low solubility of Ni in tellurium as well as nearest neighbour interaction energies. The pair and multisite ECIs evaluated for the Ni-Te system by CE approach show that there is a preference for unlike atoms around Te atoms in the first coordination shell. This ordering tendency favours the formation of Ni-rich tellurides.

7.2 Scope for further research

In present thesis, the ordering phase transformation behaviour of the Ni-Mo and Ni-Mo-Cr alloys, their microstructural evolution when exposed to the simulated service conditions has been investigated. The study has provided insights to an understanding of phase transformation mechanisms as well as the microstructural stabilities of the alloy in reactor environment indicating that the alloy possesses favourable properties for use at operating conditions. The dissertation work can further be elaborated along the following directions.

(i) Ordering in Ni-Mo-Cr alloys:

(a) The cluster expansion approach can be used to study the interaction energies for the ternary Ni-Mo-Cr system and investigate the variation of Gibbs free energy as a function of order parameter and temperature for the $Ni_2(Cr_xMo_{1-X})$ stoichiometry. Such a study can predict the stabilities of $Ni_2(Mo,Cr)$ precipitates commonly observed in Ni-Mo-Cr alloys with high Cr content.

(b) Precession electron microscopy can be carried out to observe the nature of SRO and LRO in Ni_4Mo and Ni-Mo-Cr alloys and identify the atomic sites where Cr replaces Mo.

(c) Determining the critical concentration of Cr at which the Ni-Mo-Cr alloy with Mo+Cr~20 at.% destabilizes the D_{1a} phase.

(ii) Behaviour of Ni-Mo-Cr alloys under simulated service conditions:

Radiation damage in Ni-Mo-Cr alloys by high energy electrons and ions at elevated temperatures is an important aspect which can be looked into with a view to assessing the possibility of formation of ordered precipitates in a radiation environment.

References

[1] “Superalloys II”, by C.T. Sims, N.S. Stoloff, W.C. Hagel, John Wiley and Sons, New York, **1987**.

[2] “Perspectives on radiation effects in nickel-base alloys for applications,” A. F. Rowcliffe, L. K. Mansur, D. T. Hoelzer, R. K. Nanstad, *Journal of Nuclear Materials*, **2009,** *392*, 341-352.

[3] “Generation IV nuclear reactors: Current status and future prospects”, G. Locatelli, M. Mancini, N. Todeschini, *Energy Policy*, **2013**, *61*, 1503–1520.

[4] “Molten salt reactors: A new beginning for an old idea”, David Le Blanc, *Nuclear Engineering and Design*, **2010**, *240* 1644–1656.

[5] “The Welding Metallurgy of Hastelloy alloys C-4, C-22 and C-276”, M. J. Cieslak, T.J. Headley, A.D. Romig, *Metallurgical Transactions A*, **1986**, *17A*, 2035-2047.

[6] “The molten salt reactor (MSR) in generation IV: overview and perspectives”, J. Serp, M. Allibert, O. Benes, S. Delpech, O. Feynberg, V. Ghetta, D. Heuer, D. Holcomb, V. Ignatiev, J. L. Kloosterman, L. Luzzi, E. Merle-Lucotte, J. Uhlír, R. Yoshioka, D. Zhimin, *Progress in nuclear energy*, **2014**, *77*, 308-319.

[7] “Handbook of Generation IV reactors”, by Igor Pioro, Woodhead Publishing, Cambridge, USA, **2016**.

[8] “Generation-IV nuclear power: A review of the state of the science”, T. Abram, S. Ion, *Energy Policy*, **2008**, *36 (12)*, 4323-4330.

[9] “Molten salt reactors and thorium energy”, by Thomas J. Dolan, Woodhead Publishing, Cambridge, USA, **2017**.

[10] “Materials challenges for nuclear systems”, T. Allen, J. Busby, M. Meyer, D. Petti, *Materials Today,* **2010**, *13*, 14-23.

[11] “Structural materials for Gen-IV nuclear reactors: Challenges and opportunities”, K. L. Murty, I. Charit, Proceedings of the International Conference on Advances in Nuclear Materials: Processing, Performance and Phenomena, *Journal of Nuclear Materials*, **2008**, *383,* 189–195.

[12] “Binary Alloy Phase Diagrams–Second edition”, by R. W. Cahn, Eds. T. B. Massalski, H. Okamoto, P. R. Subramanian, L. Kacprzak, ASM International, Materials Park, Ohio, USA. **1990**.

[13] “A First-Principles Thermodynamic Approach to Ordering in Ni-Mo Alloys”, A. Arya, S. Banerjee, G. P. Das, I. Dasgupta, T. Saha-Dasgupta, A. Mookerjee, *Acta Materialia*, **2001,** *49 (17)*, 3575-3587.

[14] “First–principles studies of phase stability and order–disorder transformations in Al–Li and Ni–Mo alloys”, A. K. Arya, PhD Thesis, Unpublished, **1997**.

[15] “Welding metallurgy and weldability of nickel-base alloys”, by J. N. Du Pont, J. C. Lippold, S. D. Kiser, A John Wiley and Sons INC. Publication, New Jersey, **2009**.

[16] “The Cr-Mo-Ni (Chromium-Molybdenum-Nickel) System”, A. K. Jena, S. B. Rajendraprasad, K. P. Gupta, *Journal of Alloy Phase Diagrams*, **1989**, *5*, 164-177.

[17] “Decomposition and ordering processes involving thermodynamically first-order order → disorder transformations”, W. A. Soffa, D. E. Laughlin, *Acta Metallurgica*, **1989**, *37,* 3019-3028.

[18] “Short range order in Ni-Mo, Au-Cr, Au-V and Au-Mn alloys”, S. K. Das, P. R. Okamoto, P. M. J. Fisher, G. Thomas, *Acta Metallurgica,* **1973**, *21*, 913-928.

[19] "On Short Range Order and Micro-Domains in the Ni_4Mo system", P. R. Okamoto, G. Thomas, *Acta Metallurgica,* **1971**, *19*, 825-841.

[20] "Understanding mechanisms of solid-state phase transformations by probing nuclear materials", S. Banerjee, H. Donthula, *Journal of Nuclear Materials,* **2018,** *501*, 143-161.

[21] "Effect of chromium addition on the ordering behaviour of Ni–Mo alloy: experimental results vs. electronic structure calculations", A. Arya, G. K. Dey, V. K. Vasudevan, S. Banerjee, *Acta Materialia*, **2002**, *50*, 3301–3315.

[22] "Ordering reactions in a Ni-25Mo-8Cr alloy", M. Kumar, V. K. Vasudevan, *Acta Materialia*, **1996**, *44*, 1591-1600.

[23] "Ordering in Ni-Mo alloys: First-principles calculations versus experimental observations", S. Banerjee, A. Arya, G. P. Das, *Bulletin of Materials Science,* **1997**, *20(6)*, 787-803.

[24] "Effects of ordering on the properties of Ni-Cr alloys", A. Marucco, B. Nath, *Journal of Material Science*, **1988**, *23*, 2107-2114.

[25] "Order evolution in Ni-Cr-Mo alloys", A. Verma, PhD Thesis, Unpublished, **2015**.

[26] "Topologically close packed precipitations and phase diagrams of Ni-Mo-Cr and Ni-Mo-Fe and of Ni-Mo-Fe with constant additions of chromium", E. Gozlan, M. Bamberger, S. F. Dirnfeld, B. Prinz, J. KIod, *Materials Science and Engineering A*, **1991**, *141*, 85-95.

[27] "Gamma Phase and Ni_2Cr-type long-range order in Ni-rich Ni-Cr-Mo alloys", L. Karmazin, J. Krejci, J. Zeman, *Materials Science and Engineering A*, **1994**, *183*, 103-109.

[28] “Influence of Mo addition on the solvus temperature of Ni_2(Cr,Mo) phase in Ni_2(Cr,Mo) alloys”, H. C. Pai, M. Sundararaman, B. C. Maji, A. Biswas, M. Krishnan, *Journal of Alloys and Compounds*, **2010**, *491*, 159-164.

[29] “Modelling of Ni–Cr–Mo based alloys: Part I-phase stability”, P. E. A. Turchi, L. Kaufman, Z. K. Liu, *Calphad*, **2006**, *30*, 70-87.

[30] “First-principles calculations and thermodynamic modeling of the Ni–Mo system”, S. H. Zhou, Y. Wang, C. Jiang, J. Z. Zhu, L. Q. Chen, Z. K. Liu, *Materials Science and Engineering A*, **2005**, *397*, 288–296.

[31] “Short Range Order in Ni_4Mo and its High-resolution electron microscopic images”, S. Hata, S. Matsumura, N. Kuwano, K. Oki, D. Shindo, *Acta Materialia*, **1998**, *46*, 4955-4961.

[32] “Monte Carlo study of ordering processes in fcc-based Ni-Mo alloys”, S. Hata, H. Fujita, C.G. Schlesier, S. Matsumura, N. Kuwano, K. Oki, *Material Transactions - Japan Institute of Metal*, **1998**, *39*, 133-138.

[33] “Effects of 10 MeV electron irradiation at high temperature of a Ni–Mo-based Hastelloy”, N. Wanderka, A. Bakai, C. Abromeit, D. Isheimc, D.N. Seidman, *Ultramicroscopy*, **2007**, *107*, 786–790.

[34] “Defect evolution in a Ni-Mo-Cr-Fe alloy subjected to high-dose Kr ion irradiation at elevated temperature”, M. Reyes, R. Voskoboinikov, A. Kirk, H. Huang, G. Lumpkin, D. Bhattacharyya, *Journal of Nuclear Materials*, **2016**, *474*, 155–162.

[35] “Identification from Tellurium-Structure-Material Interaction”, R. E. Gehlbach, H. Henson, ORNL/TM-4832, Oak Ridge, TN, USA, **1972**, 79–89.

[36] “Status of tellurium-Hastelloy N studies in molten fluoride salts”, J. R. Keiser, ORNL/TM-6002, Oak Ridge, TN, USA, **1977**, 1–23.

[37] “Alloys compatibility in molten salt fluorides: Kurchatov Institute related experience”, V. Ignatiev, A. Surenkov, *Journal of Nuclear Materials*, **2013**, *441*, 592-603.

[38] “Corrosion in Molten Salts”, K. Sridharan, T. R. Allen, in Molten Salts Chemistry (Eds. Frédéric Lantelme, Henri Groult), Elsevier, **2013,** 241-267.

[39] “Molten salt reactors – chemistry and materials”, D. D. Sood, proceedings of conf. on molten salts in nuclear technology (CMSNT-2013), **2013**, 43-55.

[40] “Status of materials development for molten salt reactors”, McCoy, Jr., H. E. Sun, ORNL-TM-5920; **1978**, Oak Ridge National Laboratory, USA. doi: 10.2172/5195742. https://www.osti.gov/servlets/purl/5195742.

[41] “Molten salts and nuclear energy production”, C. Le Brun, *Journal of Nuclear Materials*, **2007,** *360*, 1-5.

[42] “Thorium—Energy for the future: select papers from ThEC15”, by A. K. Nayak, B. Sehgal, Springer, New York, **2019**.

[43] “Development of materials and systems for molten salt-reactor concept”, H. G. Mac Pherson, *Reactor Technology*, **1972**, *15(2)*, 136–155.

[44] “High temperature reactor technology development in India”, V. Dulera, R. K. Sinha, A. Rama Rao, R. J. Patel, *Progress in Nuclear Energy*, **2017**, *101(A)*, 82-99.

[45] “Conceptual design of Indian molten salt breeder reactor”, P. K. Vijayan, A. Basak, I. V. Dulera, K. K. Vaze, S. Basu, R. K. Sinha, *Pramana – Journal of Physics*, **2015**, *85*, 539–554.

[46] “Pretest analysis of molten salt natural circulation loop using FLiNaK salt”, A. K. Srivastav, A. Borgohain, N. K. Maheshwari, P. K. Vijayan, Proceedings of conf. on molten salts in nuclear technology (CMSNT-2013), **2013**, 195-198.

[47] “Materials corrosion in molten LiF-NaF-KF salt”, L. C. Olson, J. W. Ambrosek, K. Sridharan, M. H. Anderson, T. R. Allen, *Journal of Fluorine Chemistry,* **2009,** *130*, 67-73.

[48] “Material performance in molten salts”, V. Ignatiev, A. Surenkov, In: R. J. M. Konings, *Comprehensive Nuclear Materials*, **2012**, 5, 221–250.

[49] “Molten salt corrosion of Ni-Mo-Cr candidate structural materials for Molten Salt Reactor (MSR) systems”, O. Muránsky, C. Yang, H. Zhu, I. Karatchevtseva, P. Sláma, Z. Nový, L. Edwards, *Corrosion Science*, **2019**, *159*, 108087.

[50] “Metallugical study on corrosion of austenitic steels in molten salt LiF-BeF$_2$ (FLiBe)”, M. Kondo, T. Nagasaka, A. Sagara, *Journal of Nuclear Materials*, **2009**, *386–388*, 685–688.

[51] “Theory of structural transformations in solids”, by A.G. Khachaturyan, Willey, New York **1983.**

[52] “K-space symmetry rules for order–disorder reactions”, D. de Fontaine, *Acta Metallurgica*, **1975**, *23*, 553–571.

[53] “Ordering Instabilities and Pretransitional Effects”, D. de Fontaine, *Metallurgical and Materials Transactions A*, **1981**, *12*, 559-556.

[54] “The problem of symmetry in statistical thermodynamics of substitutional and interstitial ordered solid solutions”, A. G. Khachaturyan, *Physics Statuts Solidi B*, **1973**, *60*, 9-37.

[55] “Short-range order and the disorder-order transformation in stoichiometric Ni_4Mo, J. P. Chevalier, W. M. Stobbs, *Acta Metallurgica*, **1979**, *27*, 1197-1217.

[56] “Computer simulation of the early stages of ordering in Ni-Mo alloys”, U. D. Kulkarni, S. Muralidhar, S. Banerjee, *Physica Status Solidi-A*, **1988**, *110*, 331-345.

[57] “Replacive ordering in alloys”, S. Banerjee, A. Arya, G. P. Das, *Physica A*, **1999**, *270*, 215-225.

[58] “HRTEM image contrast of short-range order in Ni_4Mo”, S. Hata, D. Shindo, T. Mitate, N. Kuwano, S. Matsumura, K. Oki, *Micron*, **2000**, *31*, 533–538.

[59] “Monte Carlo simulation of ordering transformations in Ni–Mo based alloys”, U. D. Kulkarni, *Acta Materialia*, **2004**, *52*, 2721-2732.

[60] “Monte Carlo simulations of ordering in Ni-Mo based alloys”, U. D. Kulkarni, *Metallurgical and Materials Transaction A*, **2008**, *39*, 1618–1622.

[61] “First-principles calculations of the electronic structure and phase stability of Ni–Mo alloys”, A. Arya, G. P. Das, S. Banerjee, M. J. Patni, *Journal of Physics: Condensed Matter*, **1998**, *10*, 8459–8475.

[62] “Initial stages of ordering in Ni_3Mo – thermal and irradiation ordering experiments”, S. Banerjee, U. D. Kulkarni, K. Urban, *Acta Metallurgica*, **1989**, *37 (1)*, 35-48.

[63] “A new paradigm for metallic alloys in materials science”, Y. Ustinovshikov, *Advances in Materials Physics and Chemistry*, **2015**, *5*, 244-270.

[64] “Interfaces in ordered intermetallics”, J. B. Singh, M. Sundararaman, S. Banerjee, *Bulletin of Materials Science*, **1997**, *20 (4)*, 541-548.

[65] “Abnormal kinetics of ordering transformation in $Ni_2(Cr_{0.5}, Mo_{0.5})$ alloy”, A. Verma, J. B. Singh, J. K. Chakravartty, *Journal of Alloys and Compounds*, **2015,** *639*, 341-345.

[66] “On the evolution of long-range order from short-range order in a $Ni_2(Cr_{0.5}Mo_{0.5})$ alloy”, A. Verma, N. Wanderka, J. B. Singh, M. Sundararaman, J. Banhart, *Journal of Alloys and Compounds*, **2014**, *586*, 561-566.

[67] “Influence of thermal exposure on the precipitates and mechanical properties of a newly developed Ni–21Cr–17Mo alloy”, Y. Zeng, L. Kou, X. Xie, *Materials Science & Engineering A*, **2013**, *560*, 611–617.

[68] “The high temperature corrosion of Hastelloy N alloy (UNS N 10003) in molten fluoride salts analysed by STXM, XAS, XRD, SEM, EPMA, TEM/EDS”, X. Ye, H Ai, Z Guo, H Huang, L Jiang, J Wang, Z Li, X Zhou, *Corrosion Science*, **2016,** *106*, 249-259.

[69] “Effect of moisture on corrosion of Ni-based alloys in molten alkali fluoride FLiNaK salt environments”, F. Y. Ouyang, C. H. Chang, B. You, T. K. Yeh, J. J. Kai, *Journal of Nuclear Materials*, **2013**, *437*, 201–207.

[70] “Effect of CrF_3 on the corrosion behaviour of Hastelloy-N and 316 L stainless steel alloys in FLiNaK molten salt”, H. Yin, J. Qiu, H. Liu, W. Liu, Y. Wang, Z. Fei, S. Zhao, X. An, J. Cheng, T. Chen, P. Zhang, G. Yu, L. Xie, *Corrosion Science*, **2018**, *131*, 355-364.

[71] “Local structure study of tellurium corrosion of nickel alloy by X-ray absorption spectroscopy”, L. Lu, Y. Jia, X. Ye, M. Luo, F. Song, Y. Huang, X. Zhou, Z. Li, Z. Jiang, *Corrosion Science*, **2016**, *108*, 169-172.

[72] “Effects of Te on intergranular embrittlement of a Ni–16Mo–7Cr alloy”, H. Cheng, F. Han, Y. Ji, Z. Li, X. Zhou, *Journal of Nuclear Materials*, **2016**,*461*, 122-128.

[73] “Effect of temperature on diffusion behaviour of Te into nickel”, Y. Jia, H. Cheng, J. Qiu, F. Han, Y. Zou, Z. Li, *Journal of Nuclear Materials*, **2013,** *441*, 372-379.

[74] “EPMA and TEM characterization of intergranular tellurium corrosion of Ni–16Mo–7Cr–4Fe superalloy”, H. Cheng, B. Leng, K. Chen, Y. Jia, J. Dong, Z. Li, Y. Zhou, *Corrosion Science*, **2015,** *97*, 1-6.

[75] “First-principles study of intergranular embrittlement induced by Te in the Ni R5 grain boundary”, W. Liu, H. Han, C. Ren, X. He, Y. Jia, S. Wang., W. Zhang, Z. Li, X. Zhou, Y. Zou, P. Huai, H. Xu, *Computational Materials Science*, **2014**, *88*, 22-27.

[76] “Commissioning and first results of scanning type EXAFS beamline (BL-09) at INDUS-2 synchrotron source”, K. Poswal, A. Agrawal, A. K. Yadav, C. Nayak, S. Basu, S. R. Kane, C. K. Garg, D. Bhattachryya, S. N. Jha, N. K. Sahoo, *AIP Conference Proceedings*, **2014,** *1591*, 649-651.

[77] “A comprehensive facility for EXAFS measurements at the INDUS-2 synchrotron source at RRCAT, Indore, India”, S. Basu, C. Nayak, A. K. Yadav, A. Agrawal, A. K. Poswal, D. Bhattacharyya, S. N. Jha and N. K. Sahoo, *Journal of Phyics: Conference Series*, **2014**, *493*, 012032.

[78] “X ray Absorption: Principles, Applications, Techniques of EXAFS, SEXAFS and XANES”, by D. C. Konigsberger, R. Prins, Wiley, New York, **1988**.

[79] “Introduction to XAFS: A practical guide to X ray Absorption Fine Structure Spectroscopy”, by Grant Bunker, Cambridge University Press, Cambridge, **2010.**

[80] “Analysis of soils and minerals using X-ray absorption spectroscopy”, S. D. Kelly, D. Hesterberg, B. Ravel.; in Methods of Soil Analysis - Part 5. Mineralogical Methods; Soil Sci. Soc. Am., Madison, WI. A. L. Ulery, R. Drees (Eds.), **2008**, 387-464.

[81] “Analysis of multiple-scattering XAFS data using theoretical standards”, M. Newville, B. Ravel, D. Haskel, J. J. Rehr, E. A. Stern, Y. Yacoby, *Physica B*, **1995**, *208*, 154-156.

[82] “ATHENA, ARTEMIS, HEPHAESTUS: data analysis for X-ray absorption spectroscopy using IFEFFIT”, B. Ravel, M. Newville, *Journal of Synchrotron Radiation*, **2005**, *12*, 537-541. doi: https://doi.org/10.1107/S0909049505012719.

[83] “Practical Guides for X-Ray Photoelectron Spectroscopy (XPS): First Steps in planning, conducting and reporting XPS measurements”, D. R. Baer, K. Artyushkova, C. R. Brundle, J. E. Castle, M. H. Engelhard, K. J. Gaskell, J. T. Grant, R. T. Haasch, M. R. Linford, C. J. Powell, A. G. Shard, P. Sherwood, V. S. Smentkowski, *Journal of vacuum science & technology. A, Vacuum, surfaces, and films: an official journal of the American Vacuum Society*, **2019**, *37*, 10.1116/1.5065501. https://doi.org/10.1116/1.5065501.

[84] “Focussed ion beam–transmission electron microscopy applications in ore mineralogy: Bridging micro- and nanoscale observations”, C. L. Ciobanu, N. J. Cook, S. Utsunomiya, A. Pring, L. Green, *Ore Geology Reviews*, **2011**, *42 (1)*, 6-31.

[85] “Ising model phase-diagram calculations in the fcc lattice with first- and second-neighbour interactions”, J. M. Sanchez, *Physical Review B*, **1982**, *25 (3)*, 1759-1765.

[86] “Cluster Approach to Order-Disorder Transformations in Alloys”, D. de Fontaine, *Solid State Physics*, 1**994**, *47*,133-176.

[87] “Atomic Ordering”, by G. Inden, W. Pitsch in Phase Transformation in Materials, (eds.) P. Haasen, VCH Press, New York, **1991**.

[88] “Foundations and Practical Implementations of the Cluster Expansion”, J. M. Sanchez, *Journal of Phase Equilibria and Diffusion*, **2017**, *38*, 238–251.

[89] “Comparison of two cluster-expansion methods for the energetics of Pd-V alloys,” C. Wolverton, A. Zunger, *Physical Review B*, **1994**, *50*, 10548 -10560.

[90] “Density-functional theory applied to phase transformations in transition-metal alloys”, W. Connolly, A. R. Williams, *Physical Review B*, **1983**, *27*, 5169-5172.

[91] “Cluster expansion method and its application in computational materials science”, Q. Wu, B. He, T. Song, J. Gao, S. Shi, *Computational Materials Science*, **2016**, *125*, 243-254.

[92] “The alloy theoretic automated toolkit: A user guide”, A. Van de Walle, M. Asta, G. Ceder, *Calphad*, **2014**, *26*, 539-553.

[93] “VASP the guide”, G. Kresse, M. Marsman, J. Furthmüller, http://cms.mpi.Univie. ac.at/vasp/.

[94] “Generalized Gradient Approximation Made Simple”, J. P. Perdew, K. Burke, M. Ernzerhof, *Physical Review Letters*, **1996**, *77*, 3865-3868.

[95] “Special points for Brillouin-zone integrations”, H. J. Monkhorst, J. D. Pack, *Physical Review B*, **1976**, *13*, 5188-5192.

[96] “Quantitative description of short-range order and its influence on the electronic structure in Ag-Pd alloys”, M. Hoffmann, A. Marmodoro, A. Ernst, W. Hergert, J. Dahl, J. Lång, P.

Laukkanen, M. P. J. Punkkinen, K. Kokko, *Journal of Physics: Condensed Matter*, **2016**, *28*, 305501.

[97] “Short-range order in multicomponent materials”, A. V. Ceguerra, M. P. Moody, R. C. Powles, T. C. Petersen, R. K. W. Marceau, S. P. Ringer, *Acta Crystallographica A*, **2012**, *68*, 547–560.

[98] “Special quasirandom structures”, A. Zunger, S. H. Wei, L. G. Ferreira, James E. Bernard, *Physical Review Letters*, **1990**, *65*, 353-356.

[99] “First-principles study of ternary fcc solution phases from special quasirandom structures”, D. Shin, A.l van de Walle, Y. Wang, Z. Liu, *Physical Review B*, **2007**, *76*, 144204.

[100] “Prediction of the Al-rich part of the Al-Cu phase diagram using cluster expansion and statistical mechanics, S. Liu, E. Martínez, J. L. Lorca, *Acta Materialia*, **2020**, *195,* 317-326.

[101] “Self-driven lattice-model Monte Carlo simulations of alloy thermodynamic properties and phase diagrams”, A. Van de Walle, M. Asta, *Modelling and Simulation in Materials Science and Engineering*, **2002**, *10*, 521-538.

[102] “The development of long-range order and the resulting strengthening effects in Ni_4Mo”, F. Ling, E. A. Starke Jr., *Acta Metallurgica*, **1971**, *19*, 759-768.

[103] “Order-Induced Strengthening in Ni_4Mo”, B. Chakravarti, E. A. Starke Jr., B. G. Lefevre, *Journal of Materials Science*, **1970**, *5*, 394-406.

[104] “Physical metallurgy of nickel—molybdenum alloys”, C. R. Brooks, J. E. Spruiell, E. E. Stansbury, *International Metals Reviews*, **1984**, *29*, 210-248.

[105] “Evaluating effective pair and multisite interactions for Ni-Mo system”, R. H. Banerjee, A. Arya, S. Banerjee, *AIP Conference Proceedings*, **2018,** *1942*, 090016. doi: https://doi.org/10.1063/1.5028931.

[106] “Short range order and its transformation to long range order in Ni_4Mo”, S. Hata, S. Matsumura, N. Kuwano, K. Oki, *Acta Materialia*, **1998**, *46*, 881-892.

[107] “Short range order and the development of long-range order in Ni_4Mo”, B. Chakravarti, E. A. Starke Jr., C. J. Sparks, R. O. Williams, *Journal of Physics and Chemistry of Solids*, **1974,** *35*, 1317-1326.

[108] “In situ diffuse scatterings of neutrons on binary alloys”, R. Caudron, M. Sarfati, M. Barrachin, A. Finel, F. Solal, *Physica B*, **1992**, *180 & 181*, 822-824.

[109] “Neutron-scattering and Monte Carlo study of short-range order and atomic interaction in $Ni_{0.89}Cr_{0.11}$”, W. Schweika, H. G. Haubold, *Physical Review B*, **1988**, *37,* 9240–9248.

[110] “Neutron scattering lengths and cross section”, V. Sears, *Neutron News*, **1992**, *3*, 29-37.

[111] “The composition of eta carbide in Hastelloy N after aging 10,000 h at 815°C”, J. M. Leitnaker, G. A. Potter, D. J. Bradley, J. C. Franklin, W. R. Laing, *Metallurgical Transactions A*, **1978**, *9*, 397–400.

[112] “The effect of silicon on precipitation and decomposition behaviours of M_6C carbide in a Ni–Mo–Cr superalloy”, Z. Xu, L. Jiang, J. Dong, Z. Li, X. Zhou, *Journal of Alloys and Compounds*, **2015**, *620,* 197-203.

[113] “Phase instability in Hastelloy N”, R. Gehlbach, H. McCoy Jr., in: International Symposium on Structural Stability in Superalloys, Seven Springs, Pennsylvania, **1968**, 346-366.

[114] "Carbides Evolution in a Ni-16Mo-7Cr Base Superalloy during Long-Term Thermal Exposure", F. Han, L. Jiang, X. Ye, Y. Lu, Z. Li, X. Zhou, 521, *Materials*, **201**7, *10*, 1-7.

[115] "Grain boundary character correlated carbide precipitation and mechanical properties of Ni-20Cr-18W-1Mo superalloy", Y. Han, X. Xue, T. Zhang, R. Hu, J. Li, *Materials Science and Engineering: A*, **2016,** *667*, 391-401.

[116] "Probing the local atomic structure of Sr-modified Al–Si alloys", P. Srirangam, S. Chattopadhyay, A. Bhattacharya, S. Nag, J. Kaduk, S. Shankar, R. Banerjee, T. Shibata, *Acta Materialia*,**2014,** *65*, 185–193.

[117] "Lattice parameter variation and its effect on precipitation behaviour of ordered Ni_2(Cr,Mo) phase in Ni-Cr-Mo alloys", A. Verma, J. B. Singh, S. D. Kaushik, V. Siruguri, *Journal of Alloys and Compound*s, **2020** ,*813*, 152195.

[118] "The properties of pure nickel", L. Jordan, W. H. Swanger, *Journal of Research of the National Bureau of Standards*, **1930**, *5*, 1291-1307

[119] "Phase diagrams of binary nickel alloys", P. Nash, *ASM International (USA)*, **1991**, *1991*, 394.

[120] "Irradiation effect on alloy GH3535 revealed by X-ray absorption fine structure", C. Li, G. Lei, R. Xie, Z. Jiang, Y. Zhu, C. Wang, W. Zhang, Q. Lei, *Nuclear Engineering and Design*, **2019**, *343*, 38–42.

[121] "EXAFS studies of nickel superalloys", N Binsted, A Bryan Edwards, *Journal of Physics: Conference Ser*ies, **2009**, *190*, 012071.

[122] "Enhanced stability of the strengthening phase Ni_2(Cr,Mo) in Ni–Cr–Mo alloys by adjacent

instability", J. Wei, B. Qian, Z. Xiao, M. Lia, R. Yu, *Computational Materials Science*, **2015**, *109*, 111-114.

[123] "Effect of ternary additions on the stability of ordered phases in Ni-Mo alloys—transmission electron microscopy results and first principles calculations", A. Arya, U. D. Kulkarni, G. K. Dey, S. Banerjee, *Metallurgical and Materials Transactions A*, **2008**, *39 A*, 1623-1629.

[124] "Probing long-range ordering in nickel-base alloys with proton irradiation," M. Song, Y. Yang, M. Wang, W. Kuang, C. R. Lear, G. S. Was, *Acta Materialia*, **2018**, *156*, 446-462.

[125] "Applications of extended X-ray absorption fine-structure spectroscopy to studies of bimetallic nanoparticle catalysts", A. I. Frenkel, *Chemical Society Reviews*, **2012**, *41*, 8163-8178.

[126] "Statistical analysis of composition fluctuations and short-range order in stoichiometric Ni–Cr–Mo alloys", A. Verma, N. Wanderka, J. B. Singh, B. Kumar, J. Banhart, *Ultramicroscopy*, **2013**, *132*, 227–232.

[127] "Computation of Ni-Cr phase diagram via a combined first-principles quantum mechanical and CALPHAD approach", K. S. Chan, Y. M. Pan, Y. D. Lee,*Metallurgical and Materials Transactions A*, **2006**, *37*, 2039-2050.

[128] "First principles investigation on the stability and elastic properties of $Ni_2Cr_{1-x}M_x$ (M= Nb, Mo, Ta, and W) superlattices", R. Hu, G. Cheng, J. Zhang, J. Li, T. Zhang, H. Fu, *Intermetallics*, **2013**, *33*, 60-66.

[129] "Corrosion of a stainless steel and nickel-based alloys in high temperature supercritical carbon dioxide environment", V. Firouzdor, K. Sridharan, G. Cao, M. Anderson, T.R. Allen, *Corrosion Science*, **2013**, *69*, 281-291.

[130] “Formation of diffusion barrier coating on superalloy 690 substrate and its stability in borosilicate melt at elevated temperature”, R.S. Dutta, C. Yusufali, B. Paul, S. Majumdar, P. Sengupta, R. K. Mishra, C. P. Kaushik, R. J. Kshirsagar, U. D. Kulkarni, G.K. Dey, *Journal of Nuclear Material*, **2013**, *432*, 72–77.

[131] “Interaction of Alloy 693 with borosilicate glass at high temperature”, R. Halder, P. Sengupta, G. Abraham, C. P. Kaushik, G. K. Dey, *Materials Today: Proceedings*, **2016**, *3*, 3025-3034.

[132] Corrosion behaviour of alloys in molten fluoride salts, G. Zheng, PhD Thesis, **2015**.

[133] “Effects of exposing duration on corrosion performance in weld joint of Ni-Mo-Cr alloy in FLiNaK molten salt”, J. Hou, G. Yu, C. Zeng, H. Ai, R. Xie, Y. Chen, X. Zhou, L. Xie, J. Wang, *Journal of Fluorine Chemistry*, **2016**, *191*, 110–119.

[134] D.F. Williams. L. Toth, K. Clarno, ORNL/TM-2006/12, **2006**, 1–69.

[135] “Electrochemical study of the corrosion of a Ni-based alloy GH3535 in molten (Li,Na,K)F at 700 ^{o}C”, Y. Wang, H. Liu, G. Yu, J. Hou, C. Zeng, *Journal of Fluorine Chemistry*, **2015**, *178*, 14-22.

[136] “Failure analysis of 316L stainless steel crucible by molten fluoride salt interaction with clay bonded silicon carbide”, R. S. Sellers, M. H. Anderson, K. Sridharan, T. R. Allen, *Engineering Failure Analysis*, **2018**, *42*, 38–44.

[137] “Long-term corrosion behaviours of Hastelloy-N and Hastelloy-B3 in moisture-containing molten FLiNaK salt environments”, F. Ouyang, C. Chang, J. Kai, *Journal of Nuclear Material*, **2014**, *446*, 81–89.

[138] “Microstructural studies on alloy 693,” R. Halder, R. S. Dutta, P. Sengupta, I. Samajdar, G.K. Dey, *Journal of Nuclear Materials,* **2014**, *453,* 91-97.

[139] “Microstructural and corrosion aspects of alloy 690,” R. S. Dutta, R. Tewari, *British Corrosion Journal*, **1999**, *34,* 201-205.

[140] “AlN coatings on Hastelloy-N alloy offering superior corrosion resistance in LiF-KF-NaF molten salt,” H. Zhu, B. Li, M. Chen, Z. Liu, Z. Tang, C. Qiu, *Journal of Fluorine Chemistry*, **2018**, *213*, 80-86.

[141] “Corrosion of 316 L stainless steel alloy and Hastelloy-N superalloy in molten eutectic LiF-NaF-KF salt and interaction with graphite”, R. S. Sellers, W. Cheng, B. C. Kelleher, M. H. Anderson, K. Sridharan, C. Wang, T. R. Allen, *Nuclear Technology*, **2014**, *188*, 192-199.

[142] “Corrosion of Incoloy 800H alloys with nickel cladding in FLiNaK salts at 850 °C,” Q. Dai, X. Xi Ye, H. Ai, S. Chen, L. Jiang, J. Liang, K. Yu, B. Leng, Z. Li, X. Zhou, *Corrosion Science*, **2018**, *133*, 349-357, https://doi.org/10.1016/j.corsci.2018.01.026.

[143] “A comparative study of surface layer formation in Ni-based alloys with varying Cr contents exposed to high temperature fluoride environment,” Rumu H. Banerjee, Vishal Singh, A. Arya, S. Banerjee, *Journal of Nuclear Materials*, **2019**, *516*, 54-62.

[144] “Handbook of X-ray Photoelectron Spectroscopy: A Reference Book of standard Spectra for Identification and Interpretation of XPS Data”, by J. F. Moulder, Perkin-Elmer, Physical Electronics Division, **1992**.

[145] “XPS study of Ni-base alloys oxide films formed in primary conditions of pressurized water reactor”, L. Marchetti, F. Miserque, S. Perrin, M. Pijolat, *Surface and Interface Analysis,* **2015**, *47*: 632– 642

[146] "An XPS Study with Depth Profiling for the Surface Oxide Layer Formed on Aluminides Produced on Superalloy 690 Substrates," R. S. Dutta, R. H. Banerjee, G. K. Dey, *Oxidation of Metals,* **2018,** *89*, 699-711.

[147] "Evolution of oxide scale on a Ni-Mo-Cr alloy at 900 °C", A. Ul-Hamid, A. I. Mohammed, S. S. Al-Jaroudi, H. M. Tawancy, N. M. Abbas, *Material Characterization,* **2007**, *58,* 13-23.

[148] "Nickel plating for active metal dissolution resistance in molten fluoride salts", L. Olson, K. Sridharan, M. Anderson, T. Allen, *Journal of Nuclear Material,* **2013**, *411*, 51-59.

[149] "Corrosion in the molten fluoride and chloride salts and materials development for nuclear applications", S. Guo, J. Zhang, W. Wu, W. Zhou, *Progress in Materials Science,* **2018**, *97*, 448-487.

[150] "Thermodynamic modeling of LiF-NaF-KF-CrF_3 system", H. Yin, P. Zhang, X. An, J. Cheng, X. Li, S. Wu, X. Wu, W. Liu, L. Xie, *Journal of Fluorine Chemistry,* **2018**, *209*, 6-13.

[151] "The diffusivity and solubility of fluorine in solid nickel from electrochemical measurements", S. N. S. Redday, R. A. Rapp, *Metallurgical Transaction B,* **1980**, *11*, 99-106.

[152] "Material corrosion in molten fluoride salts", Y. Wang, S. Zhang, X. Ji, P. Wang, W. Li, *International Journal of Electrochemical Science*, **2018**, *13,* 4891 – 4900.

[153] "Thermodynamic assessment of the Ni–Te system", C. M. Arvhult, C. Guéneau, S. Gossé, M. Selleby, *Journal of Material Science,* **2019**, *54,* 11304–11319.

[154] "Intergranular diffusion and embrittlement of a Ni-16Mo-7Cr alloy in Te vapor environment", H. Cheng, Z. Li, B. Leng, W. Zhang, F. Han, Y. Jia, X. Zhou, *Journal of Nuclear Materials*, **2015**, *467,* 341-348.

[155] “Influence of grain size on tellurium corrosion behaviours of GH3535 alloy”, L. Jiang, C. Fu, B. Leng, Y. Jia, X. Ye, W. Zhang, Q. Bai, S. Xia, Z. Lia, F. Liu, X. Zhou, *Corrosion Science*, **2019**, *148*, 110-122.